BRNO UNIVERSITY OF TECHNOLOGY

VYSOKÉ UČENÍ TECHNICKÉ V BRNĚ

FACULTY OF MECHANICAL ENGINEERING

FAKULTA STROJNÍHO INŽENÝRSTVÍ

ENERGY INSTITUTE

ENERGETICKÝ ÚSTAV

GREASE FLOW IN THE BALL JOINT OF THE STEERING ARM OF A CAR

PROUDĚNÍ TUKU V KULOVÉM KLOUBU RAMENE ŘÍZENÍ AUTOMOBILU

MASTER THESIS

DIPLOMOVÁ PRÁCE

AUTHOR — **Bc. LUKÁŠ BĚHOUN**

AUTOR PRÁCE

SUPERVISOR — **doc. Ing. PAVEL RUDOLF, Ph.D.**

VEDOUCÍ PRÁCE

BRNO 2024

BRNO UNIVERSITY OF TECHNOLOGY
FACULTY OF MECHANICAL ENGINEERING

Assignment Master's Thesis

Institut:	Energy Institute
Student:	**Bc. Lukáš Běhoun**
Degree programm:	Power and Thermo-fluid Engineering
Branch:	Fluid Engineering
Supervisor:	**doc. Ing. Pavel Rudolf, Ph.D.**
Academic year:	2023/24

As provided for by the Act No. 111/98 Coll. on higher education institutions and the BUT Study and Examination Regulations, the director of the Institute hereby assigns the following topic of Master's Thesis:

Grease flow in the ball joint of the steering arm of a car

Brief Description:

The steering arm ball joint is lubricated with grease, which acts like a non–Newtonian fluid. To function properly, it is necessary to determine the distribution of the lubricant and the forces (moments) required to move the joint. Because of the very thin gaps between the moving and stationary parts of the joint, research on the lubricant behavior requires the use of advanced experimental methods and computational flow simulations.

Master's Thesis goals:

The student will conduct multidisciplinary research based on a combination of experimental modelling and computational simulations, which will include the following:
– interpolation of measured rheograms into a non–Newtonian fluid model.
– experimental determination of the force relations during the motion of a body over a very thin lubricating film
– determination and reconstruction of the lubrication film thickness in the ball and socket joint using tomography
– computational simulations of the non–Newtonian fluid for the case of a sample moving on a plane surface and for the case of a ball and socket joint
– validation of the calculation using experimental data

Recommended bibliography:

CZABAN, A. CFD analysis of non-Newtonian and non-isothermal lubrication of hydrodynamic conical bearing. Journal of KONES. 2014, s. 49-56.

BENAMARA, N.; ALLALI, A.; BELBACHIR, S.; LOUSDAD, A. a , A. Experimental and Numerical Analysis of a Laminar Flow between two Planes with variable Slope. Algerian Journal of Engineering & Research. 2021, roč. 5, č. 1.

Deadline for submission Master's Thesis is given by the Schedule of the Academic year 2023/24

In Brno,

L. S.

doc. Ing. Jiří Pospíšil, Ph.D. Director of the Institute	doc. Ing. Jiří Hlinka, Ph.D. FME dean

Abstract

This master's thesis deals with the lubrication of automotive steering ball joints using a multidisciplinary approach. It combines experimental modeling, computer simulations, and advanced imaging techniques. X-ray computed tomography (CT) was utilized to analyze the thickness of the lubricating film. The lubricant used in the ball joints is a non-Newtonian fluid called grease. Rheological data were utilized to develop four distinct non-Newtonian fluid models. Tribological measurements provided information on the force interactions in the lubricating films, which were further investigated through Computational Fluid Dynamics (CFD) simulations, and the results were compared. The most suitable non-Newtonian fluid model was identified and applied to simulate the behavior of grease in the real geometry of ball joint obtained from CT scans. The simulation results were subsequently compared with experimental data.

Keywords

Ball joint, grease, CT, CFD, non-Newtonian fluid, rheology, lubrication

Abstrakt

Tato diplomová práce se zabývá mazáním kulových kloubů využívaných v systémech zavěšení a řízení automobilů s využitím multidisciplinárního přístupu. Kombinuje experimentální modelování, počítačové simulace a pokročilé zobrazovací techniky. Pro analýzu tloušťky mazacího filmu byla využita rentgenová počítačová tomografie (CT). Plastickým mazivem v kulových kloubech je nenewtonská kapalina zvaná tuk. Za účelem vytvoření modelu kapaliny byla využita reologická data, podle kterých byly vytvořeny čtyři modely nenewtonské kapaliny. Tribologická měření následně poskytla informace o silových interakcích v mazacích filmech, jež byly dále zkoumány pomocí CFD simulací a výsledky byly srovnány. Tím byl identifikován nejvhodnější model nenewtonské kapaliny, který byl aplikován na simulaci chování tuku v reálných geometriích kloubů získaných z CT snímků. Výsledky simulace byly následně porovnány s experimentálními daty.

Klíčová slova

Kulový kloub, plastické mazivo, CT, CFD, ne-Newtonská kapalina, reologie, mazání

Rozšířený abstrakt

Tato diplomová práce se zabývá mazáním kulových kloubů. Kulový kloub je klíčovou součástí používanou v systémech zavěšení a řízení automobilů. Je navržen tak, aby umožňoval plynulý a kontrolovaný pohyb kol. Jednoduše řečeno, skládá se z kulového čepu uloženého v pouzdře, což umožňuje otáčení kulového čepu ve více osách. Tento víceosý pohyb je nezbytný pro správnou funkci zavěšení a řízení vozidla, což umožňuje kolům pohyb nahoru a dolů, stejně jako otáčení v reakci na terén a řízení.

První kapitola práce se zabývá základním popisem kulových kloubů a jejich použitím v automobilovém průmyslu. Kulový kloub se skládá ze čtyř hlavních částí: kulového čepu, plastového ložiska, hlavy kloubu a plastického maziva mezi ložiskem a čepem. Tato práce se zaměřuje právě na plastické mazivo, v případě kulových kloubů je to konkrétně tuk. Ten se obecně chová jako nenewtonovská pseudoplastická kapalina, což znamená, že jeho viskozita klesá se zvyšujícím se gradientem rychlosti.

Protože není známé rozložení tuku v uzavřeném kulovém kloubu, je třeba k jeho zjištění využít pokročilé zobrazovací metody. V tomto případě byla použita počítačová tomografie. Vyhodnocením naměřených snímků se zabývá druhá kapitola. Proběhlo několik měření, přičemž první měření bylo provedeno ve spolupráci s CEITECem v Brně. Toto měření odhalilo, že konvenční ocelový kloub nelze prosvítit s dostatečným rozlišením a kontrast mezi jednotlivými složkami kloubu není dostatečný. Na základě tohoto zjištění byl navržen nový kloub v hliníkovém provedení s částicemi wolframu přidanými do tuku. Další měření proběhlo na výkonnějším zařízení na FZU v Praze. Nejprve byl proveden tzv. rychlý sken, který ukázal, že kontrast a rozlišení při měření na novém zařízení jsou dostatečné. Celý kloub byl tedy naměřen znovu s co nejlepším rozlišením. Tyto snímky posloužily k určení množství a pozice vzduchu uzavřeného v kloubu, hlavně kvůli nedokonalému procesu montáže kloubu. Při dalším skenování byl zvětšen čas měření a snížena oblast skenování na výseč 60°. Tím bylo možné dosáhnout ještě vyššího rozlišení než při skenování celé geometrie kloubu. Tyto snímky byly použity k určení rozměrů vrstvy tuku v kulovém kloubu. Naměřené snímky byly před vyhodnocením podrobeny post-processingu, tedy filtrování pomocí Gaussova a Kuwaharova filtru. Výsledná geometrie tukové vrstvy a vzduchových kapes byla segmentována pomocí dvou metod: thresholding (prahování) a watershed transformace.

Obsahem třetí kapitoly je základní popis druhů nenewtonských kapalin, popis experimentálních dat z měření nareometru a vytvoření čtyř modelů nenewtonovské kapaliny pomocí proložení naměřených dat. Naměřená data (závislost smykového napětí na gradientu rychlosti) poskytnutá výrobcem tuku jsou uvedena pro dvě teploty: 20 °C, tedy provozní teplota kulových kloubů, a 40 °C, což je teplota, při které se kulové klouby montují. Z těchto dat byla navíc vypočítána závislost dynamické viskozity na gradientu rychlosti. Protože byla poskytnuta data pouze pro dvě teploty, teplotní závislost, která se obvykle modeluje pomocí Arrheniova zákona, byla zanedbána, a místo toho byl vytvořen separátní model pro každou teplotu. Použité modely jsou Power-Law, Herschel-Bulkley, Cross a Carreau, tedy modely, které přímo nabízí software Ansys Fluent. Skripty, které hledají konstanty modelů, využívají Levenbergův-Marquardtův algoritmus pro nalezení těchto konstant. Veškeré použité skripty jsou přiloženy v přílohách. Pro porovnání vhodnosti modelů byl použit koeficient determinace. Z porovnání vychází, že všechny mod-

ely mají koeficient determinace vyšší než 99,5 %, což znamená téměř perfektní shodu s naměřenými daty.

Čtvrtá kapitola se zaměřuje na experimentální měření silových poměrů v úzkých spárách mezi dvěma rovnoběžnými povrchy. Při vzájemném pohybu dvou desek s danou mezerou mezi nimi, vyplněnou kapalinou, dochází ke vzniku síly na horní pohybující se desku. Tento fenomén vysvětluje tzv. Couettovo proudění. Prvně byl v této kapitole analyticky odvozen zjednodušený vztah pro velikost síly působící na horní desku. Z tohoto vztahu plyne, na čem je tato síla závislá - rychlost pohybu desky, velikost mezery, plocha horní desky a viskozita kapaliny. Experiment byl navržen podle modelu Couettova proudění, tedy s jednou pohybující se deskou a jednou stacionární deskou s mezerou mezi nimi, vyplněnou tukem. Experiment probíhal pro 3 různé velikosti mezery, kde pro každou z těchto velikostí byly provedeny experimenty pro 3 různé rychlosti. Experimenty se konaly při teplotách, pro které byl určen materiálový model, tedy 20 °C a 40 °C. Dále byly experimenty provedeny s třemi různými horními deskami - každá s jinou plochou. Pro měření byla vyhodnocena nejistota měření, vliv teploty, vliv velikosti desky, vliv rychlosti a nakonec byl zkoumán vliv drsnosti povrchu pohybující se desky na velikost síly.

Poslední kapitola se zaměřuje na numerické simulace, které si kladou za cíl stanovit nejvhodnější model nenewtonské kapaliny a následně tento model ověřit na reálné geometrii kloubu. Prvním druhem simulace byl 2-D zjednodušený model experimentálního měření, tedy dvě desky - jedna stacionární a jedna pohybující se stejně jako při experimentu. Vzhledem k vysokému počtu simulací byla pro výpočty prvně provedena studie nezávislosti výsledků na velikosti sítě. Nejprve byly provedeny výpočty pro všechny modely nenewtonských kapalin, které jsou popsány ve třetí kapitole. Tyto simulace byly provedeny za stejných podmínek (velikost mezery, velikost desky, rychlost a teplota) pro jednoduché srovnání. Při teplotě 20 °C vykazovaly Crossův a Carreauův model nejlepší shodu s experimentálními daty, přičemž rozdíl mezi těmito modely činil pouze 5 % podle metody MPD popsané v této kapitole. Další simulace ukázaly, že Crossův model trvale překonával Carreauův model přibližně o 5 % a lze ho tedy prohlásit za nejvhodnější. Stejným postupem byl určen Power-law model jako nejvhodnější pro popis chování při 40 °C. Výsledky z této simulace byly následně porovnány s analytickým modelem odvozeným ve čtvrté kapitole, kde byl zjištěn minimální rozdíl výsledků.

Další simulací je 3-D simulace experimentálního měření, která si kladla za cíl ověřit, zda je zjednodušení na 2-D geometrii dostatečně přesné, a dále zjistit, jak ovlivňuje velikost síly obtékání tuku kolem hran a podél boku desky. Bylo zjištěno, že vliv je minimální a velikost síly pro 2-D a 3-D případ je téměř identická. Vliv obtékání desky tukem je tedy minimální.

Další simulace byly provedeny již pouze s vybraným modelem kapaliny na geometrii získané ve druhé kapitole. Cílem této simulace bylo porovnání výsledků s daty naměřenými na reálném kulovém kloubu. Prvně byly simulace počítány jako axisymetrická úloha. Výsledkem je, že moment způsobovaný odporem tuku při pohybu je zanedbatelně malý v porovnání s naměřenými daty. Tento závěr je podpořen i poslední simulací, která proběhla na 3-D geometrii získané ve druhé kapitole. Důvod tohoto velkého rozdílu je ten, že model použitý v této simulaci předpokládá pouze vrstvu maziva, což znamená, že síla vzniká výhradně smykem maziva. Naproti tomu skutečný kulový kloub zahrnuje celou geometrii, kde vrstva plastického maziva tvoří pouze malou část celého systému.

Hlavním zdrojem síly ve skutečném kloubu je suchý kontakt mezi plastovým ložiskem a ocelovým kuličkovým čepem.

Závěrem lze prohlásit, že utrhávací moment, který se objevuje po určité době, kdy je kulový kloub nečinný, může být částečně způsoben mazivem. Plastické mazivo se chová jako pevná látka, dokud není překročena mez kluzu. Toto chování bylo patrné i při simulacích, kdy dochází při změnách směru pohybu ke skokovým změnám momentu. Navíc je moment generovaný odporem plastického maziva mnohem menší než moment vznikající při suchém kontaktu v kulovém kloubu. Toto pozorování potvrzuje, že snížení točivého momentu by mohlo být dosaženo zlepšením mazacích mechanismů v kulovém kloubu, například zlepšením distribuce tuku v kloubu při jeho pohybu.

Bibliographic citation

BĚHOUN, Lukáš. *Proudění tuku v kulovém kloubu ramene řízení automobilu* [online]. Brno, 2024 [cit. 2024-05-19]. Dostupné z: https://www.vut.cz/studenti/zav-prace/detail/158157. Diplomová práce. Vysoké učení technické v Brně, Fakulta strojního inženýrství, Energetický ústav. Vedoucí práce Pavel Rudolf.

Declaration

I declare that I have personally compiled the thesis "Grease flow in the ball joint of the steering arm of a car" according to the instruction of my supervisor, doc. Ing. Pavel Rudolf, Ph.D. and with the use of the sources listed in bibliography.

Bc. Lukáš Běhoun

Acknowledgement

I would like to thank my thesis supervisor doc. Ing. Pavel Rudolf, Ph.D. for his professional guidance and help during the completion of my thesis. Additionally, I express my appreciation to Ing. Petr Šperka, Ph.D., for his support with experimental measurements. Special thanks are also due to Ing. Martin Petrenec, Ph.D., for his support during the entire process of completing my master thesis. I am also grateful to Ing. Jan Drahokoupil, Ph.D., for his cooperation and willingness to assist with CT scans.

I extend my gratitude to the company THK Rhythm Automotive for offering me this topic and providing the necessary data.

Lastly, I am deeply grateful to my family for their support throughout my whole studies.

Bc. Lukáš Běhoun

Contents

Introduction

In modern automotive engineering, the suspension and steering systems plays a pivotal role in ensuring both the safety and performance of vehicles. Among its crucial components, the ball joint serves as a vital link facilitating smooth articulation between the various components. Effective lubrication of these joints is imperative to minimize friction and wear, thus enhancing durability and reliability.

This thesis delves into the intricate process of understanding lubrication in steering arm ball joints. It employs a combination of experimental techniques and computational simulations to analyze the behavior of non-Newtonian lubricants in practical scenarios. The research starts with the construction of a comprehensive non-Newtonian fluid model based on experimentally measured rheograms. Subsequently, the investigation delves into the forces exerted when a body moves over a thin lubricating film, a critical parameter for assessing tribological performance.

Utilizing X-ray computed tomography (CT), the thesis accurately determines and reconstructs the thickness distribution of the lubricating film within ball and socket joints. Additionally, computational fluid dynamics (CFD) simulations are harnessed to model the behavior of non-Newtonian lubricants in both planar and spherical geometries, with a keen focus on achieving accuracy through comparison with experimental results.

Exploring grease lubrication in ball joint performance holds profound significance for enhancing the longevity, efficiency, and reliability of mechanical systems across various industries. Understanding grease distribution and grease behavior enables the optimization of lubrication processes. This integration of experimental modeling and computational simulations offers valuable insights into non-Newtonian fluid dynamics inside the ball joint.

1 Ball joint

A ball joint is a pivotal component used in suspension and steering systems of automotive vehicles, designed to allow smooth and controlled movement of the wheel assembly. Simply put, it is a component that consist of spherical stud encased within a housing assembly, that enables articulation and rotation in multiple axis.
The primary function of the ball joint is to provide a flexible yet robust connection between various suspension and steering components. For example, thanks to the ball joints, the wheel can move against the frame during suspension or cornering while still being firmly connected to the car frame.

1.1 Basic component of ball joint

The main components of the ball joint are ball stud, plastic bearing and socket, potentially a cap, boot and protective cover. For the demonstration of the individual parts of the ball joint, two steering system components were selected. The design of the inner tie rod is shown in figure (Figure 1.1) and the design of the outer tie rod is shown in figure (Figure 1.2).

Ball stud. The ball stud is spherical metal component that fits into a socket within the joint body (housing). It provides a pivot point for the joint, allowing for articulation and movement.

Plastic bearing. The plastic bearing surrounds the metal ball stud within the joint body. It serve as low-friction surface against which the ball stud can articulate, reducing wear and providing smooth movement.

Grease. The grease acts as a lubricant between the metal ball stud and plastic bearing, reducing friction, ensuring smooth movement, and minimizing wear on both components. The grease will be further explained in next section.

Joint body (housing). The joint body houses the ball stud and plastic bearing, providing support and structure for the ball joint assembly. It is typically made of metal and includes mounting points for attachment to other components of the suspension or steering system.

Cap. Based on the design and assembly, the ball joint can contain a cap. It covers and encloses the joint housing.

Boot. The boot covers the exposed end of the ball joint assembly. It helps prevent contaminants from entering the joint and damaging the internal components. The boot is typically made of rubber or another flexible material.

Protective cover. Some ball joints feature a protective cover that shields the entire assembly from external elements, providing additional protection against contaminants and preserving the integrity of the ball joint.

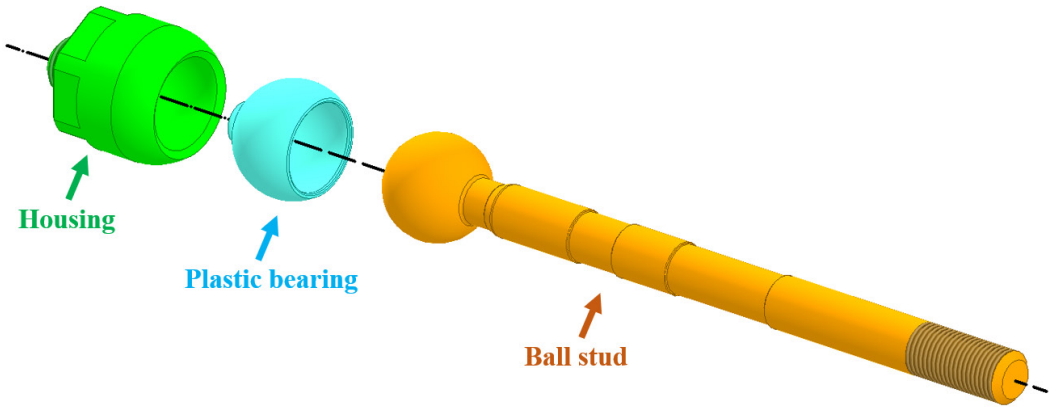

Figure 1.1. Model of the inner tie rod of the vehicles steering system.

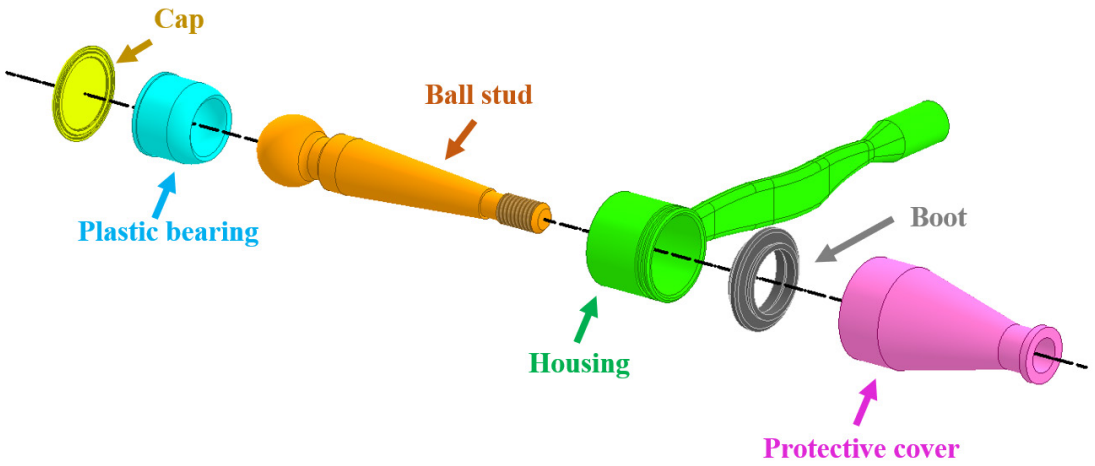

Figure 1.2. Model of the outer tie rod of the vehicles steering system.

1.2 Grease

Grease is a substance that combines a base oil with a thickening agent and additives, resulting in a semi-fluid or semi-solid structure. [1] Typically, grease comprises 65 % to 95 % by weight of base oil, 5 % to 35 % by weight of thickeners, and 0 % to 10 % of additives. [1]

Grease lubricants are further characterized by their operational temperature range, corrosion protection, oil separation sensitivity, water resistance, consistency, and material compatibility. [2]

1.2.1 Base oil

Base oil is the key ingredient of grease lubricants. Typically the oil with kinematic viscosity ranging from 15 $mm^2 \cdot s^{-1}$ to 1500 $mm^2 \cdot s^{-1}$ at temperature 40 °C are used. [1] The base oils are usually classified into mineral, synthetic and vegetable oils as shown in figure (Figure 1.3)

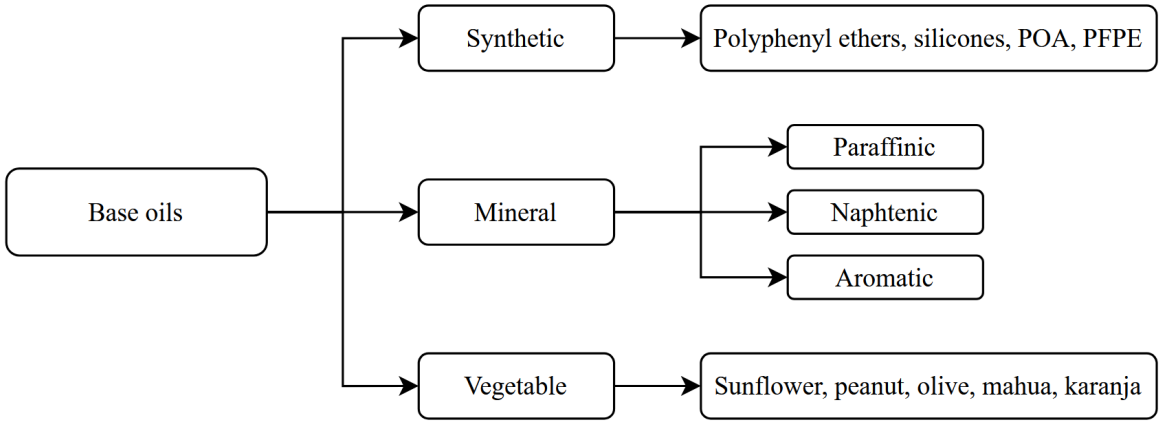

Figure 1.3. List of common commercially used base oils. (adapted from: [3])

1.2.2 Thickeners

Mixing the thickener with the base oil results in a grease. Within grease, the thickening agent forms a matrix that traps the base oil, preventing it from freely flowing. [3] The matrix of the thickener behaves as a reservoir of the lubricating oil, releasing the lubricating oil at the contact of friction surfaces. A wide array of thickeners are employed in grease lubrication, typically divided into two categories: soap (such as alkali and aluminium metal) and non-soap (including organic and inorganic varieties) as shown in figure (Figure 1.4).[1]

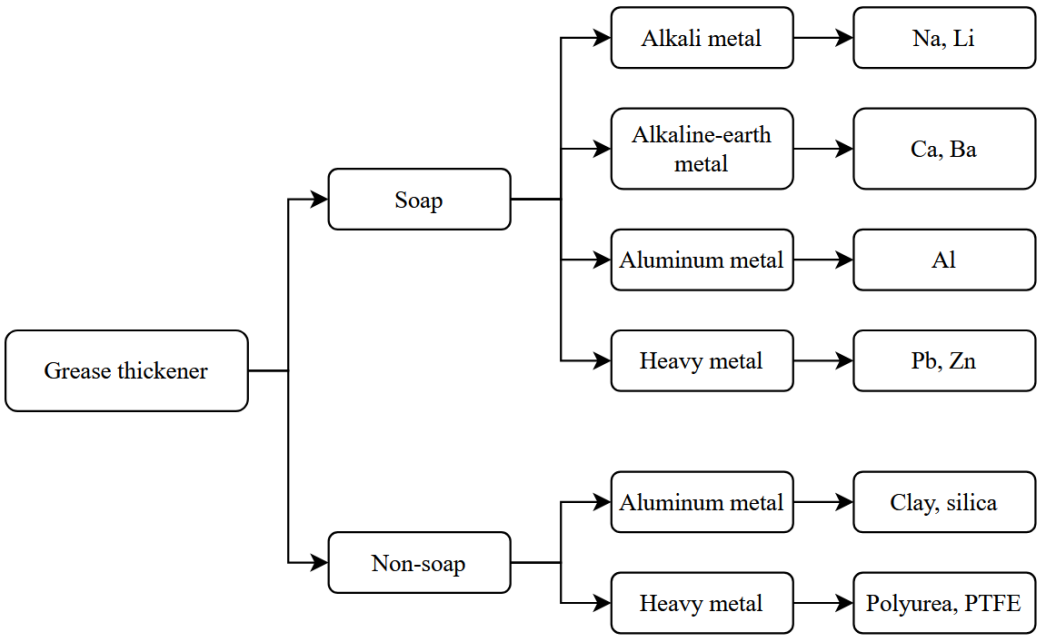

Figure 1.4. List of common commercially used thickeners. (adapted from: [3])

1.2.3 Additives

Additives are substances incorporated into the grease formulation to enhance its performance characteristics and properties. Grease additives serve various functions: anti-wear agents form protective films on metal surfaces, reducing friction and wear, rust and corrosion inhibitors protect against moisture and chemical-induced corrosion, extreme pressure additives prevent metal-to-metal contact under high loads, etc. [1] Based on the required grease properties, different additives are added to the grease formulation, as shown in figure (Figure 1.5).

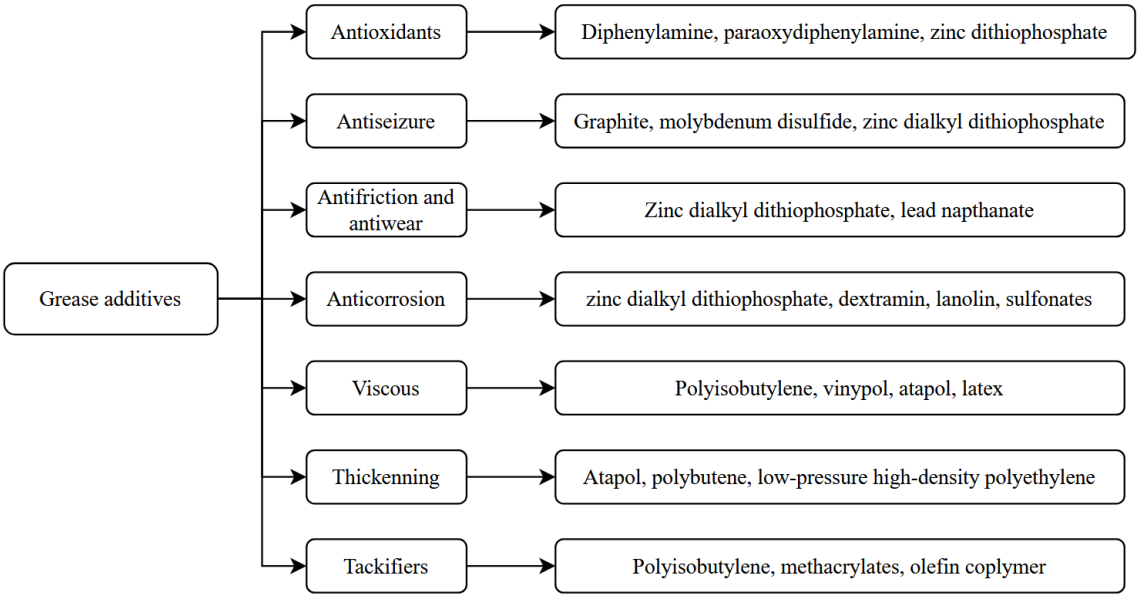

Figure 1.5. List of common commercially used additives. (adapted from: [3])

1.3 Suspension and Steering System

The purpose of suspension and steering system is to ensure vehicle stability, handling characteristics and overall safety of the vehicle. The suspension system manages the interaction between the vehicle and the road surface, optimizing tire grip and vehicle stability while minimizing vibration and impact forces. Meanwhile, the steering system translates the driver's input from the steering wheel into wheel movement, directing the vehicle's trajectory. This system incorporates mechanisms like steering gears, tie rods, and steering columns to ensure precise and responsive control over the vehicle's direction.

Given the multitude of steering and suspension system components, the following text will be focused only on the components that incorporates the ball joint. These components are shown in figure (Figure 1.6).

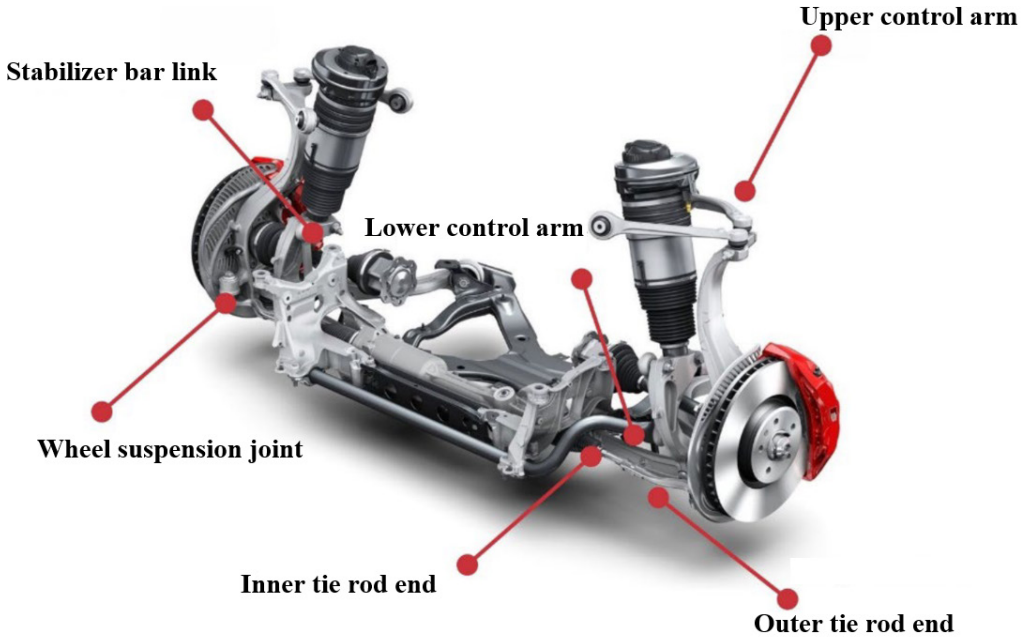

Figure 1.6. Components of steering and suspension systems of vehicle that contains the ball joint. (Adapted from [4])

Stabilizer bar link. The stabilizer bar link (Figure 1.7), also known as sway bar link or anti-roll bar link, connects the stabilizer bar to the suspension system. Its primary function is to transmit forces between the stabilizer bar and suspension system, helping to control body roll during cornering and improve stability of the vehicle.

Figure 1.7. Stabilizer bar link of vehicles suspension system. [5]

Lower control arm. The lower control arm (Figure 1.8), also known as lower A-arm, is a components of the suspension system, that connects the wheel hub to the vehicle´s frame or body. This component plays a crucial role in supporting the weight of the vehicle and controlling the movement of the wheels.

Figure 1.8. Lower control arm of vehicles suspension system. [6]

Upper control arm. Similar to lower control arm, the upper control arm (Figure 1.9), or upper A-arm, connects the wheel hub to the vehicle´s frame or body. It works in conjunction with the lower control arm to support the weight of the vehicle and control wheel movement, particularly in vehicles with independent suspension systems.

Figure 1.9. Upper control arm of vehicles suspension system. [7]

Wheel suspension joint. The wheel suspension joint (Figure 1.10) is part of the vehicle´s suspension system, that is essential for maintaining stability of the vehicle during the movement and overall vehicle performance within the suspension system. The ball joint typically connects the wheel hub to the suspension system.

Figure 1.10. Wheel suspension ball joints. [8]

Inner tie rod end. The inner tie rod end (Figure 1.11) is located at the end of tie rod assembly. It connects the outer tie rod end to the steering rack or steering gearbox assembly. Its role is to maintain proper steering alignment and stability by allowing for precise adjustment of tie rod assembly.

Figure 1.11. Inner tie rod of vehicle´s steering system. [9]

Outer tie rod end. The outer tie rod end (Figure 1.12) is part of vehicle´s steering system. It connects the front wheel spindle to the inner tie rod end. It´s purpose is to transmit steering input from driver to the wheels, allowing them to turn left and right.

Figure 1.12. Outer tie rod of vehicle´s steering system. [9]

1.4 Ball joint properties

Several properties are observed in ball joints. Generally the properties can be divided into three main groups - functional requirements, strength requirements and durability requirements. This classification is shown in figure (Figure 1.13).

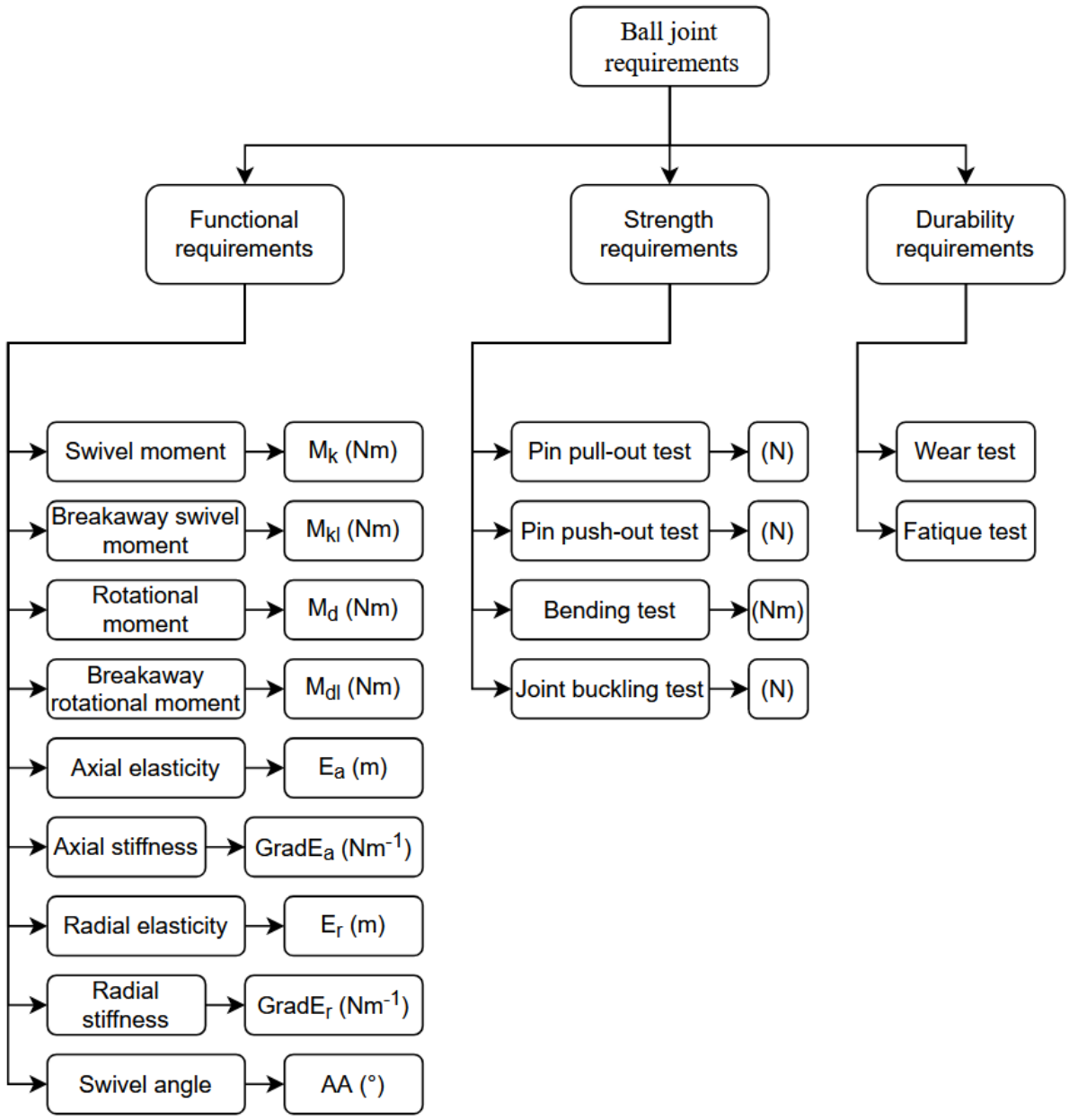

Figure 1.13. List of all ball joint requirements, that are usually specified by costumer. [10]

The functional requirements pertain to the operational performance of the ball joint under normal working conditions. These requirements focus on how well the ball joint functions in terms of its ability to transmit forces, absorb shocks, and facilitate movement within the mechanical system.

The strength requirements relate to the mechanical integrity and load-bearing capacity of the ball joint, ensuring it can withstand the forces and stresses encountered during operation without failure.
The durability requirements focus on the ability of the ball joint to withstand prolonged usage over its intended service life. These requirements involve tests and evaluations to assess wear resistance, fatigue resistance, and overall longevity.

The visual representation of the tested values is shown in figure (Figure 1.14) and figure (Figure 1.15).

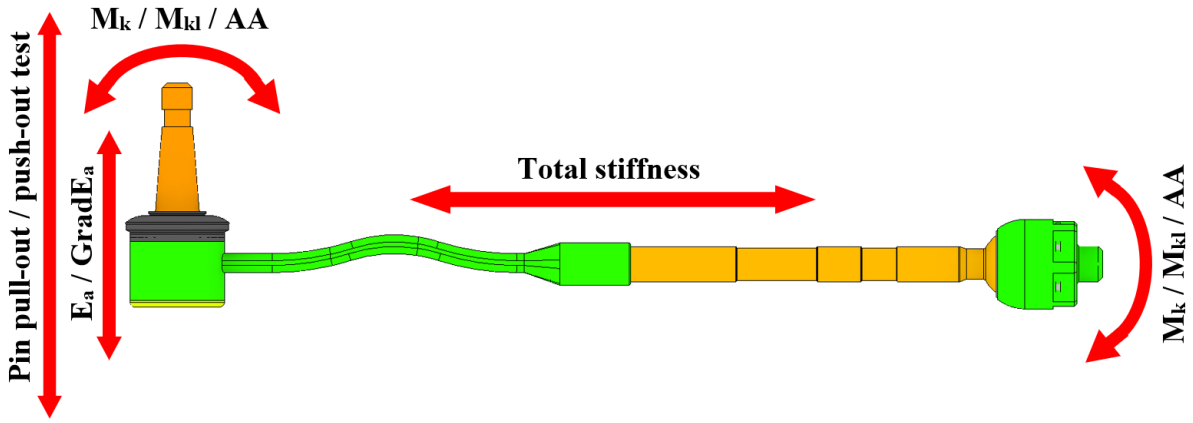

Figure 1.14. Graphical representation of all ball joint test done regarding the functional requirements. View from the side.

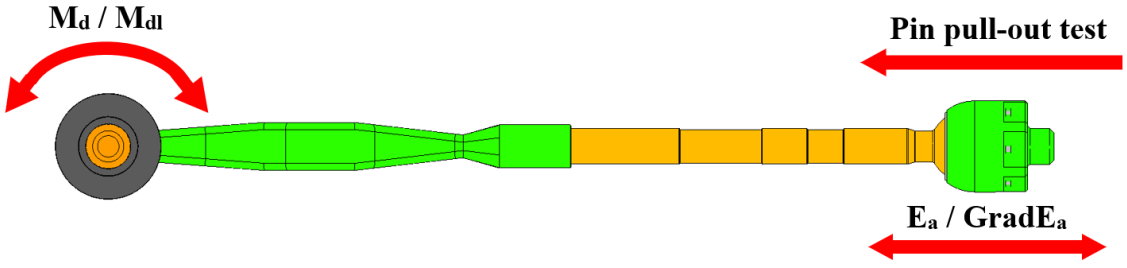

Figure 1.15. Graphical representation of all ball joint test done regarding the functional requirements. View from the top.

It is a known fact, that several of these properties of the ball joints, or costumer requirements on the ball joints, is highly dependent on the quality of lubrication. The list below summarize the influences of the proper grease lubrication on the ball joint performance.

Functional properties. Proper lubrication is essential for maintaining smooth movement and reducing friction within the ball joint. Inadequate lubrication can lead to increased resistance to motion, which may affect swivel and rotational moments. The breakaway moments may also be influenced, as they represent the initial resistance to movement before lubrication allows for smoother rotation.

Strength properties. Grease lubrication plays a role in reducing wear and preventing corrosion within the ball joint, which can directly impact the strength requirements.

Durability properties. A well-lubricated ball joint experiences reduced wear, prolonging its lifespan and enhancing its resistance to degradation over time. Additionally, lubrication helps reduce friction and therefore the heat buildup, which can contribute to improved performance in pin fatigue tests by reducing the likelihood of fatigue-induced failures.

The importance of proper grease lubrication in ball joint performance cannot be overstated. Almost all of the ball-joint properties are directly influenced by the quality of the lubrication.

The quality of the lubrication can be influenced by several factors.
The grease application on the plastic bearing before ball joint assembly can influence the quality of the grease distribution inside the ball joint. The distribution can be also influenced by the grease smearing method during the assembly.
The properties of the grease, mainly the viscosity and the yield stress magnitude of this Bingham pseudoplastic fluid can influence the behavior of the grease during and after the ball joint assembly.
The manufacturing process influences the surface roughness and overall surface quality and wear resistance of the ball joint, which can impact the lubrication quality.

Investigating the intricacies of grease lubrication in ball joint performance is crucial for ensuring the longevity, efficiency, and reliability of mechanical systems across various industries. Effective lubrication mitigates wear, reduces frictional losses, and enhances the functionality of ball joints. By thoroughly understanding factors such as grease distribution, viscosity, and yield stress, lubrication processes can be optimized to maximize performance and minimize maintenance.

2 X-ray computed tomography

Computed Tomography (CT) in engineering is a non-invasive method employed to inspect the internal structures of diverse objects. The fundamental principle is illustrated in figure (Figure 2.1), where a conventional CT scanner comprises an X-ray source and an X-ray detector. The process involves rotating the object of interest between the source and the detector. The X-ray source emits a beam that penetrates the object, and the detector records the intensity of X-rays that pass through. As the object rotates, multiple X-ray projections are acquired from various angles. Subsequently, sophisticated algorithms process these projections to reconstruct a detailed cross-sectional image, providing a comprehensive and accurate visualization of the internal features and dimensions of the inspected object.

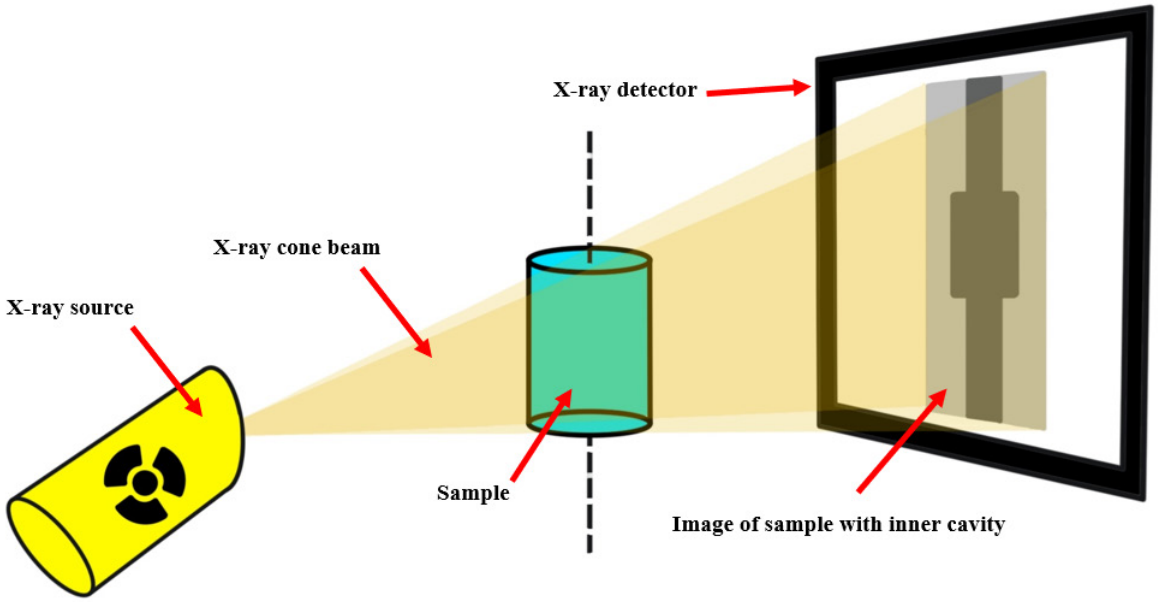

Figure 2.1. Basic principle of Computed Tomography imaging. (adapted from: [11])

2.1 X-ray sources

The X-ray source consist of: external high voltage supply, a filament, electron optics and an anode. When an electric current passes through the filament, the filament is heated and electrons are produced. Electrons are accelerated by o potential difference. Within the anode, the electrons decelerate and eventually come to a stop in the anode material, typically composed of a heavy metal like tungsten. The kinetic energy of the electrons is transformed into heat, with less than 1 % of this energy producing X-rays.[12] The X-ray beams subsequently pass through a beryllium window and an aluminum filter, with the filter serving to absorb low-energy beams and thus harden the X-ray beam. Two main types of X-ray sources exist: rotating X-ray tubes, where a focused electron beam collides with a rotating heavy metal anode, and stationary X-ray tubes, where electrons converge on a specific area of a stationary anode. Rotating tubes provide higher intensity due to

improved heat dispersion, while stationary tubes are simpler but may have image quality limitations due to potential deformities in the anode surface [13] [14].

2.2 X-ray detectors

X-ray detectors are crucial components responsible for measuring the intensity of X-ray beams passing through the scanned object and generating images based on the interaction data. The type of detector chosen determines the form of the acquired data, either electric current or a flash of light signal. Scintillation detectors utilize scintillating crystals that emit light when struck by X-rays, with a photo-detector capturing the light fluctuations for electronic conversion and subsequent image reconstruction.[15] Solid-state detectors, made of semiconductor materials like silicon, operate on the photoelectric effect. When X-rays hit the semiconductor, it emits electrons in proportion to the X-ray intensity.[16] The resulting electrical current is measured, and a computer processes the signal to reconstruct the image. The choice between scintillation and solid-state detectors depends on specific application requirements and desired imaging outcomes.

2.3 Image reconstruction

Image reconstruction is process of transforming data acquired from X-ray detectors at different angles into cross-sectional or 3-D images of the scanned object. Reconstruction is mathematical and computational process, and is crucial part of computed tomography. The process usually consist of: Data acquisition, sinogram formulation, filtering, reconstruction algorithm and image display.[17]

Data acquisition. Data are collected from all X-ray detectors.

Sinogram formulation. From acquired data, the sinograms are formulated. Sinogram is 2-D data array - angle dimension and position dimension. The data in sinogram reflects the intensity of X-ray beams detected during the measurement at every combination of angle and position.[18] The sinogram serves as an input for the reconstruction algorithm.

Filtering. The pre-reconstruction filtering is used to eliminate the artifacts and noise from measurement.The filter is applied in the frequency domain of the sinogram data.[19] This step involves modifying the data by multiplying it by the filter´s frequency response, which attenuates or enhances certain frequencies in the data. Common filters for pre-reconstruction filtering are: Ram-Lak filter, Shepp-Logan filter, Hann filter, and others.[20]

Reconstruction algorithms. Algorithms are the essential part of image reconstruction. There are various type of algorithms, such as: Filtered back projection, algebraic reconstruction technique, Fan-beam reconstruction and currently deep learning algorithms are used with fast development in AI technology.[21]

Image display. Images after reconstruction are in the cross-sectional 2-D form, where every pixel has specified intensity, that represents the level of X-ray beams attenuation or absorption. These images can be furthermore rendered into the 3-D model.

2.4 Sample preparation

The quality of images can be affected not just by the appropriate selection of CT scan parameters and image reconstruction methods, but also by the properties of the sample itself.
Transmittance, which describes the transparency of a material in the context of X-ray imaging, is a key factor. Higher transmittance signifies that more X-rays can pass through the material, whereas lower transmittance indicates that more X-ray beams are absorbed by the material.

Transmittance for homogeneous material can be described by equation (Equation 2.1):

$$T(E) = e^{-\mu(E)\cdot\rho\cdot L} \tag{2.1}$$

Where: $\mu(E)$ $(-)$ represents the X-ray absorption coefficient, ρ $(kg \cdot m^{-3})$ represents density of material and L (m) represents thickness of material.
Transmittance for non-homogeneous material can be described by equation (Equation 2.2):

$$T(E) = \int_0^d e^{-\mu(E,x)\cdot\rho(x)}\, dx \tag{2.2}$$

Where: $\mu(E,x)$ (m^{-1}) represents the X-ray absorption coefficient at given position x along the path, $\rho(x)$ $(kg\cdot m^{-3})$ represents density of material at given position x along the path and d (m) is the thickness of the material.

Both equation (Equation 2.1) (Equation 2.2) include variable μ that represents the X-ray absorption coefficient. This coefficient is dependent on various factors.

Material composition. Generally, elements with higher atomic numbers tend to exhibit higher absorption coefficients. This characteristic is often quantified by the effective atomic number, which is typically determined through experimental measurements or estimated using the formula (Equation 2.3).[22]

$$Z_{\text{eff}} = \left[\left(\sum \frac{(n_i \cdot Z_i)}{\sum (n_i \cdot Z_i)}\right)^{2.94} \cdot Z_i\right]^{\frac{1}{2.94}} \tag{2.3}$$

Where: n_i is the number of electrons in the i-th shell of the atom and Z_i is the atomic number of the i-th atom in the compound.

Energy of radiation. Materials respond differently to various energies of electromagnetic radiation.

Density. Materials with higher density contain a greater number of atoms within a given volume, significantly impacting the absorption coefficient.

Temperature and pressure. Extreme temperature and pressure can also affect absorption coefficient, particularly in gases and plasma.

Atomic and molecular structures. The arrangement and chemical bonding between molecules within the material can influence the absorption coefficient, especially in crystalline materials and complex compounds.

For the scope of this thesis, the following section will exclusively focus on the ball joint CT scan.

2.4.1 Ball joint sample preparation

The conventional ball joint is composed of several materials. The housing and ball pin are made of a steel alloy, the bearing is constructed from polyoxymethylene (POM), and lubricant is applied between the bearing and ball pin in the form of grease. Additionally, due to an imperfect assembly process, there may be air pockets within the lubricant. Some air pockets can also be present in the plastic bearing due to imperfections in the injection molding process.
Key properties that are significant for determining the absorption coefficient are listed in the table (Table 2.1).

Table 2.1: Properties of materials of conventional ball joint.

Material	**Density**	**Effective atomic number**	**Attenuation coefficient**
(-)	$(kg \cdot m^{-3})$	(-)	(cm^{-1})
Steel alloy	7850 [23]	22 [24]	1.3 [25]
Polyoxymethylene	1410 [26]	7 [27]	0.25 [28]
Grease	900 [29]	-	-
Air	1.2 [30]	7.28 [31]	2.17612E-05 [32]

An alternative ball joint configuration was designed to minimize the absorption (attenuation) coefficient. In this design, the steel alloy was substituted with an aluminum alloy (6082 - T6). To ensure a noticeable contrast between the polyoxymethylene and grease, WS_2 fullerene-like nanoparticles were mixed into the grease before ball joint assembly. In this configuration the composition of grease is: 2 % WS_2 particles and 98 % of original grease. The properties of these material are listed in the table (Table 2.2).

Table 2.2: Properties of materials of alternative ball joint.

Material	**Density**	**Effective atomic number**	**Attenuation coefficient**
(-)	$(kg \cdot m^{-3})$	(-)	(cm^{-1})
Aluminium alloy	2700 [33]	26.98 (estimated)	0.15 [34]
Polyoxymethylene	1410 [26]	7 [27]	0.25 [28]
Grease	900 [29]	-	-
WS_2	7500 [35]	65.6 (estimated)	-
Air	1.2 [30]	7.28 [31]	2.17612E-05 [32]

2.5 CT scans of ball joint

Prior to conducting a final scan to ensure precise measurement results, a series of preliminary scans were executed. These initial steps were essential to establish the correct choice of measuring device and alignment of the imagining apparatus and the specimen.

2.5.1 Contrast assessment

The initial CT scans were conducted at CEITEC CTLAB, located on the campus of Brno University of Technology. However, detailed information regarding the measurement settings was not provided, with the exception of the image resolution. Scans are shown in figures (Figure 2.2) and (Figure 2.3).

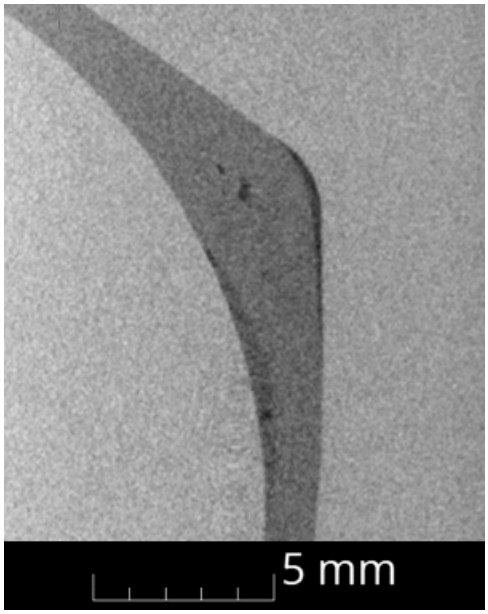

Figure 2.2. Aluminium configuration

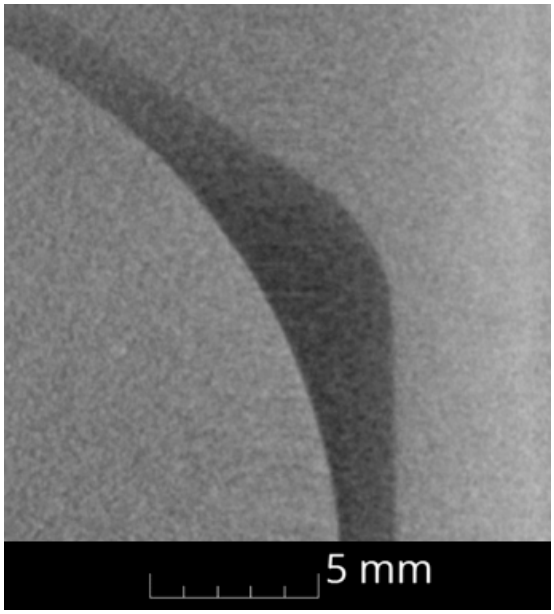

Figure 2.3. Steel configuration

Conclusion from images: Initial visual examination reveals a marked difference in contrast between the steel ball joint configuration and the aluminum ball joint configuration. The steel configuration demonstrates notably lower contrast levels between its components, including the housing, ball pin, polyoxymethylene, and grease, in comparison to the aluminum counterpart. That can be concluded even from the final resolution of images that is listed in table (Table 2.3). Therefore, only the aluminium configuration will be used for further analysis.

Table 2.3: First scan measurement resolution.

Ball joint configuration	**Resolution**
(-)	$\mu m/voxel$
Aluminium alloy	25
Steel alloy	40

Also it can be concluded, that the WS_2 fullerene-like nanoparticles are extremely small and therefore below the resolution of the CT scanner by several orders of magnitude. In the measured configuration, only 2 % of WS_2 particles were present.
It is worth noting that the addition of more WS_2 particles to the grease has the potential to enhance the contrast of the particles within the grease matrix. However, such an augmentation could impact the behavior of the grease during the ball joint assembly process. Moreover, the introduction of further WS_2 particles could result in the grease exhibiting a contrast level similar to that of polyoxymethylene or even aluminum. Given that the inherent contrast of the materials is deemed sufficient, the decision was made to forgo the addition of additional WS_2 particles.

2.5.2 Fast scan

The second measurement was carried out at the Institute of Physics of the Czech Academy of Sciences in Prague. However, specific details regarding the measurement settings were not provided. The primary objective of this scan was to assess the impact of employing an alternate scanning device on the resulting image resolution and overall image quality. Properties of measurement device used are presented in the table (Table 2.4). The 3-D reconstructed image and cross-sectional image are shown in figures (Figure 2.4) and (Figure 2.5).

Table 2.4: ZEISS Xradia 610 versa properties. [36]

Property	**ZEISS Xradia 610 versa**
Spatial resolution	500 mm
Resolution at a 50 mm working distance	1 μm
Source voltage range	30-160 kV
Source maximum power output	25 W
Minimum achievable voxel	40 nm

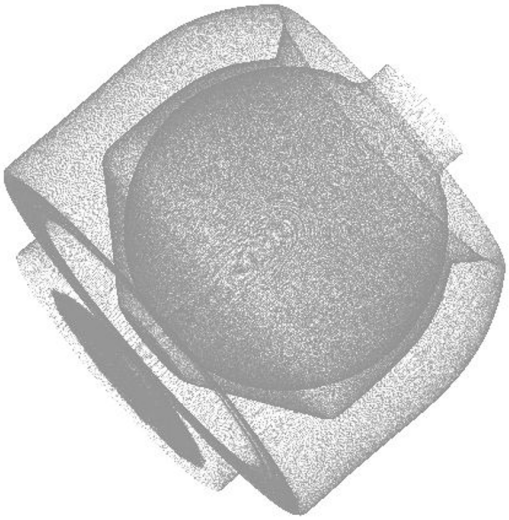

Figure 2.4. 3D reconstructed image

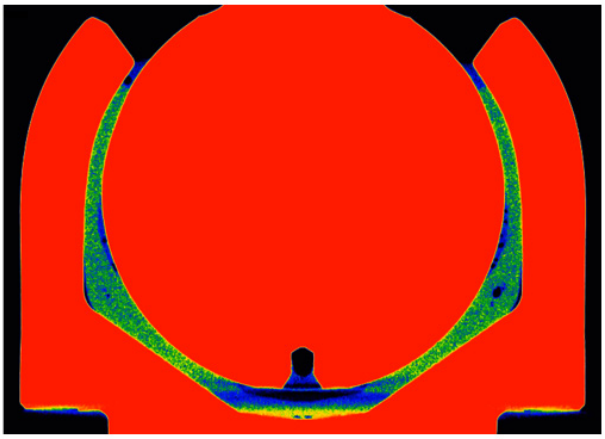

Figure 2.5. Cross-sectional image

Despite its relatively brief duration (approximately 30 minutes), the fast CT scan yielded images of satisfactory resolution, enabling clear differentiation among the four constituent materials: aluminum, grease, air, and polyoxymethylene. This successful outcome attests to the imaging system´s ability in material differentiation. As a result, the subsequent scan will also be conducted using the same imaging machine, given its demonstrated capability to provide accurate and detailed representations of the materials of interest.

2.5.3 Full scan of ball joint

Full scan (Figure 2.6) was conducted at the same machine as fast scan (ZEISS Xradia 610 versa) at the Institute of Physics of the Czech Academy of Sciences in Prague. Purpose of this scan was to have full geometry measured, to evaluate the position and size of air pockets in grease layer. However, detailed information regarding the measurement settings was not provided, with the exception of the image resolution.

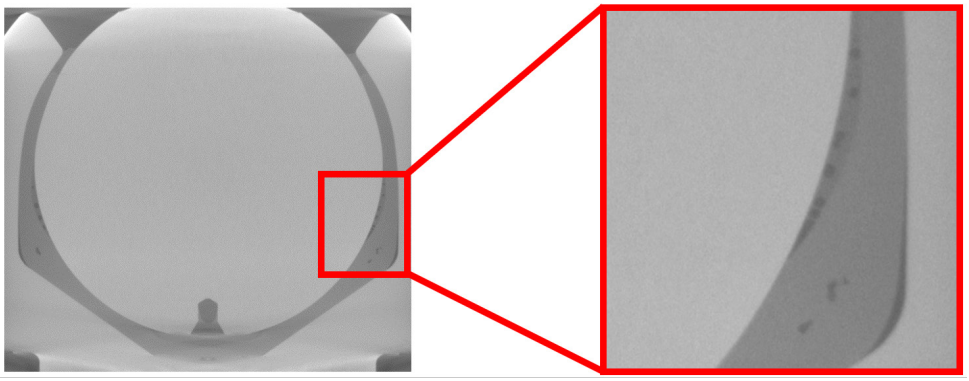

Figure 2.6. Scan of full geometry with detail on the grease layer with air gaps.

Even a cursory visual inspection reveals that the quantity of aluminum obstructing the X-ray beam path has a substantial impact on image quality. The image can be effec-

tively categorized into three distinct areas.

Low aluminum content area. In this region, where the least amount of aluminum is present, X-ray beam transmission is optimal, and almost no noise remains after image reconstruction.

Moderate aluminum content area. Within this area, characterized by a medium quantity of aluminum, the transmission of X-ray beams is not ideal, leading to some post-reconstruction noise. Nonetheless, the boundaries between different materials remain distinguishable, and image post-processing techniques can effectively resolve these issues. This area holds particular interest for the evaluation.

High aluminum content area. Within the region of highest aluminum concentration, the presence of aluminum significantly affects the transmission of X-ray beams. As a result, post-reconstruction noise levels are considerably increased, making it almost impossible to discern material boundaries within the image.

Further elaboration on the post-processing and image evaluation procedures will be provided in the following chapter.

2.5.4 Sectional scans

To assess the thickness, size and geometry of the grease layer, more targeted scans were performed. Unlike the comprehensive full scan, one scan was exclusively conducted for circular section spanning an angle of 60° (Figure 2.7) and (Figure 2.8). Pixel size of this scan is 9.36 μm x 9.36 μm x 9.36 μm.

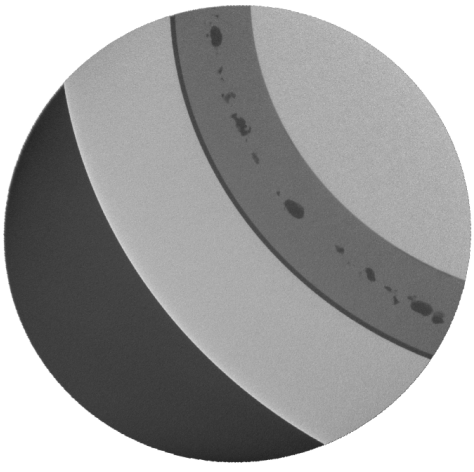

Figure 2.7. Top view of sectional scan

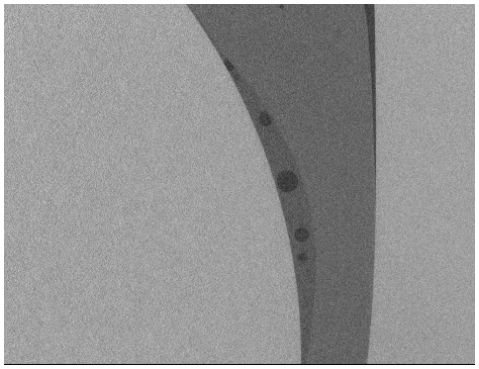

Figure 2.8. Side view of sectional scan

Further elaboration on the post-processing and image evaluation procedures will be provided in the following chapter.

2.5.5 High resolution scans

A next few scans were taken to determine the maximum possible magnification (lowest possible pixel size). All of them proved to be unreconstructable, therefore it can be concluded that the maximum possible enlargement while maintaining sufficient quality is sectional scan mentioned above (Figure 2.7) and (Figure 2.8). Details regarding the machine settings and image resolution for these scans can be found in table (Table 2.5).

Table 2.5: Properties of non-reconstructable images.

Property	Upper image	Middle image	Bottom image
Source power output	21 W	21 W	21 W
Source voltage	140 kV	140 kV	140 kV
Filter	LE3	Air	LE3
Pixel size	0.3959 μm	1.0712 μm	0.5082 μm
Exposure	500 s	100 s	500 s

2.6 CT scans post-processing

Post-processing in computed tomography refers to a process of refining the reconstructed image data to achieve optimal form for subsequent utilization. The process typically consist of: filtering, selection of region of interest, contrast enhancement and artifact correction. These steps play a crucial role in enhancing the overall quality and interpretability of the CT images.
Steps that were used in ball joint scans evaluation are described more in next sub-chapters.

2.6.1 Gaussian filter

Gaussian filter is a type of linear filter used for image processing. The filter is based on the Gaussian function, which is a bell-shaped curve that is characterized by its average (mean) and standard deviation.
Mathematically, the two-dimensional form of Gaussian filter, that was used in this evaluation, can be expressed as (Equation 2.4).

$$G(x,y) = \frac{1}{2\pi\sigma^2} e^{-\frac{x^2+y^2}{2\sigma^2}} \tag{2.4}$$

Where: G(x, y) represents value of the Gaussian function at given position (x,y), σ (-) represents standard deviation of the Gaussian distribution, x is the distance from origin in the horizontal axis and y is the distance from origin in the vertical axis.

The intensity of smoothing is characterized by value of standard deviation and kernel size and shape.[37] The greater the value of standard deviation is, the stronger the smoothing will be. Kernel represents the shape and size of neighborhood that will be sampled when calculating the pixel values to be modified.[37]

The Gaussian filter was used for both CT scans (Full scan and Sectional scan). The settings of filter is identical for both scans: standard deviation $\sigma = 1$, kernel size 3 x 3 and square kernel shape. The influence of Gaussian filter on image quality can be represented in two ways. Visually inspecting the influence as it is shown for sectional scan in figure (Figure 2.9). It can be seen that the image is smoother, and the artifacts in form of too bright or dark pixels was erased. That is especially useful for further evaluation.

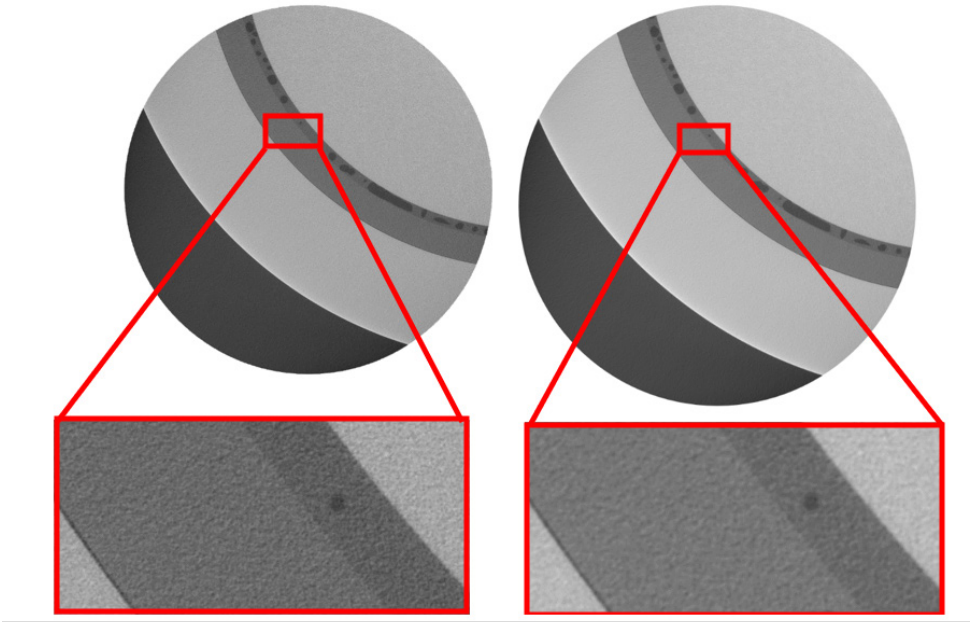

Figure 2.9. Influence of Gaussian filter on image quality. On the left is the image before filtering with detail to grease layer. On the right is the image after Gaussian filtering with detail to same spot.

Another way is displaying the histogram of intensity of pixels (voxels) distribution that represents the density of material. For sectional scan the histogram is shown in figure (Figure 2.10). Full scan is shown in figure (Figure 2.11).

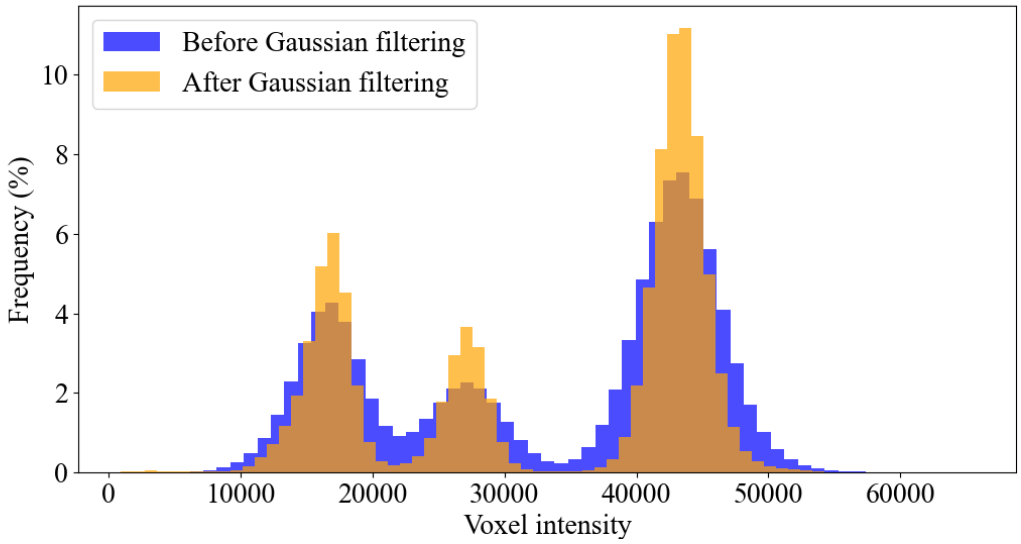

Figure 2.10. Histogram of voxel intensity distribution for sectional scan.

There can be distinguished 3 peeks on the histogram. Every peek belongs to one material - air, aluminium and polyoxymethylene. Grease does not have peek, because of much lower number of voxels of it´s intensity.
Applying the Gaussian filter to the original data makes the peaks much more distinct. Furthermore it reduces voxels with very high and very low intensity. That is important mainly for region of interest (ROI) selection (segmentation).

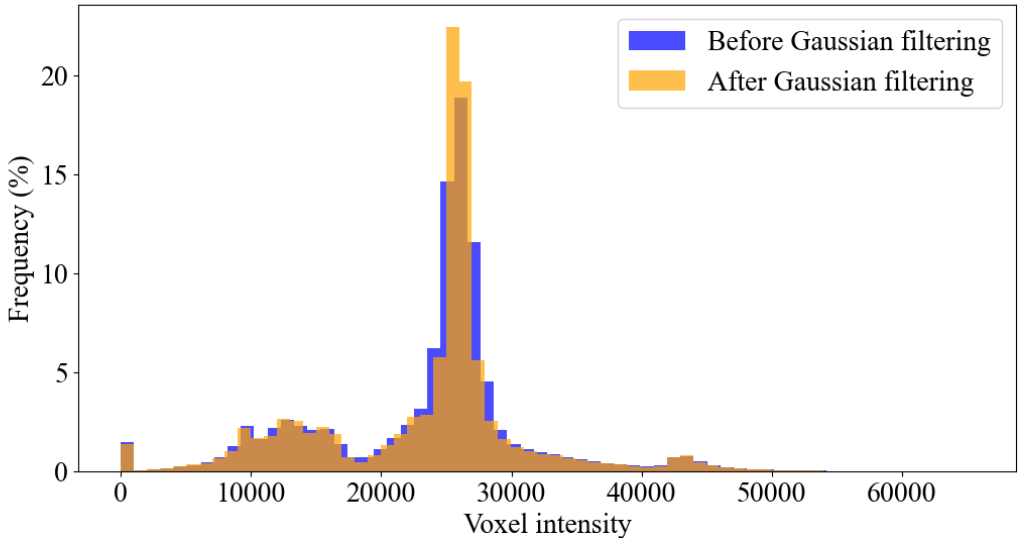

Figure 2.11. Histogram of voxel intensity distribution for full scan.

Same principle applies for the full scan histogram. Peeks are more distinguishable after the Gaussian filtering and the images are more convenient for the segmentation. The higher peek in this histogram (Figure 2.11) than in the sectional scan histogram

(Figure 2.10) is caused by much higher volume of aluminium present in the images (full scan has higher ratio of aluminium to rest of materials than sectional scan).

2.6.2 Kuwahara filter

Kuwahara filter is a type of non-linear smoothing for adaptive noise reduction. Majority of filters used in computed tomography are linear low-pass filters. They effectively reduce the noise, but usually smooth the edges, which is not desired. Kuwahara on the other hand can effectively reduce the noise and smooth the image while preserving the edges.

Let´s consider a 3x3 window with a pixel at coordinates (x, y). This window is divided into four quadrants: θ_1 (top - left), θ_2 (top - right), θ_3 (bottom - left), θ_4 (bottom - right) where the pixel at (x,y) coordinates is hared between all of them. For each quadrant, two values are computed: the average m_k and variance δ_k^2 described by equations: (2.5) (2.6). [38]

$$m_k = \frac{1}{(n+1)\times(n+1)} \times \sum_{(x,y)\in\theta_k} \varphi\big(f(x,y)\big) \tag{2.5}$$

$$\delta_k^2 = \frac{1}{(n+1)\times(n+1)} \times \sum_{(x,y)\in\theta_k} \left[\varphi(f(x,y)) - m_k\right]^2 \tag{2.6}$$

Where: k takes values from the set 0,1,2,3 (in case of 3 x 3 kernel size). The function f denotes the source image, and f(x, y) corresponds to the pixel value at coordinates (x, y). The function φ calculates the value of a given pixel, $\frac{1}{(n+1)\times(n+1)}$ represents the total number of pixels in the current area, where n is derived from the filter window size (e.g., 3 x 3 kernel results in n = 3).[38]

Next step is to find the smallest value of the variance in all four areas.[38] Mathematically expressed as (2.7).

$$\delta_{\min}^2 = \min_{k\in\{1,2,3,4\}} \left(\delta_k^2\right) \tag{2.7}$$

The value assigned to the central pixel at coordinates (x, y) is determined by taking the average of the region where the variance is minimal. [38]

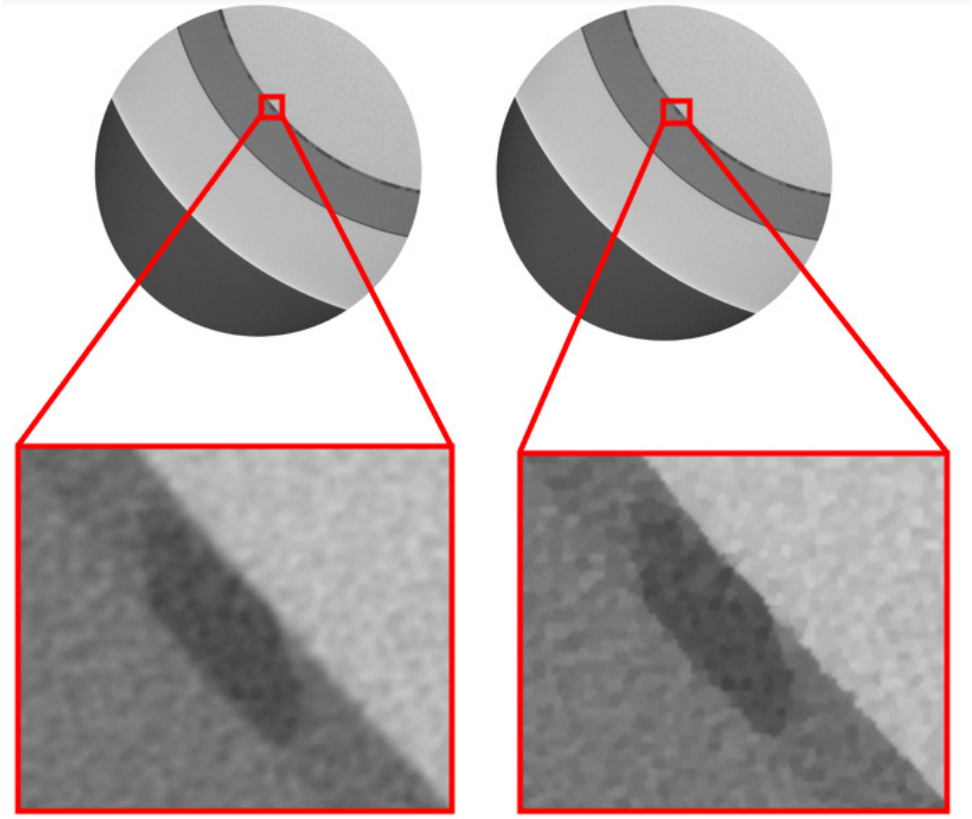

Figure 2.12. Influence of Kuwahara filter on image quality. On the left is the image before filtering with detail to grease layer and air gap. On the right is the image after Kuwahara filtering with detail to same spot.

The Kuwahara filter was applied to both Full and Sectional CT scans with identical settings, using a 3 x 3 kernel size. While larger kernel sizes (5 x 5 and 7 x 7) resulted in slightly smoother images, they also led to the blurring of material interfaces. In the context of image segmentation, having a clearly defined interface is crucial. The impact of the Kuwahara filter on image quality is assessed through two perspectives: visual inspection, as shown in figure (Figure 2.12), where it is evident that the interface is more distinct, and the overall image is slightly smoother compared to the Gaussian smoothing filter.

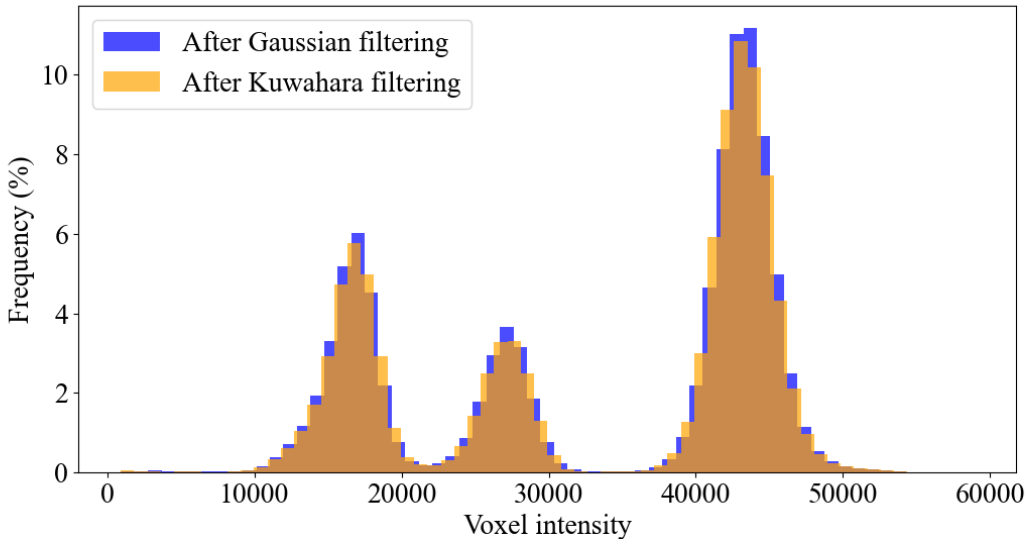

Figure 2.13. Histogram of voxel intensity distribution for Sectional scan (Kuwahara filter).

Similar to Gaussian filtering, the Kuwahara filter enhances the distinguishability of the three peaks in the histogram for the sectional scan, as illustrated in figure (Figure 2.13). Although the difference from the previous case may not be substantial, the primary objective of the Kuwahara filter was to enhance the clarity of edges, which was successfully achieved.

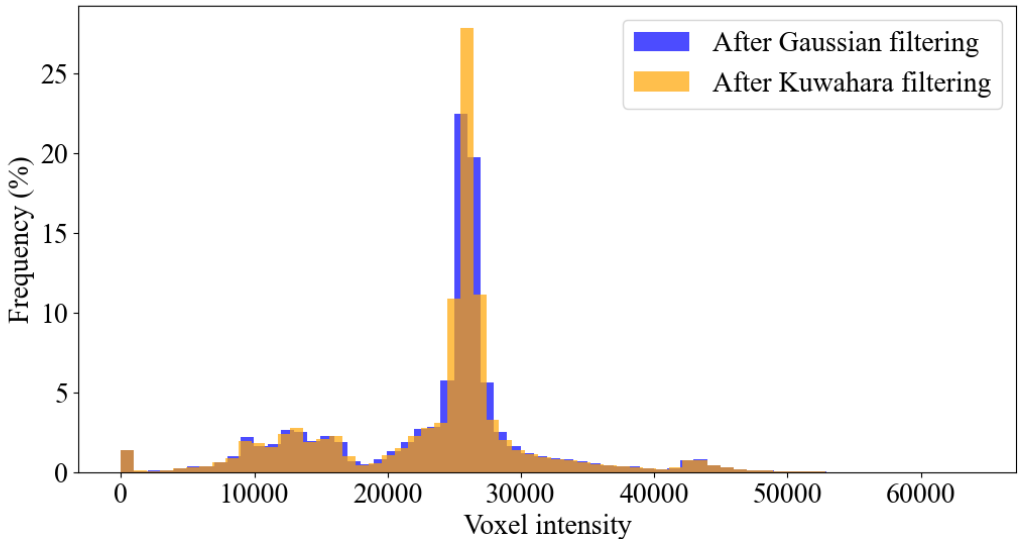

Figure 2.14. Histogram of voxel intensity distribution for Full scan (Kuwahara filter).

The same finding applies to the Full scan histogram (Figure 2.14). The peaks are more discernible compared to using the Gaussian filter alone. The elevated peak can still be attributed to the significantly higher number of aluminum voxels present in the image.

Additionally, the edges appear sharper, a crucial factor for further image segmentation processes.

2.6.3 Sobel filter

The Sobel filter, part of the broader Sobel operator, employs convolution with specially crafted kernels (Equation 2.8) to accentuate variations in intensity, thus bringing out edges in an image. Mathematically, the convolution of the input image I with the Sobel kernels G_x and G_y is expressed as (Equation 2.9 and 2.10). [39]

$$G_x = \begin{bmatrix} -1 & 0 & 1 \\ -2 & 0 & 2 \\ -1 & 0 & 1 \end{bmatrix} \quad and \quad G_y = \begin{bmatrix} -1 & -2 & -1 \\ 0 & 0 & 0 \\ 1 & 2 & 1 \end{bmatrix} \tag{2.8}$$

$$I_x = I * G_x \tag{2.9}$$

$$I_y = I * G_y \tag{2.10}$$

The fundamental principle of the Sobel filter revolves around determining the direction θ and magnitude M of the most significant intensity change by computing the gradient of image intensity at each pixel according to (Equation 2.12 and 2.11).

$$M = \sqrt{(I_x)^2 + (I_y)^2} \tag{2.11}$$

$$\theta = \arctan\left(\frac{I_y}{I_x}\right) \tag{2.12}$$

These equations quantify the abruptness or smoothness of intensity transitions at each pixel, offering insights into the likelihood that a pixel represents an edge.
Applying the Sobel filter to a pixel within a region of consistent intensity yields a zero vector (M=0). Conversely, when the filter is applied to a pixel located on an edge, the result is a vector indicating the direction from the darker side to the brighter side of the edge.
This filter was exclusively used for subsequent use in the watershed transformation used to separate air from grease layer, so the filter was used only on Full scan (Figure 2.15).

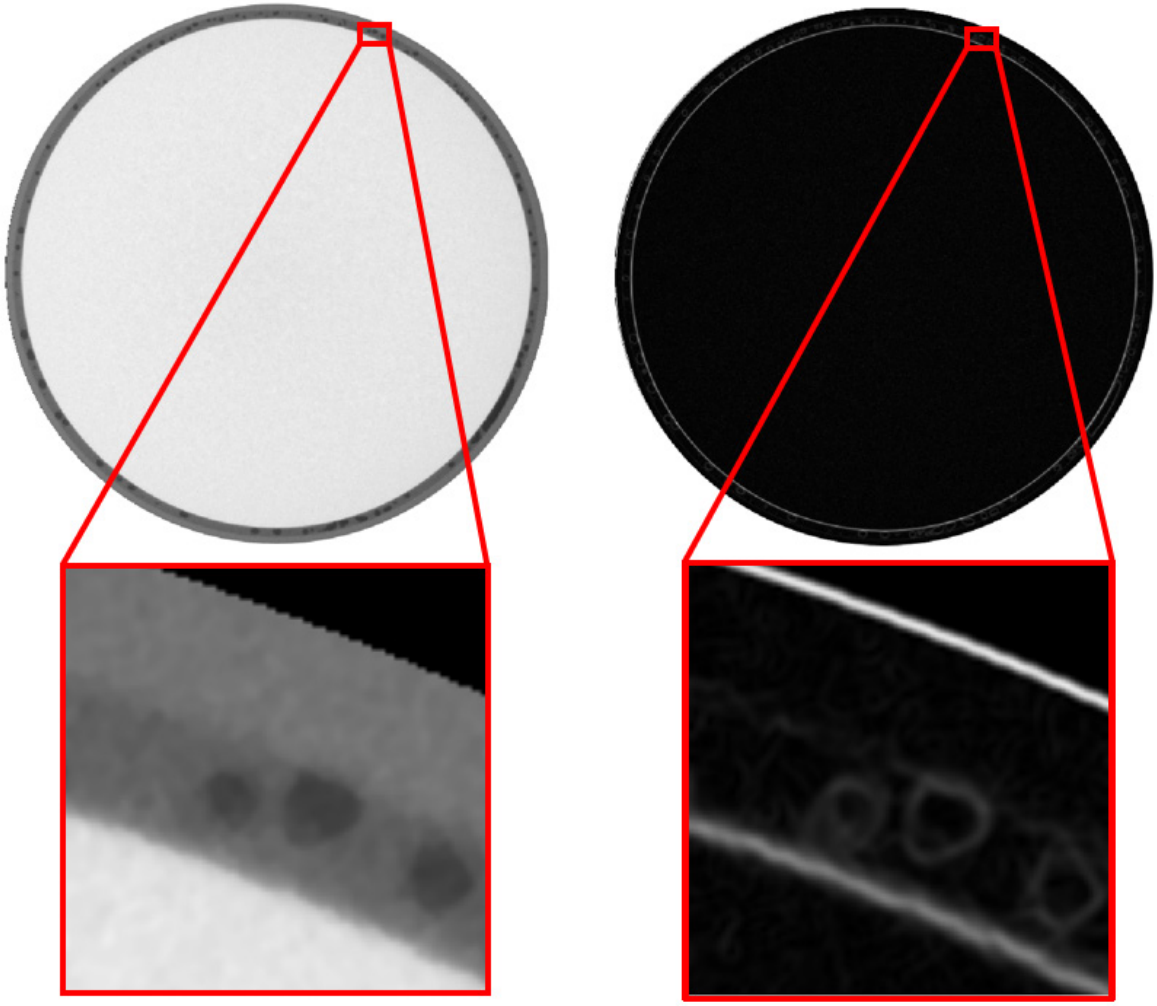

Figure 2.15. Influence of Sobel filter on image. On the left is the image before filtering with detail to grease layer and air gap. On the right is the image after Sobel filtering with detail to same spot.

2.7 Image segmentation

Image segmentation involves dividing an image into distinct segments or sets of voxels that share similar characteristics or meet specific criteria. In the evaluation of ball joint scans, this process entails assigning a particular phase (material) to each voxel within the image.

Numerous segmentation algorithms are available for image partitioning. However, this thesis will specifically describe only the algorithms that have been used for the evaluation.

2.7.1 Thresholding

The principle behind thresholding segmentation involves selecting a range of voxel intensities and attributing a phase (material) to all voxels falling within this range. The interval can be determined through manual inspection based on visual assessment or automatically using a predefined algorithm. In the context of this evaluation, due to the limitations of the software used, the interval was selected manually.

The primary objective of the Sectional scan is to reconstruct the grease layer, making air pockets irrelevant in this context. Consequently, the segmentation process did not take air into consideration. Figure (Figure 2.16) illustrates the segmentation of three phases (materials): 1 - grease, 2 - polyoxymethylene, and 3 - aluminum, with the Y-axis presented in logarithmic scale. In this case the manual selection should not introduce any errors due to clear borders between phases.

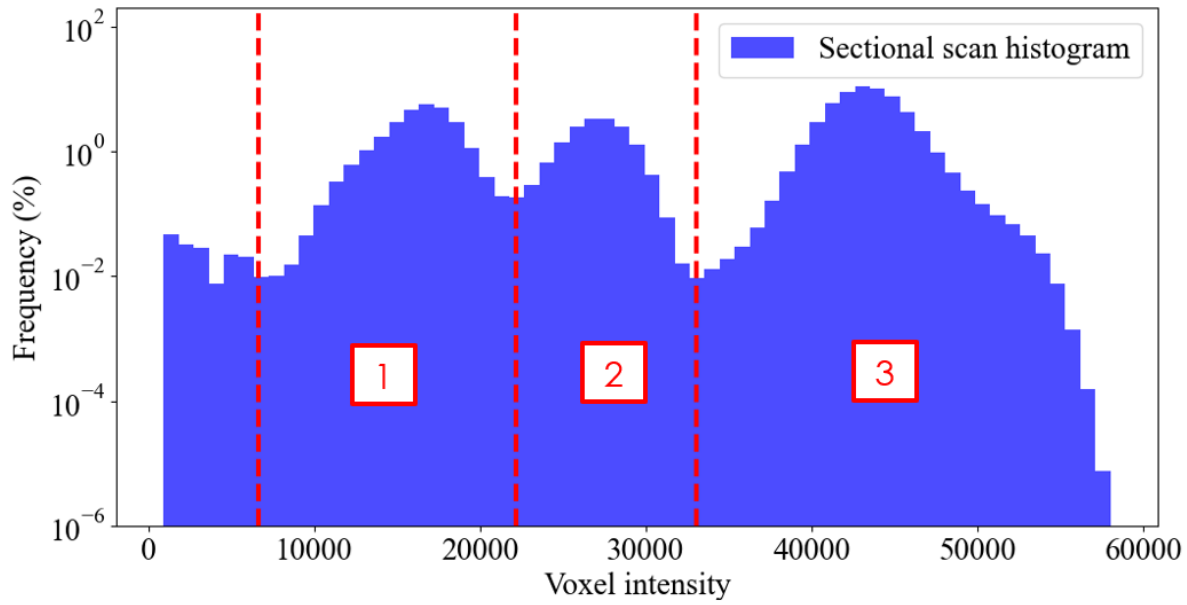

Figure 2.16. Thresholding of Sectional scan. 1 - grease, 2 - polyoxymethylene, and 3 - aluminum.

In figure (Figure 2.17) an visual evaluation of segmentation quality can be conducted. The figure includes representation of the Full scan, detail of Full scan (which corresponds to Sectional scan area) in grayscale, and ultimately, a segmented depiction of grease layer detail. This segmented detail will undergo additional analysis for geometry reconstruction purposes.

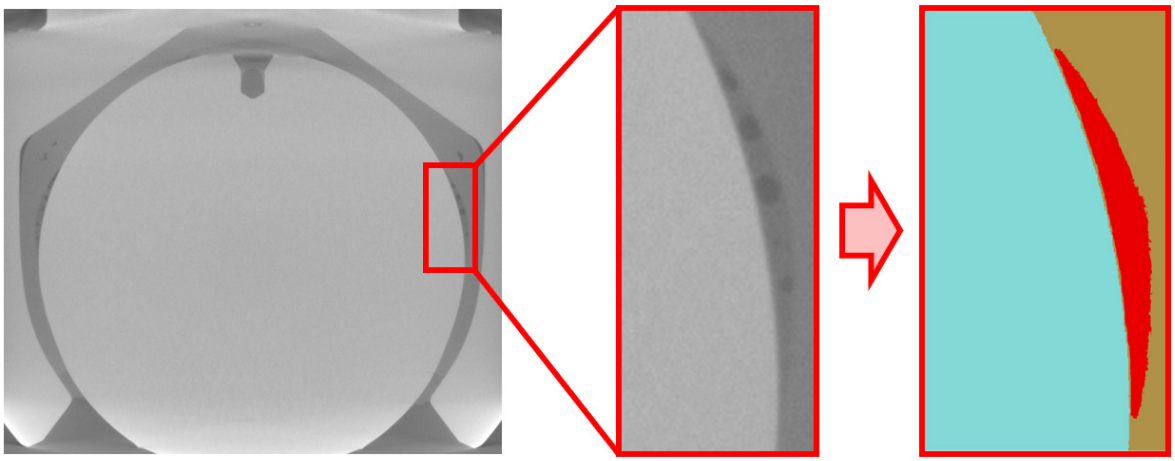

Figure 2.17. Segmentation of grease layer detail. Image before segmentation is shown at the left side. Image after segmentation is shown at the right side.

2.7.2 Watershed transformation

Watershed segmentation is region-based method that has its origins in mathematical morphology. The theory behind watershed is that every grayscale image can be viewed as tomographic surface, where high voxel intensity indicates peaks, while low voxel intensity indicates valleys.[40]
The segmentation itself consist of several steps and graphically can be displayed as in figure (Figure 2.18).

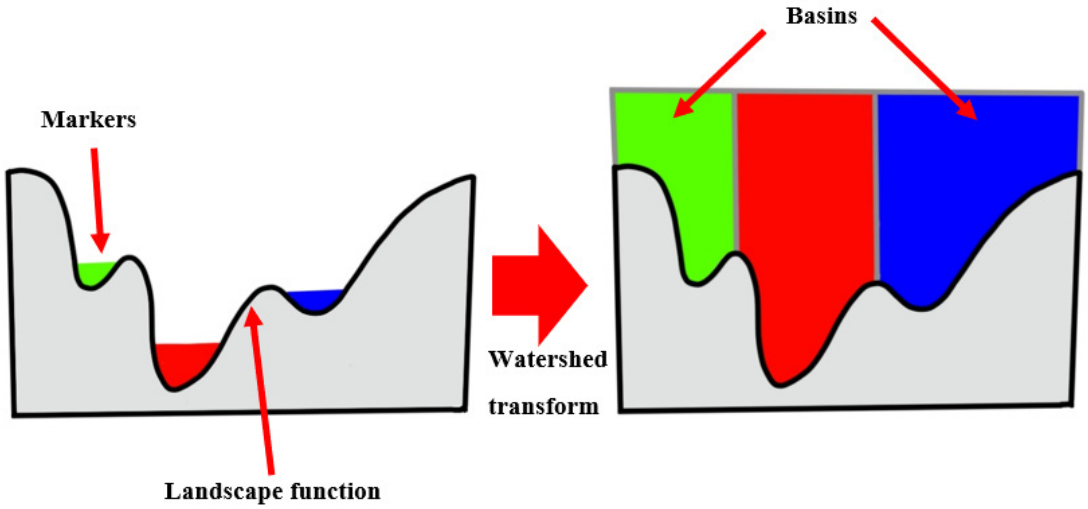

Figure 2.18. Principle of watershed transformation. On the left the initial configuration. On the right the final form of transformation.

Marker selection. This process is often done by thresholding already described in subsection (Subsection 2.7.1). In this case, the thresholding interval is not chosen to mark all air voxels directly, but to create the seeds - points where the flooding starts.

Landscape function selection. The landscape for this evaluation is created using 3D Sobel filter already described in subsection (Subsection 2.6.3).

Generation of Distance Map. Following the initial watershed transform, which effectively segments the air but leaves connected air pockets due to the image´s low resolution, a distance map is generated. In this process, the Region of Interest (ROI) including everything except air is chosen. Each pixel outside this ROI is assigned a value between 0 and 1, reflecting its distance from the nearest ROI pixel. Consequently, pixels closer to the ROI exhibit smaller values, while those farther away possess higher values.

New marker selection. In this step, markers representing air regions are chosen from the distance map instead of the original image. The goal is to ensure that the selected markers separate individual air pockets effectively, preventing their connection in the resulting image. This selection is crucial, as an inaccurate threshold interval may lead to the unintended splitting of a single pocket into multiple ones.

New landscape function selection. To facilitate the watershed transform, the landscape function is derived from the inverted distance map. Here, smaller values correspond to air pixels, while higher values represent all other pixels. This inversion ensures that valleys in the landscape function align with air pockets.

Mask selection. The mask, derived from the original watershed transform, sets the boundaries for the subsequent watershed transform. Without the mask, the watershed transform would expand indiscriminately, overlooking the spaces between air pockets.

Finally, the last watershed transformation can be conducted after all these steps. The result of this reconstruction is segmented air phase from the Full scan.

2.8 Geometry reconstruction

For grease layer geometry reconstruction, the outcomes from section (Section 2.7) can be utilized. Specifically, the results from subsection (Subsection 2.7.1) involve the segmentation of the grease layer from the Sectional scan. The measurement of the dimensions of the grease layer involved the following steps:

Separation of image. Every fifth image from the scan was isolated. This implies that measurements were taken along the vertical axis approximately every 50 μm based on pixel size.

Measurement of grease layer. On each isolated image, five measurements of the grease layer were taken at same positions. The specific positions can be referenced in figure (Figure 2.19), where the color legend is as follows: red represents grease, green denotes air, light blue corresponds to aluminum, and orange indicates polyoxymethylene.

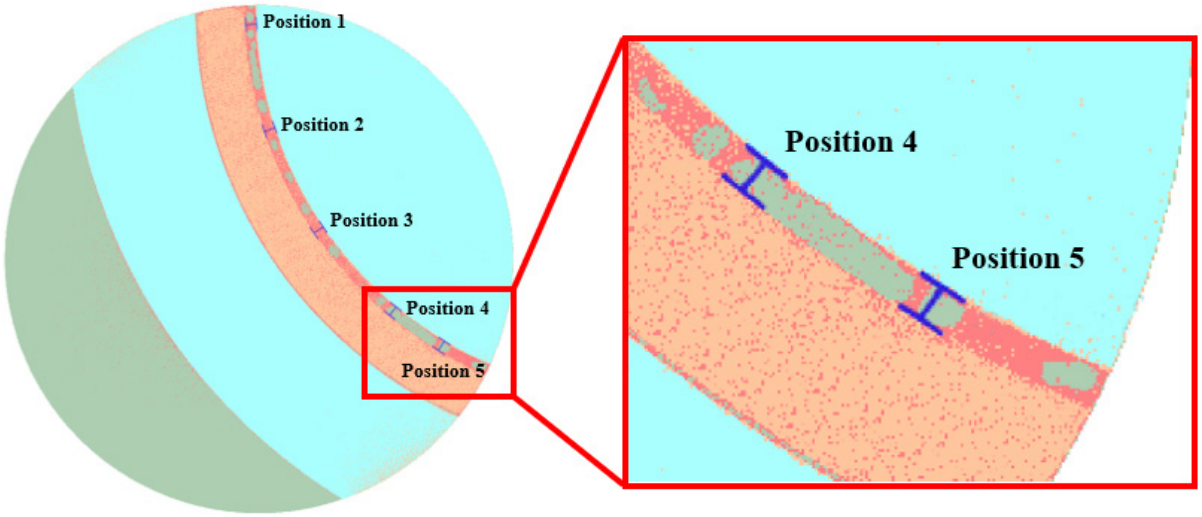

Figure 2.19. Position of measurement on the left, and detail of measurement on the right.

Measurement averaging. The five measurements were averaged to derive a single value for each separated image.

Smoothing of final values Following all measurements, the final geometry underwent smoothing using a spline to mitigate potential inaccuracies resulting from less-than-ideal phase separations. Inaccurate assignment of values (phases) to several pixels during separation may introduce noise to the geometry. The application of a spline to the measured data helps to prevent it.

Final position on thickness of grease layer is derived from the above procedure. Results can be seen in figure (Figure 2.20). The thickness showed in the normalized values (all values were divided by maximal thickness value) to ensure the confidentiality of the results. The grease covers approximately 60° of the entire ball pin (360°).

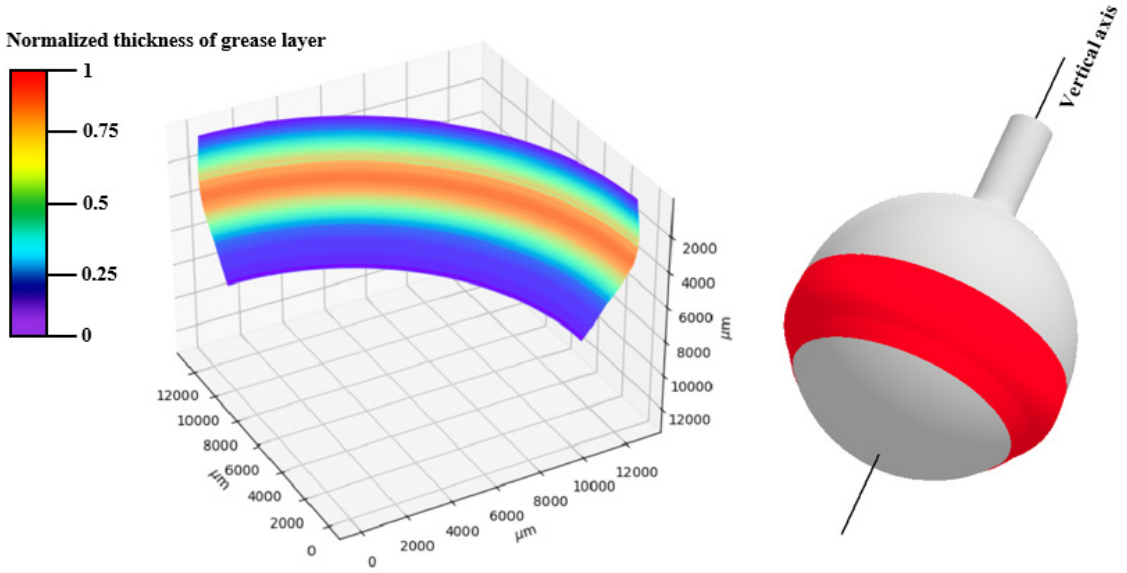

Figure 2.20. Thickness of grease layer shown at the chart on the left. Position of the grease layer on the ball pin on the right.

The grease layer includes air gaps, and the configuration and location of these gaps can be reconstructed based on the outcomes derived in subsection (Subsection 2.7.2). The watershed transformation results in the segmentation of air from the surrounding ball joint. The segmentation software employed enables the exportation of a mesh representing the precise geometry. To ensure accuracy during mesh export, the original mesh underwent Laplacian smoothing. The smoothed mesh is visualized in figure (Figure 2.21)

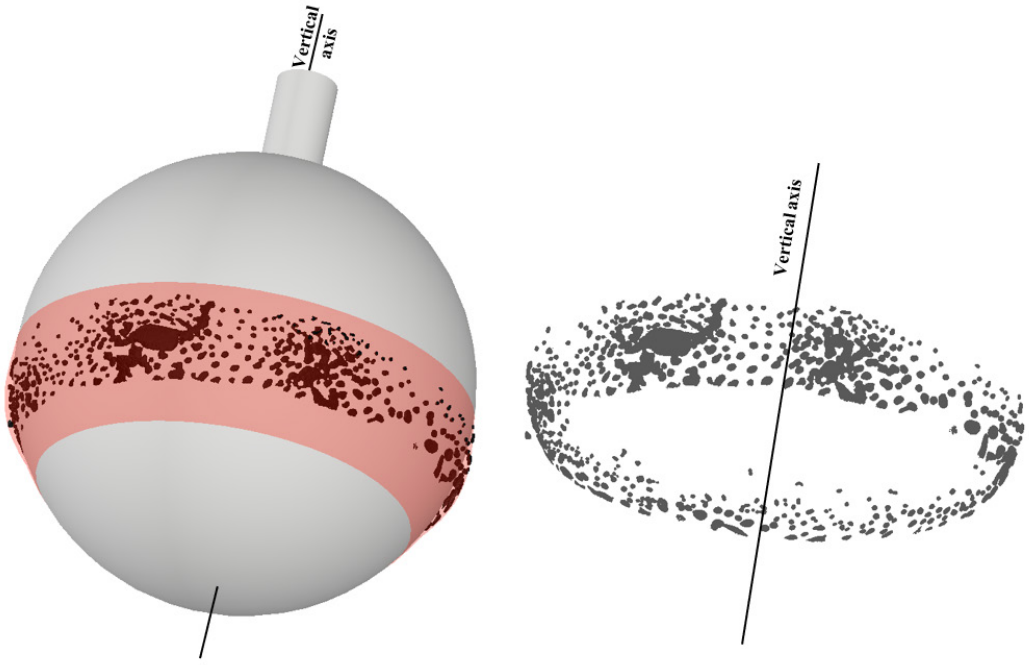

Figure 2.21. The full geometry (ball stud, grease layer and air gaps) shown at the left and air gaps only shown at the right.

It can be seen that the air is located mainly in the area of widest grease layer thickness. It´s probably because of the shape of the gap itself. The confuser shape can push air into places with a larger gap width. Another reason can be low resolution of scans itself. The minimum number of pixels in the narrowest point of the air pocket must be at least three to determine whether it is an air pocket or just noise or measurement inaccuracy. Since there are 4 pixels across the width of the grease layer in the narrowest points, and since the insensitivity of usually two pixels from the boundary of the two phases is slightly biased, it is not possible to determine whether it is grease or air.

By comparing the number of pixels it is possible to determine the percentage of air volume in the grease on the ball joint. That can be mathematically expressed as (Equation 2.13).

$$\frac{V_{air}}{V_{grease}} = \frac{N_{air}}{N_{grease}} = \frac{5231859}{22645803} \cdot 100\% = 23.103\% \tag{2.13}$$

Where: V (m^3) represents the volume of air or grease and N (-) represents the number of pixel labeled as air or grease.

The high amount of air in the grease layer may be due to the fact that the joint has not been moved properly after assembly, unlike mass-produced joints.

3 Material model

Fluids exhibit behaviors that can be categorized into two types: Newtonian and non-Newtonian. In the realm of Newtonian fluids, such as water and air, the viscosity remains constant regardless of the applied shear rate, aligning with Newton´s law of viscosity. On the contrary, non-Newtonian fluids like greases, food sauces, blood and paints defy this conventional behavior. These fluids dynamically alter their viscosity in response to external forces.

3.1 Newtonian behavior

Newtonian fluids adhere to Newton´s law of viscosity. This fundamental law states that the shear stress τ (Pa) within the fluid is directly proportional to the shear rate $\dot{\gamma}$ (s^{-1}), resulting in linear relationship expressed by the equation (Equation 3.1).

$$\tau = \eta \cdot \dot{\gamma} \tag{3.1}$$

Where: τ (Pa) represents shear stress, η $(Pa \cdot s)$ stands for dynamic viscosity and $\dot{\gamma}$ (s^{-1}) is the shear rate.

The behavior of fluid in rheology is often defined by flow curve and viscosity curve. The flow curve represents the relationship between shear stress τ (Pa) and shear rate $\dot{\gamma}$ (s^{-1}) for a liquid. It illustrates how the fluid responds to applied shear forces, showcasing the variations in shear stress as a function of shear rate. The flow curve is a fundamental tool in rheology, providing insights into the flow behavior of fluids under different conditions. The flow curve for Newtonian fluid is shown in figure (Figure 3.1).

The viscosity curve depicts how the dynamic viscosity η $(Pa \cdot s)$ of a fluid changes with varying shear rates $\dot{\gamma}$ (s^{-1}). This curve is crucial in understanding the fluid´s resistance to flow under different shear conditions. The viscosity curve for Newtonian fluid is shown in figure (Figure 3.1).

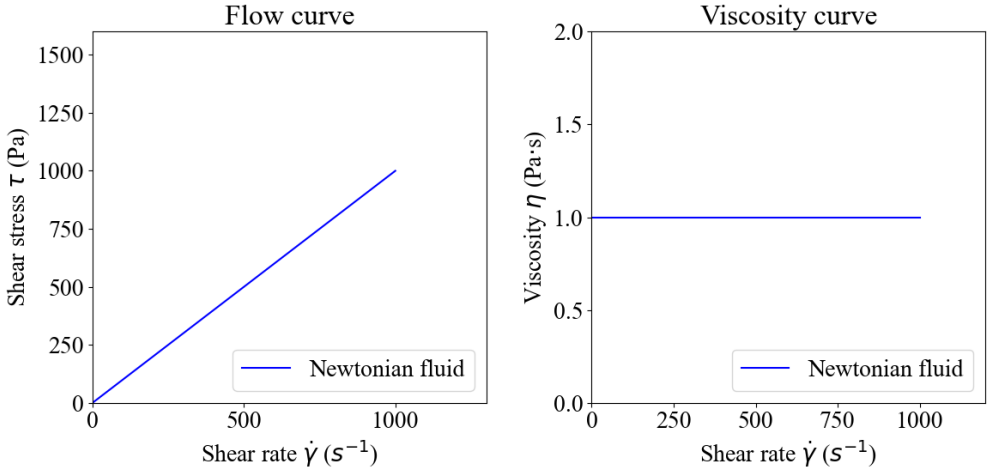

Figure 3.1. Flow curve and viscosity curve of Newtonian fluid.

3.2 Non-Newtonian behavior

Non-Newtonian fluids, on the other hand, exhibit a variable viscosity depending on the applied stress or shear rate or even the time. These fluids can be categorized into several types based on their response to shear. For the nonlinear curves, the slope at any point of the flow curve is called the apparent viscosity [41]. That can be mathematically expressed as (Equation 3.2).

$$\tau = \eta_a(\dot{\gamma}) \cdot \dot{\gamma} \tag{3.2}$$

Where: τ (Pa) represents shear stress, $\eta_a(\dot{\gamma})$ $(Pa \cdot s)$ stands for apparent viscosity which is function of shear rate and $\dot{\gamma}$ (s^{-1}) is the shear rate.

Non-Newtonian fluids can be categorized into several types based on their response to shear and time.

3.2.1 Shear-thinning fluids

Shear-thinning fluids, or pseudoplastic fluids, are a category of non-Newtonian fluids characterized by a reduction in viscosity as the shear rate rises. This implies that as the applied force or stress on the fluid increases, it becomes less resistant to flow, resulting in a lower viscosity.[42] That means that their shear stress τ (Pa) - shear rate $\dot{\gamma}$ (s^{-1}) dependency is non-linear with a zero intercept and a concave curve.[43]
Various non-Newtonian fluid models, such as the Power-Law model, Herschel-Bulkley model, and Cross model, can be employed to mathematically characterize pseudoplastic fluids. These models will be explored in greater detail in next section (Section 3.4).

Same as for Newtonian flow, the fluid can be characterized using flow and viscosity curve shown in figure (Figure 3.2).

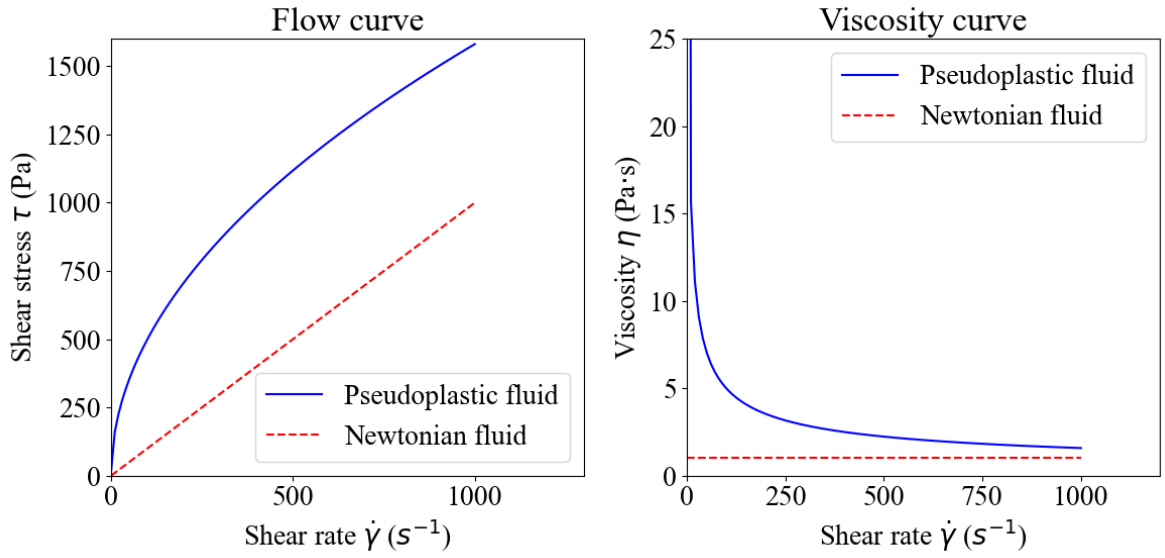

Figure 3.2. Flow and viscosity curve of Pseudoplastic fluid.

3.2.2 Shear-thickening fluids

Shear-thickening fluids, also referred to as dilatant fluids, are a type of non-Newtonian liquid characterized by an increase in viscosity as the shear rate rises. This means that as higher force or stress is applied to the fluid, its resistance to flow escalates, resulting in an elevation of viscosity. In this case the shear stress τ (Pa) - shear rate $\dot{\gamma}$ (s^{-1}) dependency for shear-thickening fluids is non-linear with a zero intercept, but the curve is convex.[43]

Similar to shear-thinning fluids, the behavior of shear-thickening fluids can be mathematically described by various models, such as the Power-Law, Herschel-Bulkley, and others,as explained in more detail in section (Section 3.4).

Same as for pseudoplastic fluids, the dilatant fluid can be characterized using flow and viscosity curve shown in figure (Figure 3.3).

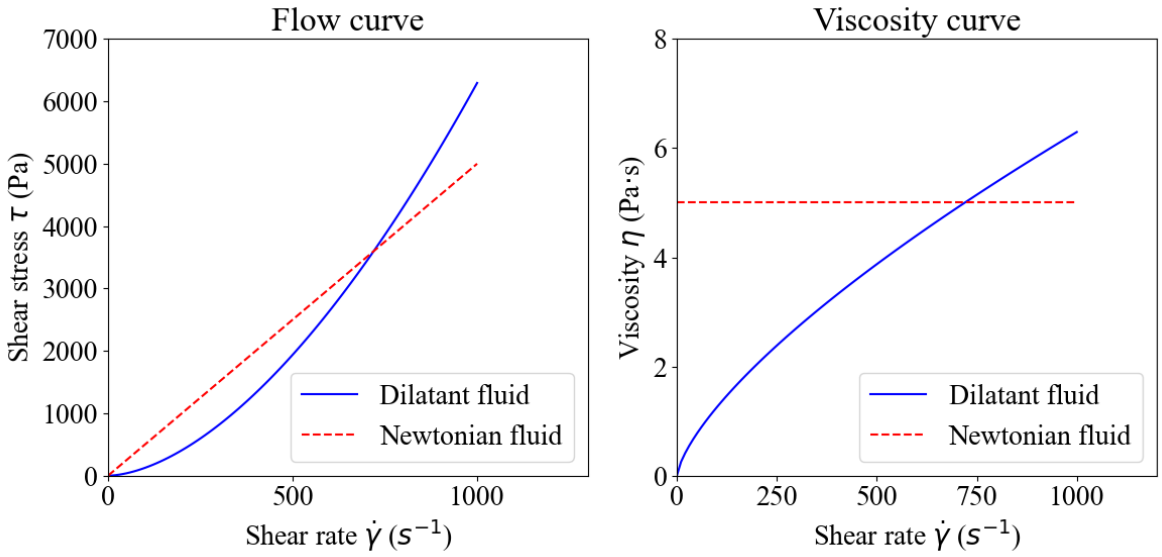

Figure 3.3. Flow and viscosity curve of Dilatant fluid.

3.2.3 Bingham fluids

Bingham fluids are type of Non-Newtonian fluids that behaves like a solid until a yield stress, also known as critical stress, is exceeded. After reaching the yield stress the Bingham fluid flows either like Newtonian viscous fluid, pseudoplastic fluid or dilatant fluid. That means that Bingham fluids are classified as viscoplastic materials because they exhibit both solid and liquid characteristics.[44]
The behavior of Bingham fluid that behave like Newtonian fluid after exceeding yield stress is described by the equation (Equation 3.3).

$$\tau = \tau_y + \eta \cdot \dot{\gamma} \tag{3.3}$$

Where: τ (Pa) represents shear stress, τ_y (Pa) is the yield stress, η $(Pa \cdot s)$ stands for dynamic viscosity and $\dot{\gamma}$ (s^{-1}) is the shear rate.

The fluid can be characterized using flow and viscosity curve shown in figure (Figure 3.4).

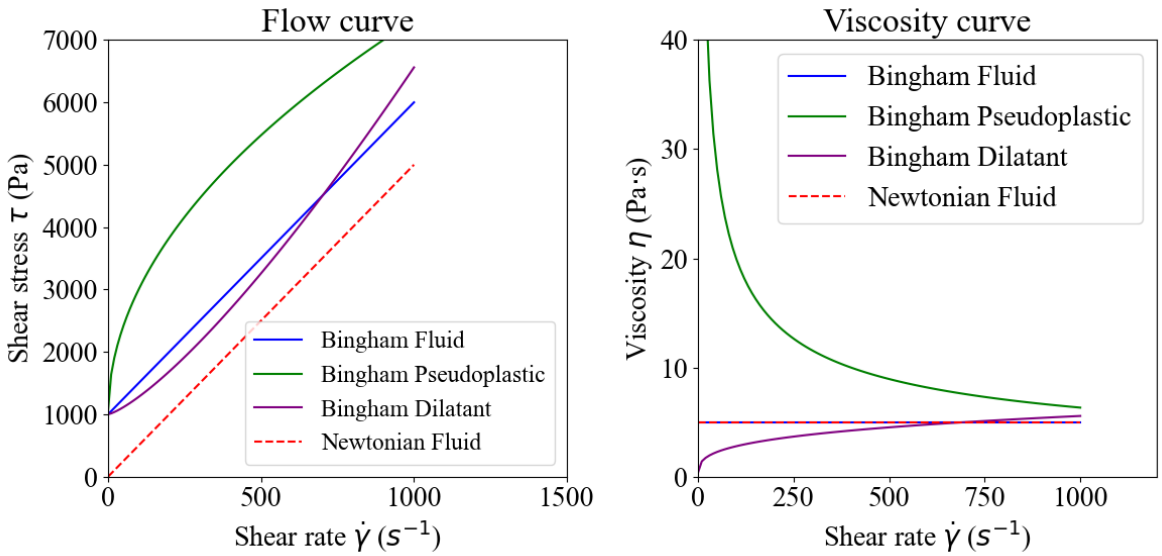

Figure 3.4. Flow and viscosity curve of Bingham fluid.

3.2.4 Thixotropic fluids

Typically, viscosity is viewed as a time-independent property. However, certain fluids, such as thixotropic fluids, exhibit distinctive rheological characteristics wherein viscosity decreases over time under constant shear stress. This implies that thixotropic fluids become less viscous when subjected to continuous shearing, yet they gradually revert to their original viscosity when left undisturbed.[43]

The fluid behavior can be best characterized using flow curve and viscosity $\eta(\dot{\gamma})$ - time (t s) dependency shown in figure (Figure 3.5).

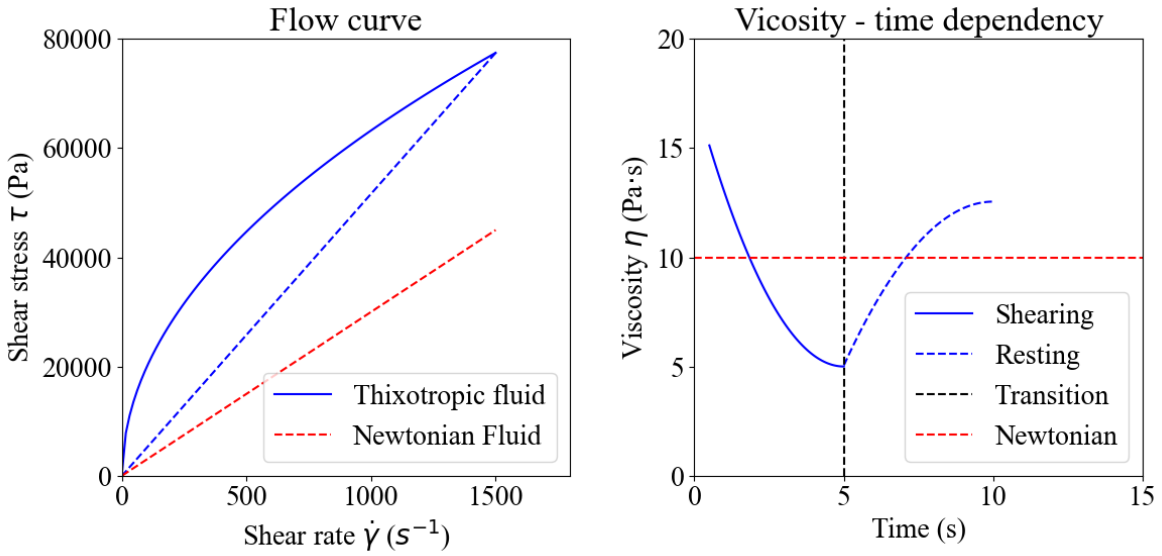

Figure 3.5. Flow curve and viscosity - time dependency of Thixotropic fluid.

3.2.5 Rheopectic fluids

Rheopectic fluids, opposed to thixotropic fluids, represent another category of non-Newtonian fluids exhibiting time-dependent viscosity. However, rheopectic behavior is defined by an increase in viscosity over time under constant shear stress, in contrast to the viscosity decrease observed in thixotropic fluids. Essentially, rheopectic fluids become more resistant to flow or more viscous as they undergo continuous shear stress. This behavior is reversible, and the viscosity decreases when the stress is removed.[43]

The fluid behavior can be best characterized using flow curve and viscosity $\eta(\dot{\gamma})$ $(Pa{\cdot}s)$ - time $(t\ s)$ dependency shown in figure (Figure 3.6).

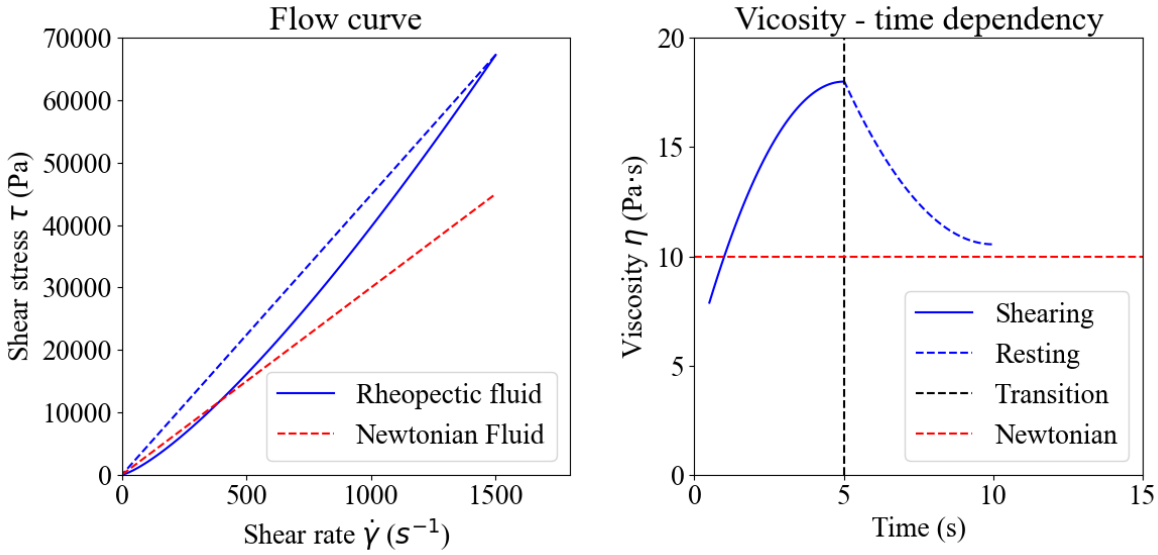

Figure 3.6. Flow curve and viscosity - time dependency of Rheopectic fluid.

3.3 Experimental data

To obtain a material model, the experimental data has to be measured. Data were provided by manufacturer itself. Rheological properties are measured on device called rheometer. There is several type of rheometers that can be used to measure viscosity and other properties, for example: plate-plate (a), cone-plate (b), rotating (c), oscillating piston (d), falling ball (e) and rolling ball viscosimeter (f).[43] The basic principle is shown in figure (Figure 3.7).

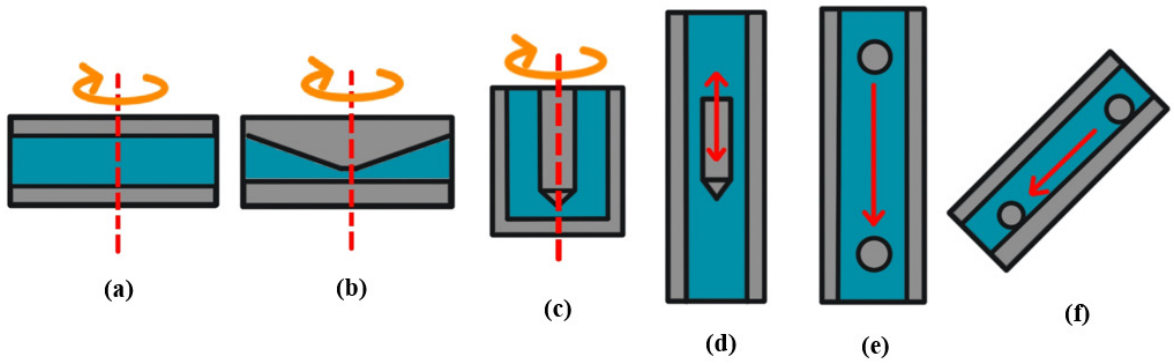

Figure 3.7. Typical commercially available viscosimeters. (a)(b)(c) - torque moment is measured, (d) - deflection is measured, (e)(f) - Time is measured.

In this case the cone-plate rheometer was used. Advantage of conical rotating disc is that shear rate is constant no matter the distance from the center. The gap between the plates is usually not adjustable, but that highly depend on manufacturer of the viscosimeter. [45] The shear stress is directly derived from measured torque moment of the upper conic disc.

The equation (Equation 3.4) defines viscosity as the derivative of shear stress with respect to shear rate. To enhance the accuracy and stability of Python scripts employed for determining material model constants, viscosity for a measured grease can be calculated through numerical methods. Utilizing two sets of data points allows for a combined fit, thereby improving the stability of the script.

$$\eta_a = \frac{d\tau}{d\dot{\gamma}} \Rightarrow \eta_i = \frac{\tau_i - \tau_{i+1}}{\dot{\gamma}_i - \dot{\gamma}_{i+1}} \tag{3.4}$$

Where: η_a $(Pa \cdot s)$ is the apparent viscosity, τ (Pa) represents shear stress, $\dot{\gamma}$ (s^{-1}) is the shear rate and i ranges from 1 to the total number of data point - 1.

The manufacturer of grease provided shear stress - shear rate data for two temperatures: 20 °C and 40 °C. Viscosity dependency on shear rate was calculated according to equation (Equation 3.4). Data both measured and calculated for temperature 20 °C are shown in figure (Figure 3.8).

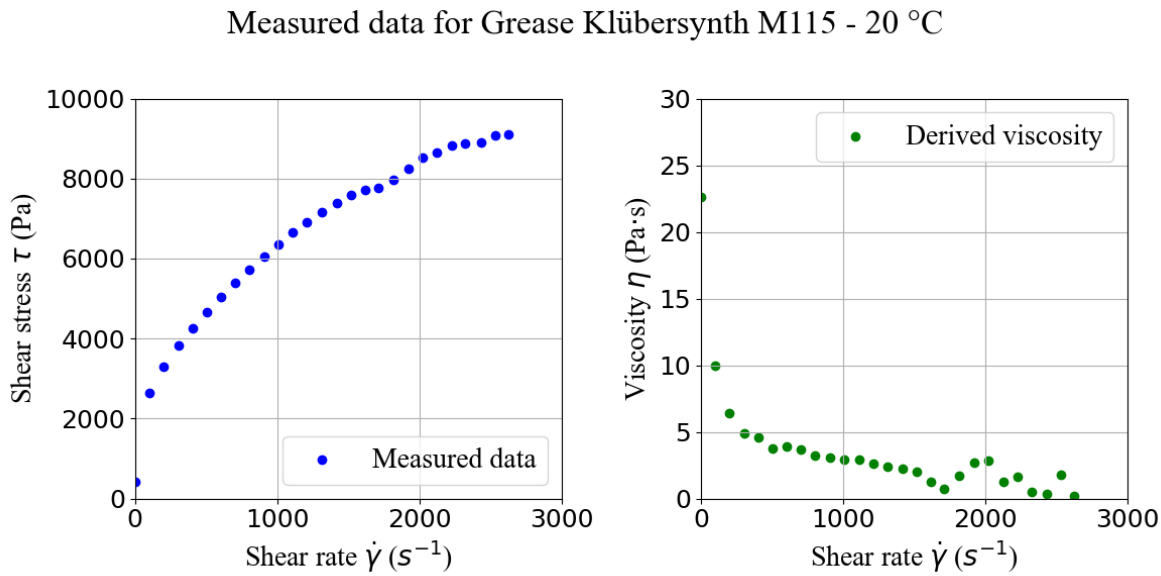

Figure 3.8. Experimental data provided by manufacturer for grease Klübersynth M115-04 at 20 °C. On the left shear stress - shear rate data, on the right viscosity - shear rate calculated data.

Just from visual inspection it can be concluded, that the grease exhibits pseudoplastic behavior and the fluid is with high probability a Bingham fluid, because of intersection with y-axis is non-zero.

Data both measured and calculated for temperature 40 °C are shown in figure (Figure 3.9).

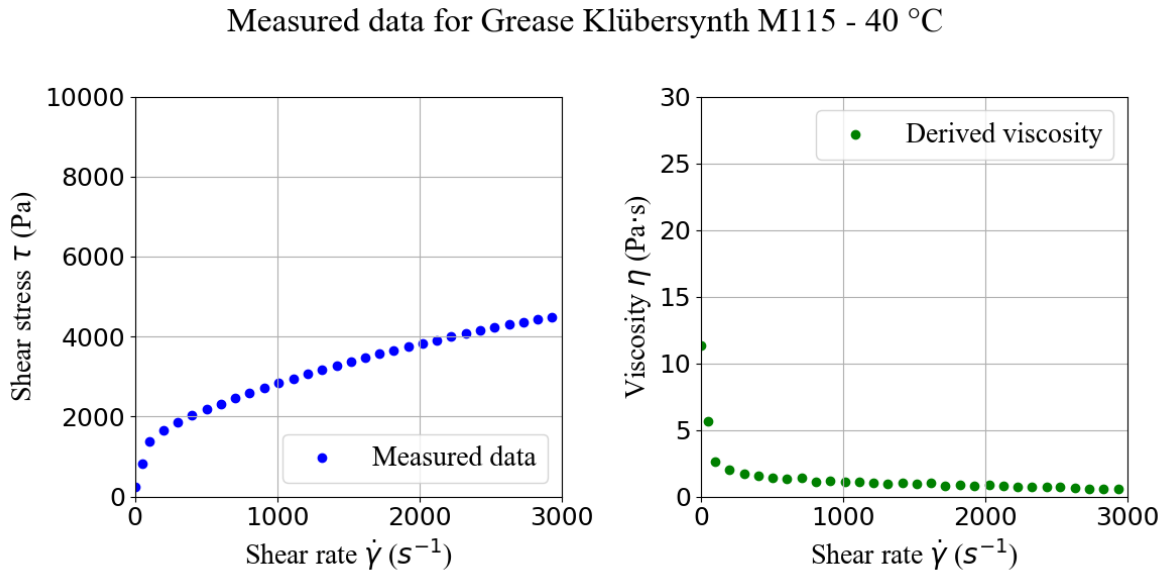

Figure 3.9. Experimental data provided by manufacturer for grease Klübersynth M115-04 at 40 °C. On the left shear stress - shear rate data, on the right viscosity - shear rate calculated data.

Measured data at 40 °C exhibits same behavior as data at room temperature. The fluid is also pseudoplastic nature. The intercept with y-axis is still non-zero, therefore grease behave like Bingham fluid even at 40 °C. The shear stress and viscosity at 40 °C can be estimated to be approximately half of shear stress and viscosity at 20 °C.

3.4 Non-Newtonian fluid model

The behavior of non-Newtonian fluids can be effectively captured by rheological models, which provide mathematical descriptions of the dependency between shear stress and shear rate, or in some cases, viscosity and shear rate.
In the literature, numerous rheological models exist, including the Bingham model, Power-Law (Ostwald–de Waele) model, Herschel-Bulkley model, Cross model, Carreau model, Casson model, Bi-viscous model, and others. [45]

In general, the apparent viscosity is a function of all three invariants of rate-to-deformation tensor, which can be defined as (Equation 3.5).[46]

$$\bar{\bar{D}} = \left(\frac{\partial u_j}{\partial x_i} + \frac{\partial u_i}{\partial x_j} \right) \tag{3.5}$$

Where: $\bar{\bar{D}}$ represents rate-to-deformation tensor, u_i is the velocity component in the i-th direction and x_j stands for spatial coordinate in the j-th direction.

Ansys Fluent, when modelling a non-Newtonian fluid, makes an assumption, that apparent viscosity is considered to be function of the shear rate only, in context of rate-to-deformation tensor.[47] Shear rate is related to the second invariant of rate-to-deformation tensor, and can be defined as (Equation 3.6).[46]

$$\dot{\gamma} = \sqrt{\frac{1}{2} \bar{\bar{D}} : \bar{\bar{D}}} \tag{3.6}$$

Where: $\dot{\gamma}$ (s^{-1}) stands for the shear rate, and $\bar{\bar{D}}$ represents rate-to-deformation tensor.

Viscosity is highly dependent on temperature. The dependence can be put into Ansys Fluent by including function H(T), known as Arrhenius law (Equation 3.7).

$$H(T) = exp \left[\alpha \cdot \left(\frac{1}{T - T_0} - \frac{1}{T_\alpha - T_0} \right) \right] \tag{3.7}$$

Where: H(T) represents Arrhenius law or temperature dependency, α (-) is ratio of the activation energy to the thermodynamic constant, T_α (K) is a reference temperature for which H(T) = 1, T_0 (K) is lowest thermodynamically acceptable and therefore is set to 0 by default, T (K) represents the current temperature.

Due to the lack of data provided by manufacturer of grease, the dependency of viscosity on temperature will be neglected, which can be mathematically expressed as (Equation 3.8). Instead of that, two separated models for grease will be done. One for room temperature 20 °C and one for temperature 40 °C.

$$H(T) = 1 \tag{3.8}$$

Where: H(T) represents Arrhenius law or temperature dependency.

Given the multitude of available models, this thesis will specifically concentrate on four models accessible in the Ansys Fluent software: Power-Law model, Herschel-Bulkley model, Carreau model and Cross model.

3.4.1 Power-Law model

Power-Law fluid model (also known as Ostwald de Waele fluid model) is a simple mathematical model used to describe fluids that exhibits pseudoplastic or dilatant behavior. The model can be mathematically expressed as (Equation 3.9).[48]

$$\tau = \eta_a \cdot \dot{\gamma} \tag{3.9}$$

Where: τ (Pa) represents shear stress, η_a $(Pa \cdot s)$ stands for apparent viscosity and $\dot{\gamma}$ (s^{-1}) is the shear rate.

The apparent viscosity is further defined by (Equation 3.10) where for isothermal flow the function H(T) = 1. [48] [47]

$$\eta_a = K \cdot \dot{\gamma}^{n-1} \cdot H(T) = K \cdot \dot{\gamma}^{n-1} \tag{3.10}$$

Where: η_a $(Pa \cdot s)$ stands for apparent viscosity, K $(Pa \cdot s^n)$ is the consistency index, $\dot{\gamma}$ (s^{-1}) stands for the shear rate, n (-) represents flow behavior index and H(T) is the temperature dependency, which is in this case equal to 1.

The Power-Law model is characterized by only two fitting constants, simplifying the fitting process compared to other models. The values of the consistency index K and flow behavior index n are determined by fitting experimental data of shear stress τ (Pa) - shear rate $\dot{\gamma}$ (s^{-1}).

The Python script for determining Power-Law constants is included in the appendixes, labeled as "Power-Law-fit" (Appendix C). This script utilizes a function that employs a Levenberg-Marquardt algorithm to determine the constants of a Power-Law material model, as detailed in the SciPy library documentation.[49]
The found constants of Power-Law model are listed in the table (Table 3.1) for both temperatures.

Table 3.1: Constants of Power-Law model for both temperatures 20 °C and 40 °C.

	Temperature 20 °C	**Temperature 40 °C**
Flow behavior index n (-)	0.403	0.4
Consistency index K ($Pa \cdot s^n$)	390.99	181.93
Coefficient of determination (-)	0.99952	0.99941

The high coefficient of determination (above 0.999) for both datasets indicates an excellent fit. The value of flow behavior index confirms that the grease have pseudoplastic behavior. By comparing the value of consistency index it can be concluded that the value of consistency index at 40 °C is approximately half than it´s value at 20 °C, thus viscosity of grease at 40 °C is approximately half than viscosity of grease at 20 °C.

The visual representation of fit is shown in figure (Figure 3.10).

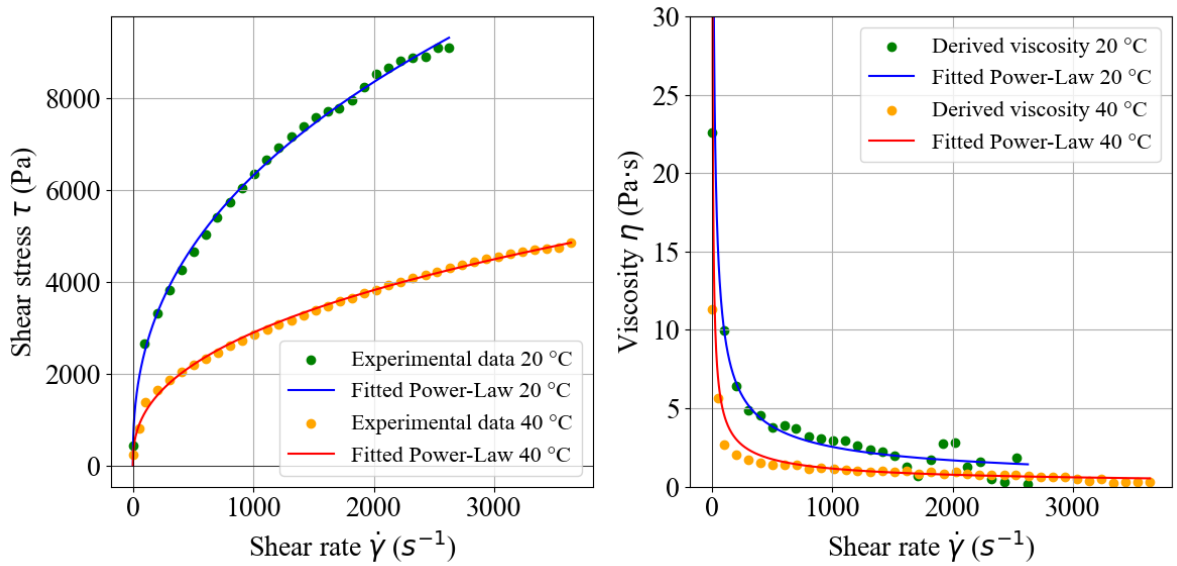

Figure 3.10. Visual representation of Power-Law fit for both temperatures. Flow curve on the left and viscosity curve on the right.

3.4.2 Herschel-Bulkley model

Herschel-Bulkley material model is another simple mathematical model. But in contrast to Power-Law model, it can also describe Bingham fluid behavior.

The Herschel-Bulkley model introduces a power-law relationship between shear stress and shear rate with the following equation (Equation 3.11).[45]

$$\tau = \tau_0 + K \cdot \dot{\gamma}^n \tag{3.11}$$

Where: τ_0 (Pa) represents yield stress, K $(Pa \cdot s^n)$ is the consistency index, $\dot{\gamma}$ (s^{-1}) stands for the shear rate and n (-) represents flow behavior index.

The apparent viscosity can be defined as two relationships, based on the fact if the shear rate $\dot{\gamma}$ is higher or lower than critical shear rate $\dot{\gamma}_c$ according the Ansys Fluent documentation. Where the critical shear rate is defined as (Equation 3.12). [47]

$$\dot{\gamma}_c = \frac{\tau_0}{\mu_0} \tag{3.12}$$

Where: $\dot{\gamma}_c$ (s^{-1}) is the critical shear rate, τ_0 (Pa) represents yield stress and μ_0 $(Pa \cdot s)$ is finite representation of viscosity at very low shear rates.

The viscosity parameter μ_0 $(Pa \cdot s)$ signifies the viscosity value considered by Ansys Fluent in its calculations, serving as a finite representation instead of an extremely high viscosity value when the shear rate is zero. [47]

For $\dot{\gamma} > \dot{\gamma}_c$ the apparent viscosity can be calculated according to (Equation 3.13).[47]

$$\eta_a = \frac{\tau_0}{\dot{\gamma}} + K \cdot \left(\frac{\dot{\gamma}}{\dot{\gamma}_c}\right)^{n-1} \tag{3.13}$$

Where: η_a $(Pa \cdot s)$ stands for apparent viscosity, τ_0 (Pa) represents yield stress, K $(Pa \cdot s^n)$ is the consistency index, $\dot{\gamma}$ (s^{-1}) stands for the shear rate, $\dot{\gamma}_c$ (s^{-1}) represents the critical shear rate and n (-) represents flow behavior index.

For $\dot{\gamma} < \dot{\gamma}_c$ the apparent viscosity can be calculated according to (Equation 3.14).[47]

$$\eta_a = \tau_0 \cdot \frac{\left(2 - \frac{\dot{\gamma}}{\dot{\gamma}_c}\right)}{\dot{\gamma}_c} + K \cdot \left[(2-n) + (n-1) \cdot \frac{\dot{\gamma}}{\dot{\gamma}_c}\right] \tag{3.14}$$

Where: η_a $(Pa \cdot s)$ stands for apparent viscosity, τ_0 (Pa) represents yield stress, K $(Pa \cdot s^n)$ is the consistency index, $\dot{\gamma}$ (s^{-1}) stands for the shear rate, $\dot{\gamma}_c$ (s^{-1}) represents the critical shear rate and n (-) represents flow behavior index.

The Herschel-Bulkley model is characterized by three fitting constants. Conventional approach is to estimate a value of yield stress τ_0 (Pa) and then to solve the resultant linear problem to find the other parameters [50].

The paper by Mullineux et al. [50] introduces an alternative method that simplifies the conventional approach. The new approach involves deriving a function $\bar{F}(n)$ (Equation 3.15) in which the flow behavior index n serves as the root [50]. This method facilitates the determination of the flow behavior index, and once obtained, the other two constants can be straightforwardly determined.

$$\bar{F}(n) = \frac{1}{X^{3 \cdot n} \cdot Y} \begin{bmatrix} m & \sum x^n & \sum x^n \cdot [ln(x) - ln(X)] \\ \sum x^n & \sum x^{2 \cdot n} & \sum x^{2 \cdot n} \cdot [ln(x) - ln(X)] \\ \sum y & \sum x^n \cdot y & \sum x^n \cdot y \cdot [ln(x) - ln(X)] \end{bmatrix} \tag{3.15}$$

Where: m (-) is the number of data points, X (-) and Y (-) are constants used to scale data values x_i and y_i, n is the flow behavior index.

This approach was used to determine the value of flow behavior index on the experimental data. The behavior of the determinant of the function $\bar{F}(n)$ for the experimental data for both temperatures can be seen in figure (Figure 3.11).

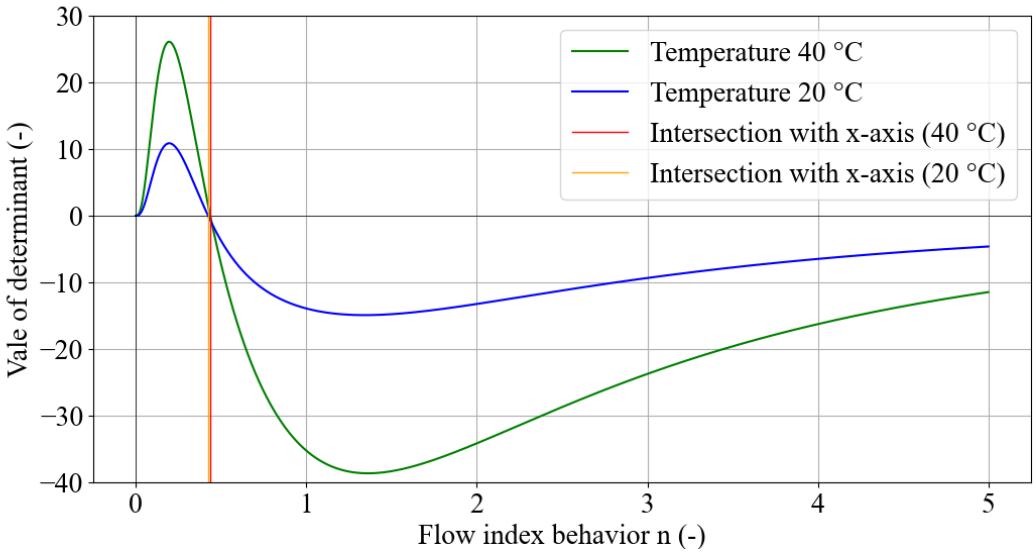

Figure 3.11. Determinant of the function $\bar{F}(n)$ vs. flow behavior index n (-) for both temperatures.

It can be shown that the function $\bar{F}(n)$ is zero, when flow behavior index is zero and infinite, while it initially becomes positive and with high values of flow behavior index the function is negative. Thus the root has to exist. The proof is presented in paper by Mullineux et al. [50]. The root of a function $\bar{F}(n)$ can be found as intersection with x-axis as shown in figure (Figure 3.11).
Fitting the Herschel-Bulkley model is now reduced to finding two constants and the problem becomes linear. The Python script for determining all Herschel-Bulkley constants is included in the appendixes, labeled as "Herschel-Bulkley-fit" (Appendix B). This script utilizes a function that employs a Levenberg-Marquardt algorithm to determine the constants of a Herschel-Bulkley material model, as detailed in the SciPy library documentation.[49]

The found Herschel-Bulkley model constants are listed in the table (Table 3.2) for both temperatures.

Table 3.2: Constants of Herschel-Bulkley model for both temperatures 20 °C and 40 °C.

	Temperature 20 °C	**Temperature 40 °C**
Yield stress τ_0 (Pa)	279.16	228.87
Flow behavior index n (-)	0.424	0.436
Consistency index K $(Pa \cdot s^n)$	322.69	130.05
Critical shear stress τ (Pa)	2652.09	814.34
Critical shear rate $\dot{\gamma}$ (s^{-1})	98.48	50.55
Coefficient of determination (-)	0.99962	0.99962

The high coefficient of determination (above 0.999) for both datasets indicates an excellent fit. Flow behavior index is almost same for both temperatures as it should be. Visual representation of Herschel-Bulkley fit is shown in figure (Figure 3.12).

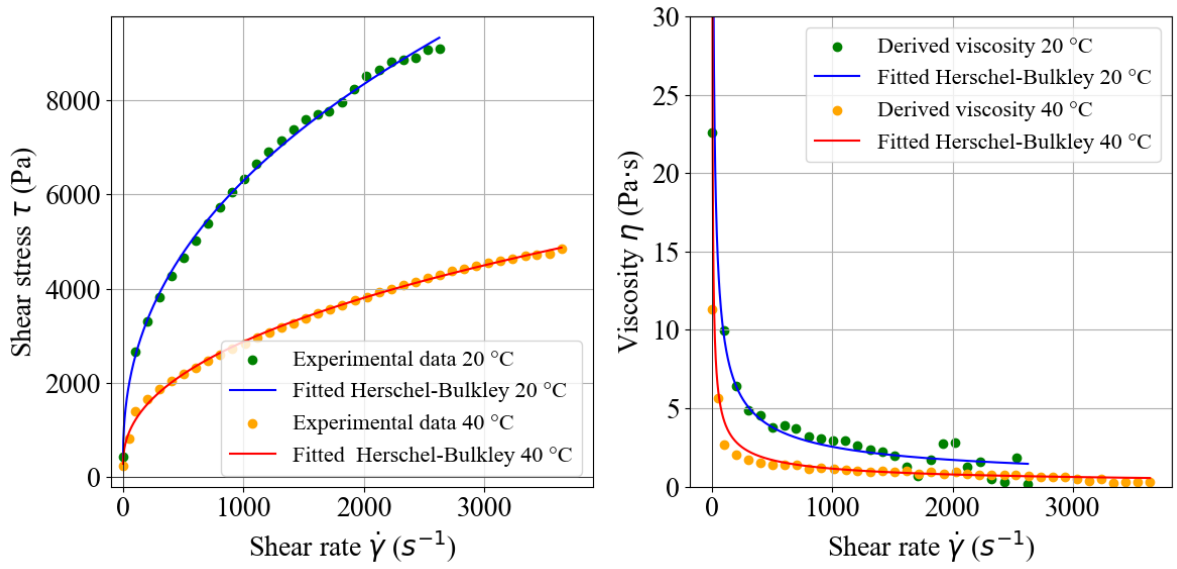

Figure 3.12. Visual representation of Herschel-Bulkley fit for both temperatures. Flow curve on the left and viscosity curve on the right.

3.4.3 Carreau model

Carreau material model is one of more complex models that allows for the representation of various flow behaviors, including the transition from Newtonian to non-Newtonian behavior at different shear rates. Mathematically, the Carreau model can be described as (Equation 3.16).[45]

$$\eta(\dot{\gamma}) = \eta_\infty + (\eta_0 - \eta_\infty)\left[1 + (\lambda \cdot \dot{\gamma})^2\right]^{\frac{n-1}{2}} \tag{3.16}$$

Where: $\eta(\dot{\gamma})$ $(Pa \cdot s)$ represents viscosity dependent on the shear rate, η_∞ $(Pa \cdot s)$ is the viscosity at the infinite shear rate, η_0 $(Pa \cdot s)$ describes the viscosity at zero shear

rate, λ (s) is the time constant, n (-) represents the flow behavior index and $\dot{\gamma}$ (s^{-1}) is the shear rate.

The Carreau model has four constants to find. To make the fit process simpler, the viscosity in infinite shear rate η_∞ is assumed to be zero. This assumption can be done, because the shear stress - shear rate data are not provided by the manufacturer in the range necessary to find this value. The viscosity at the zero shear rate η_0 is assumed to be smaller than 100 $Pa \cdot s$. Because the grease is probably the Bingham fluid the viscosity at zero shear rate should be extremely high value. To make the fit process stable, the maximum value is set to finite value. Mathematically expressed as (Equation 3.17) (Equation 3.18).

$$\eta_\infty = 0 \quad Pa \cdot s \tag{3.17}$$

$$\eta_0 < 100 \quad Pa \cdot s \tag{3.18}$$

The Python script for determining Carreau constants with given assumptions (Equation 3.17) (Equation 3.18) is included in the appendixes, labeled as "Carreau-fit" (Appendix C). This script utilizes a function that employs a Levenberg-Marquardt algorithm to determine the constants of a Carreau material model, as detailed in the SciPy library documentation [49].

The found constants of Carreau model are listed in table (Table 3.3) for both temperatures.

Table 3.3: Constants of Carreau model for both temperatures 20 °C and 40 °C.

	Temperature 20 °C	**Temperature 40 °C**
Time constant λ (s)	0.33297	1.3908
Flow behavior index n (-)	0.368	0.385
Zero shear rate viscosity η_0 ($Pa \cdot s$)	100	100
Infinite shear rate viscosity η_∞ ($Pa \cdot s$)	0	0
Coefficient of determination (-)	0.99639	0.99583

High coefficient of determination (above 0.99) indicates a very good fit for both temperatures for Carreau model. The infinite shear viscosity is equal zero for both temperatures, which corresponds with the established assumption (Equation 3.17). The zero shear rate viscosity is equal $\eta_0 = 100\ Pa \cdot s$ which satisfies the assumption (Equation 3.18). The maximum possible value for viscosity at zero shear rate has been reached, which indicates that the viscosity could be higher. But considering that this value is only important in very small values of shear rate, this fact can be neglected. [51]

Visual representation of Carreau fit is shown in figure (Figure 3.13).

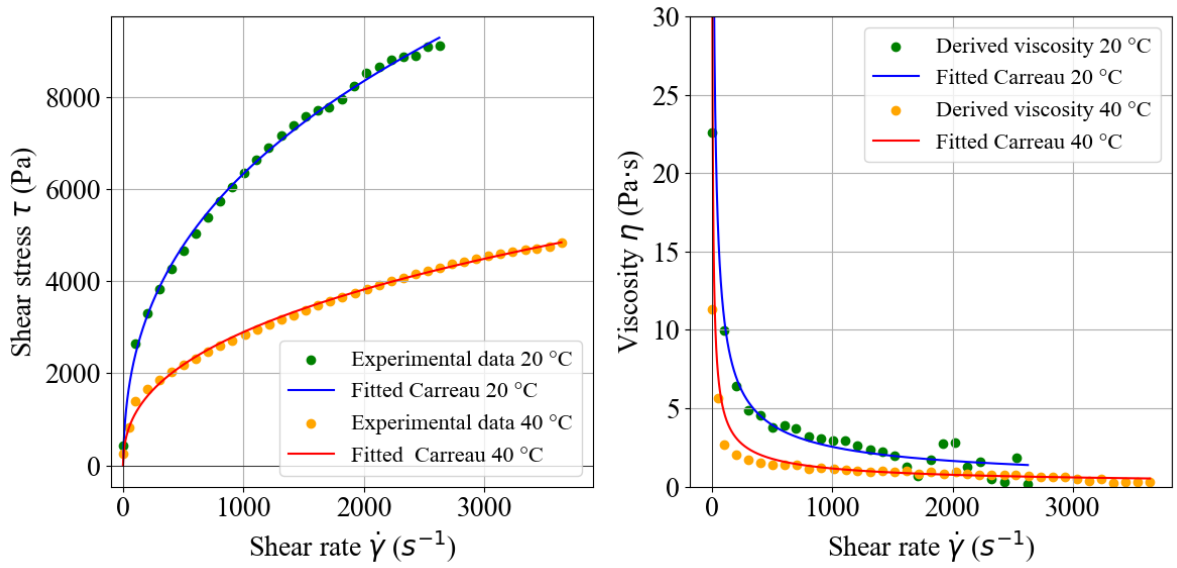

Figure 3.13. Visual representation of Carreau fit for both temperatures. Flow curve on the left and viscosity curve on the right.

The Carreau model defines viscosity over the entire shear rate range. Thus, the viscosity is often shown in the logarithmic scale. This curve is shown in figure (Figure 3.14).

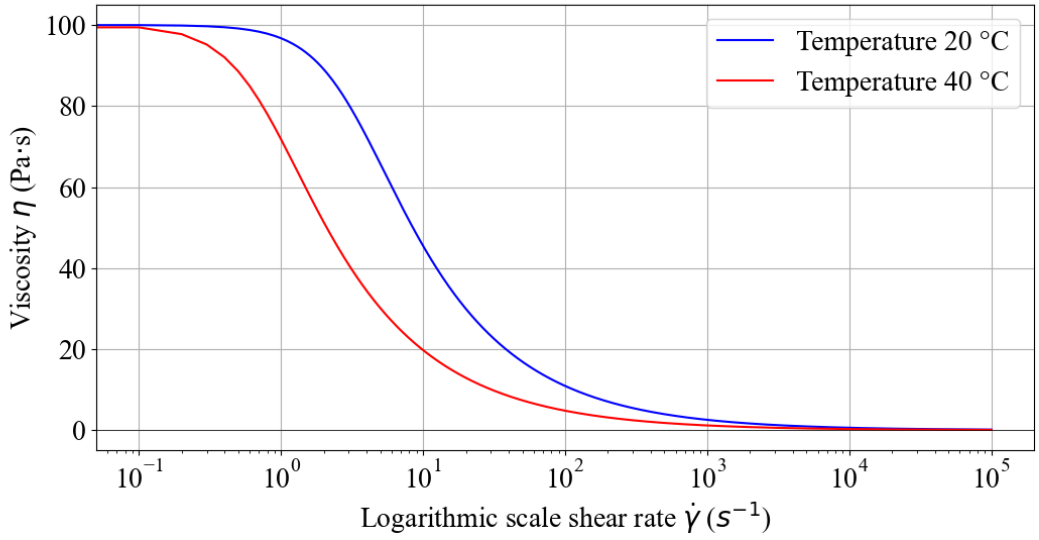

Figure 3.14. Visual representation of Carreau fit in logarithmic scale for both temperatures.

The figure reveals that the Carreau fluid exhibits Newtonian behavior at shear rates approximately $0 < \dot{\gamma} < 0.5\,s^{-1}$ and $\dot{\gamma} > 10^4\,s^{-1}$ for both temperatures. Within this range, the Carreau fluid behaves as a Power-Law fluid.

3.4.4 Cross model

Cross model, similarly to Carreau model, describes both Newtonian and pseudoplastic behavior of fluids. Mathematically, the Cross model can be described as (Equation 3.19).[52]

$$\frac{\eta_a - \eta_\infty}{\eta_0 - \eta_\infty} = \frac{1}{1 + (\lambda \cdot \dot{\gamma})^{1-n}} \tag{3.19}$$

Where: η_a $(Pa \cdot s)$ is the apparent viscosity, η_∞ $(Pa \cdot s)$ represents viscosity at infinite shear rate, η_0 $(Pa \cdot s)$ describes the viscosity at zero shear rate, λ (s) is the time constant and n (-) represents the flow behavior index.

Same as for Carreau model, the assumption of zero viscosity at infinity shear rate can be employed, because of lack of provided data at very high shear rate. The assumption is represented by the equation (Equation 3.20).

$$\eta_\infty = 0 \quad Pa \cdot s \tag{3.20}$$

Assuming the negligible infinity shear rate viscosity the Cross model equation can be written as (Equation 3.21). This way only three constants need to be found for Cross model, which greatly speeds up the process of finding them.

$$\eta_a = \frac{\eta_0}{1 + (\lambda \cdot \dot{\gamma})^{1-n}} \tag{3.21}$$

Where: η_a $(Pa \cdot s)$ describe the apparent viscosity, η_0 $(Pa \cdot s)$ represents the viscosity at zero shear rate, λ (s) is the time constant and n (-) represents the flow behavior index.

Second assumption can be made for zero shear rate viscosity. Same as for Carreau model, the viscosity tends to go to extremely high value, which is not numerically possible. To ensure the stability of the fitting process, the assumption (Equation 3.22) is introduced, capping the maximum value at a finite level.

$$\eta_0 = 100 \quad Pa \cdot s \tag{3.22}$$

The python script for determining Cross model constants with given assumptions (Equation 3.20)(Equation 3.22) is included in the appendixes, labeled as "Cross-fit" (Appendix D). This script utilizes a function that employs a Levenberg-Marquardt algorithm to determine the constants of a Cross model, as detailed in the SciPy library documentation.[49]

The found constants of Cross model are listed in the table (Table 3.4) for both temperatures.

Table 3.4: Constants of Cross model for both temperatures 20 °C and 40 °C.

	Temperature 20 °C	**Temperature 40 °C**
Time constant λ (s)	0.18289	0.92507
Flow behavior index n (-)	0.301	0.351
Zero shear rate viscosity η_0 $(Pa \cdot s)$	100	100
Infinite shear rate viscosity η_∞ $(Pa \cdot s)$	0	0
Coefficient of determination (-)	0.99573	0.99489

High coefficient of determination (above 0.99) indicates a very good fit for both temperatures for Cross model.The infinite shear viscosity is equal zero for both temperatures, which corresponds with the established assumption (Equation 3.20). The zero shear rate viscosity is equal $\eta_0 = 100\ Pa \cdot s$ which satisfies the assumption (Equation 3.22). The attained viscosity at zero shear rate represents the maximum achievable value, suggesting the potential for even higher viscosity. However, given its significance only at very low values, this observation can be disregarded.[51]

Visual representation of Cross fit is shown in figure (Figure 3.15).

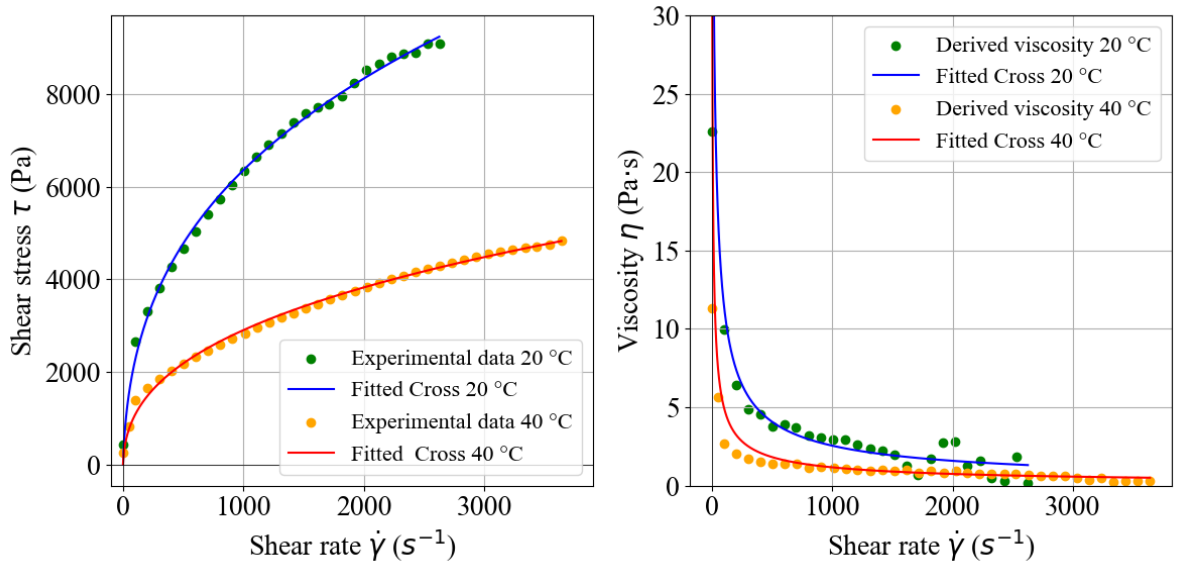

Figure 3.15. Visual representation of Cross fit for both temperatures. Flow curve on the left and viscosity curve on the right.

The Cross model defines viscosity over the entire shear rate range. Thus, the viscosity is often shown in the logarithmic scale. This curve is shown in figure (Figure 3.16)

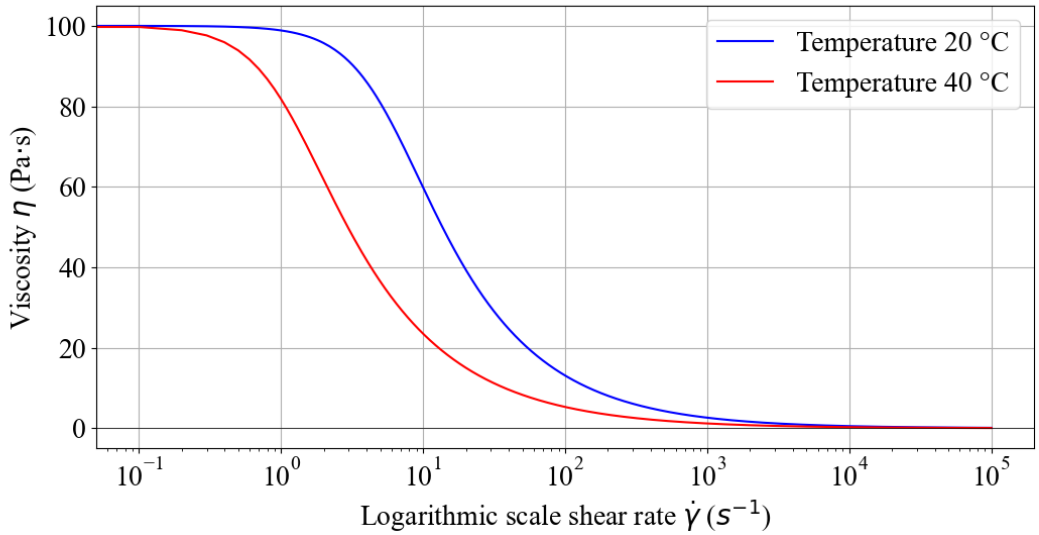

Figure 3.16. Visual representation of Cross fit in logarithmic scale for both temperatures.

The figure illustrates that the Cross fluid displays Newtonian characteristics at shear rates around $0 < \dot{\gamma} < 0.5\,s^{-1}$ and $\dot{\gamma} > 10^4\,s^{-1}$ for both temperatures. Within this interval, the fluid follows a Power-Law behavior. This aligns with the conclusion drawn from the Carreau model.

3.5 Comparison of non-Newtonian fluid models

To determine the quality of the fit, the coefficient of determination was used. The coefficient of determination, often denoted as R^2 (-), is a statistical measure that represents the proportion of the variance in the dependent variable that is predictable from the independent variable. It can be mathematically expressed as (Equation 3.23). [53]

$$R^2 = \frac{The\ sum\ of\ the\ squares\ of\ the\ regression}{The\ total\ sum\ of\ squares} = \frac{\sum_{i=1}^{n}(\hat{Y}_i - \bar{Y})^2}{\sum_{i=1}^{n}(Y_i - \bar{Y})^2} \tag{3.23}$$

Where: n (-) is the total number of data points, $\hat{Y}_i$ (-) represents the predicted value of the dependent variable for the i-th observation based on the regression model, $\bar{Y}$ (-) is the mean of the observed values of the dependent variable and Y_i is the actual value of the dependent variable for the i-th observation.

The coefficient of determination ranges from 0 to 1, or 0 to 100 % when presented as a percentage. A higher value indicates better fit.

The table (Table 3.5) contains the values of coefficient of determination, presented in percentage values, for all non-Newtonian fluid models described in section (Section 3.4).

Table 3.5: Values of coefficient of determination for every non-Newtonian fluid model at both temperatures, presented in percentage values.

Coefficient of determination		
	Temperature 20 °C	**Temperature 40 °C**
Power-Law model	99.952 %	99.941 %
Herschel-Bulkley model	99.962 %	99.962 %
Carreau model	99.639 %	99.583 %
Cross model	99.573 %	99.489 %

The high percentage values, ranging from 99.489 % to 99.962 %, indicate a strong correlation between the predicted values from the fluid models and the actual experimental observations. This suggests that the selected non-Newtonian fluid models (Power-Law, Herschel-Bulkley, Carreau, and Cross models) are highly effective in representing the rheological behavior of the fluids at both temperatures. The consistency of high coefficient of determination values across different models and temperatures reflects the robustness and reliability of these models in capturing the complex behavior of non-Newtonian fluids under the specified conditions.

Because all models exhibit strong correlations with experimental observations, the determination of the most suitable model involves a further evaluation. Recognizing the complexity of non-Newtonian fluid behavior, an experimental investigation was conducted to refine the model selection. The experiment entailed sliding one plate against another steady plate, to quantify the force generated by shearing the grease. This empirical approach aims to closely simulate real-world conditions and provide insight into the fluid´s response under shear. Furthermore, the study will leverage numerical simulations in Ansys Fluent to complement the experimental findings. The combination of experimental data and computational modeling will offer a comprehensive understanding of the non-Newtonian fluid´s rheological characteristics. The appropriateness of each model will be assessed based on their ability to accurately predict the observed forces in this specific shearing scenario, aiding in the final determination of the most suitable model for the study.

4 Experiment

The purpose of the experimental study is to measure the force generated between two plates - one steady and one sliding in a single direction at a specified height, with the gap between them filled with grease. The force arises from shearing the grease, a phenomenon that can be explained by Couette´s flow model.

4.1 Couette flow

Couette flow is a fundamental fluid dynamics concept that describes the flow of a viscous fluid between two parallel plates with one plate moving relative to the other. In a Couette flow setup, there are two parallel plates separated by a certain distance, and a fluid is placed between them. One of the plates is kept stationary, while the other is set in motion with a constant velocity. This motion induces shear forces within the fluid, leading to a velocity gradient across the gap between the plates. The Couette flow is shown in figure (Figure 4.1).

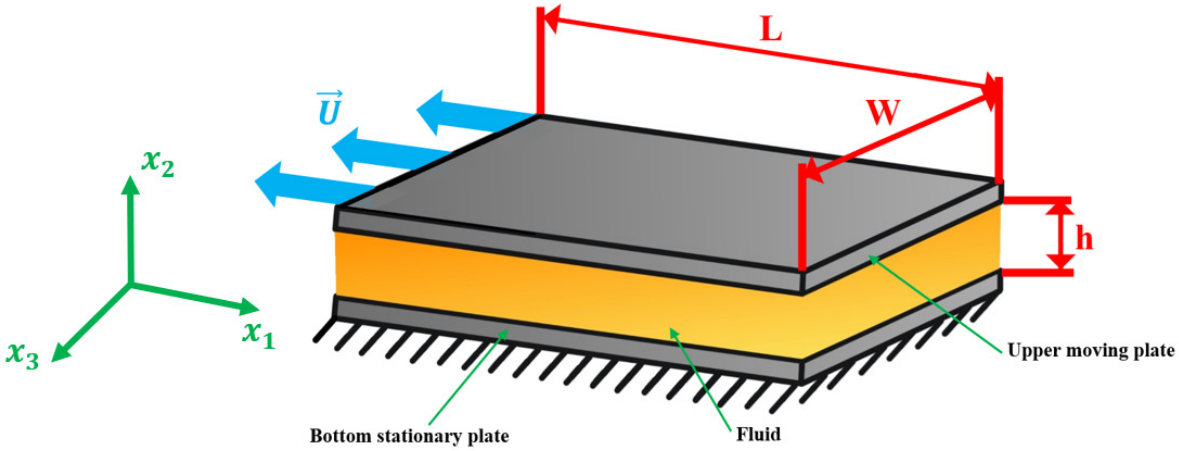

Figure 4.1. The Couette flow - Orange fluid between stationary and moving plate.

The Navier-Stokes equation (Equation 4.1) serves as the initial step in obtaining the analytical solution of Couette flow.

$$\frac{\partial v_i}{\partial t} + v_j \frac{\partial v_i}{\partial x_j} = -\frac{1}{\rho} \cdot \frac{\partial p}{\partial x_i} + \nu \cdot \frac{\partial^2 v_i}{\partial x_j \partial x_j} + a_i \tag{4.1}$$

Where: v_i represents the i-th component of the velocity vector, x_i is the i-th coordinate direction, p is the pressure, ρ represents the fluid density, ν is the kinematic viscosity and f_i represents the external forces acting on the fluid in the i-th direction.

To simplify the mathematical description, the flow is usually analyzed under steady-state condition, meaning the flow variables do not change with time. With this assumption the equation (Equation 4.1) simplify to (Equation 4.2).

$$v_j \frac{\partial v_i}{\partial x_j} = -\frac{1}{\rho} \cdot \frac{\partial p}{\partial x_i} + \nu \cdot \frac{\partial^2 v_i}{\partial x_j \partial x_j} + a_i \tag{4.2}$$

Considering small velocity of the upper plate, and thus the Reynolds number as small, the flow can be assumed as laminar. As a result, the viscous term significantly dominates the convective term, so that the convective term is negligible. Thus, the equation (Equation 4.2) results in the form (Equation 4.3).

$$0 = -\frac{1}{\rho} \cdot \frac{\partial p}{\partial x_i} + \nu \cdot \frac{\partial^2 v_i}{\partial x_j \partial x_j} + a_i \tag{4.3}$$

Considering small gap between the plates, and thus small volume of the grease between them, the gravitational forces can be neglected. The equation then takes form (Equation 4.4).

$$0 = -\frac{1}{\rho} \cdot \frac{\partial p}{\partial x_i} + \nu \cdot \frac{\partial^2 v_i}{\partial x_j \partial x_j} \tag{4.4}$$

The equation can be further modified by multiplying with the fluid density (Equation 4.5).

$$0 = -\frac{\partial p}{\partial x_i} + \mu \cdot \frac{\partial^2 v_i}{\partial x_j \cdot \partial x_j} \tag{4.5}$$

Where: μ $(Pa \cdot s)$ is the dynamic viscosity

The pressure can be assumed as constant, thus the equation takes form of (Equation 4.6).

$$0 = \mu \cdot \frac{\partial^2 v_i}{\partial x_j \cdot \partial x_j} \tag{4.6}$$

Then assuming unidirectional flow the equation can be simplified to (Equation 4.7).

$$0 = \mu \cdot \frac{\partial^2 v_1}{\partial x_2 \cdot \partial x_2} \tag{4.7}$$

The velocity profile $v_1(x_2)$ can be calculated by integrating the equation (Equation 4.7) twice with respect to coordinate x_2. The first integration can be mathematically expressed as (Equation 4.8).

$$\int \mu \cdot \frac{\partial^2 v_1}{\partial x_2 \cdot \partial x_2} \cdot dx_2 = \int 0 \cdot dx_2 = A \tag{4.8}$$

Where: A is the constant.

While the second integration can be expressed as (Equation 4.9).

$$\int A \cdot dx_2 = A \cdot x_2 + B \tag{4.9}$$

Where: B is the integration constant.

To find the value of the constants A and B, the boundary conditions can be applied. Where the only boundary condition needed is the no slip condition at both plates. Mathematically expressed as (Equation 4.10) and (Equation 4.11).

$$v(0) = 0 \tag{4.10}$$

$$v(h) = U \tag{4.11}$$

Substituting these conditions into the equation (Equation 4.9), the value of the constants comes out as (Equation 4.12) and (Equation 4.13).

$$B = 0 \tag{4.12}$$

$$A = \frac{U}{h} \tag{4.13}$$

The shear stress at any point in the flow follows the Newtonian viscosity law, mathematically expressed as (Equation 4.14).

$$\tau_{ij} = \mu \cdot \left(\frac{\partial v_i}{\partial x_j} + \frac{\partial v_j}{\partial x_i} \right) \tag{4.14}$$

For the unidirectional flow the equation becomes (Equation 4.15).

$$\tau = \mu \cdot \frac{\partial v_1}{\partial x_2} = \mu \cdot A = \mu \cdot \frac{U}{h} = const. \tag{4.15}$$

Therefore, in this simplified flow scenario, the shear stress remains constant at any given point throughout the fluid. Additionally, even for non-Newtonian fluids, a linear velocity profile would be maintained.

To calculate the frictional force acting upon the moving plate, the equation (Equation 4.15) has to be integrated over the entire surface area of the plate. That can be mathematically expressed as (Equation 4.16).

$$F_{frictional} = \int_A \tau \cdot dA = \int_0^W \int_0^L \tau \cdot dx_1 \cdot dx_3 = \mu \cdot \frac{U}{h} \cdot L \cdot W = \mu \cdot \frac{U}{h} \cdot S \tag{4.16}$$

Where: $F_{frictional}$ (N) represents the frictional force acting upon the moving plate, τ (Pa) is the shear stress in the fluid, S (m^2) is the area of the moving plate, W (m) is the width of the moving plate, L (m) represents the length of the plate, μ $(m^2 \cdot s^{-1})$ is the dynamic viscosity of the fluid between the plates, U $(m \cdot s^{-1})$ is the speed of the moving plate in the x_1 direction and h (m) is the gap between the parallel plates.

For non-Newtonian fluids, the viscosity is shear rate dependent and therefore the viscosity has to be replaced by apparent viscosity, The equation then takes the shape (Equation 4.17)

$$F_{frictional} = \mu(\dot{\gamma}) \cdot \frac{U}{h} \cdot S \tag{4.17}$$

Where: $F_{frictional}$ (N) represents the frictional force acting upon the moving plate, S (m^2) is the area of the moving plate, μ $(m^2 \cdot s^{-1})$ is the dynamic viscosity of the fluid between the plates that is function of shear rate $\dot{\gamma}$ (s^{-1}), U $(m \cdot s^{-1})$ is the speed of the moving plate in the x_1 direction and h (m) is the gap between the parallel plates.

This equation (Equation 4.16), despite the assumptions made during its derivation, offers valuable insights into how the frictional force varies with changes in dynamic viscosity, relative velocity, gap height, and moving plate area. These insights were instrumental in preparing for the experiment.

The experiment involved three different gap sizes. The relative speed of the moving plate was also varied across three levels. Additionally, the moving plate used in the experiment had three different areas. Due to these variations, the experiment can capture the behavior more precisely and the correct material model can be selected.

4.2 Experimental setup

The experimental setup involved tribometer Bruker UMT Tribolab equipped with 2-axis force sensors, 3 types of upper steel plate, reciprocal module with one sliding steel plate and the grease itself. To evaluate the influence of surface roughness the optic profilometer Contour GT-X Bruker was used.

4.2.1 UMT Bruker TriboLab

The tribometer UMT Bruker TriboLab (Figure 4.2) serves as a versatile tool for measuring and characterizing various tribological processes, including wear, the impact of lubricants on friction surfaces, micro-hardness, and adhesion. It offers the capability to simulate diverse tribological conditions such as high temperatures and loads. [54][55] The tribometer is located in the tribological laboratory at the Institute of Machine and Industrial Design at Brno University of Technology.
The movement of the sample was accomplished using reciprocal module shown in figure (Figure 4.3) which ensures linear oscillatory motion. The position of the reciprocal module is tracked using a linear variable differential transformer (LVDT) sensor with a resolution of 1 μm. [56]

Figure 4.2. Tribometer UMT Bruker TriboLab [54]

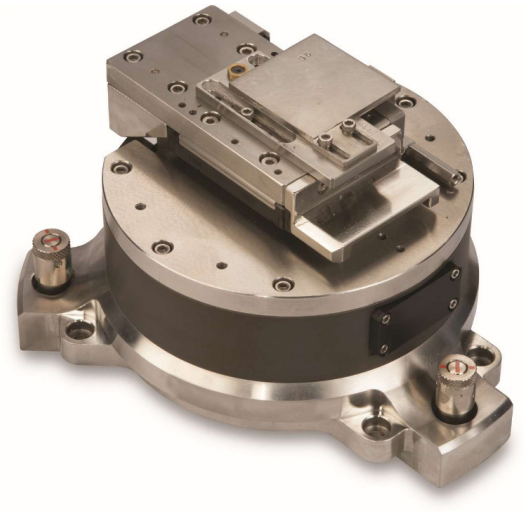

Figure 4.3. Reciprocal drive [54]

The upper changeable module (Figure 4.4) is equipped with DFM-5-G 2-axis force sensor featuring a range spanning from 0.5 N to 50 N and a resolution of 2.5 mN. [56] The noise level is maintained at 0.02 % of the full scale value. [56]

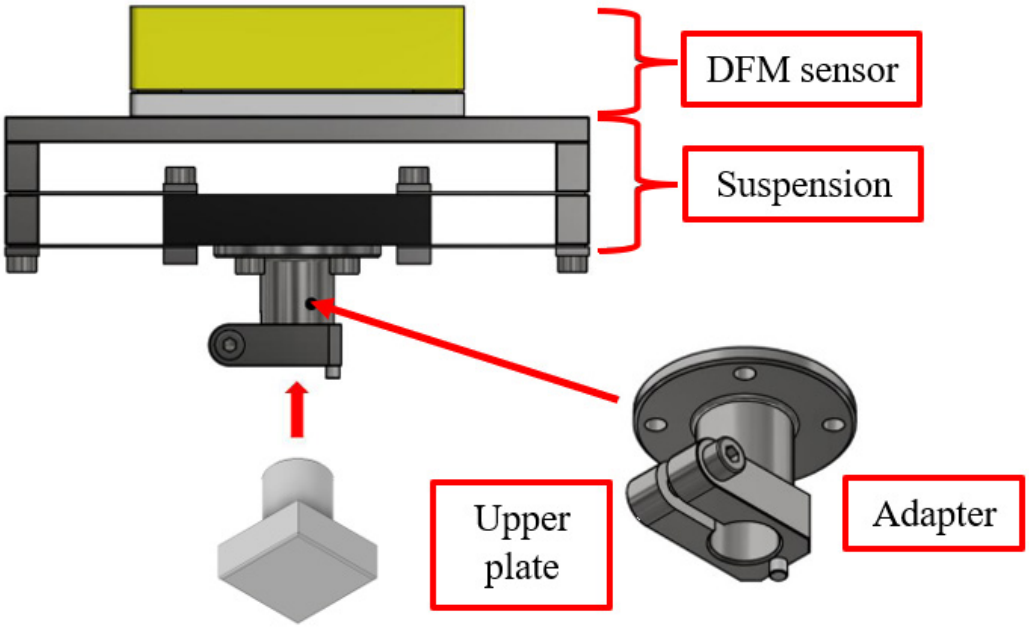

Figure 4.4. Upper changeable module of UMT Bruker TriboLab. (adapted from: [57])

4.2.2 Upper plates

Three upper plates were designed. To maximize the measured force, the largest plate was designed to the largest possible dimensions. The other two plates were designed to be half and quarter the area of the largest plate. The production drawings for all the plates are listed in the appendixes: large plate (Appendix E), medium plate (Appendix F) and small plate (Appendix G).
Visually the plates are shown in figure (Figure 4.5).

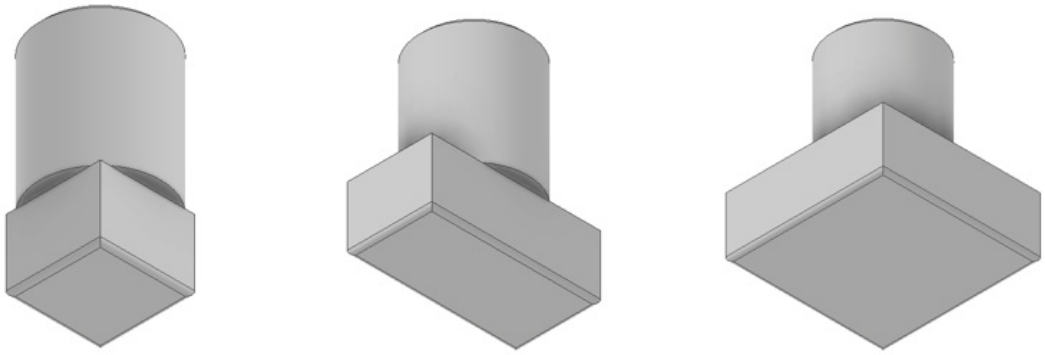

Figure 4.5. Upper plates: on the left the small plate (dimensions 10 mm x 10 mm), in the middle the medium plate (dimensions 20 mm x 10 mm) and on the right the large plate (dimensions 20 mm x 20 mm).

To ensure the best possible parallelism of the top and bottom plates, a geometric tolerance of axial runout was prescribed for the underside of the top plates. Given the method of manufacture - turning and milling, this option is the most suitable. Furthermore, a surface roughness of Ra 0.4 was prescribed on the bottom surface that will be in contact with the grease to ensure the closest possible similarity to the future simulations, that assume absolutely smooth surface.

4.2.3 Bruker Contour GT-X8

The Bruker Contour GT-X8 optic profilometer (Figure 4.6) is designed for non-contact surface topology measurement, operating on the principle of scanning interferometry.[58] It offers versatile applications, including determining the 3D topography of machine part surfaces, delivering high vertical resolution across a broad field of view, and facilitating automated measurements for metrology and quality control purposes. [55] The profilometer is located in the tribological laboratory at the Institute of Machine and Industrial Design at Brno University of Technology.

Figure 4.6. Optic profilometer Bruker Contour GT-X8. [58]

4.3 Measurement procedure

Clamping the tools. The upper plate is secured within the upper exchangeable module of the tribometer using a cylindrical pin, highlighted in red in figure (Figure 4.7). The bottom movable plate is clamped into the reciprocal module using two screws positioned diagonally opposite each other in the module´s corners, as illustrated in figure (Figure 4.7).During the clamping process, it´s crucial to ensure that the side edge of the upper plate remains parallel to the direction of movement.

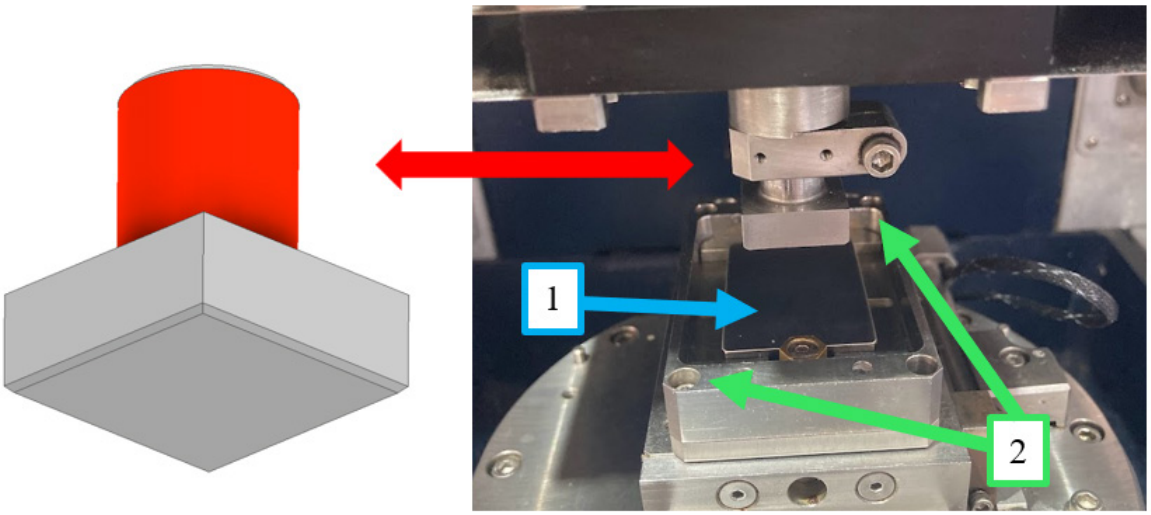

Figure 4.7. Clamping of the upper plate (red), bottom plate (1) and screws (2).

Zero setting. It is necessary to set the zero point of the vertical axis, i.e. the point where the upper and lower plates are in contact.

Application of grease. The grease is applied approximately in the middle of the bottom plate.

Heating. The grease is heated using heating cartridges, with temperature monitored by a heat sensor. These cartridges are inserted into designated holes in the module beneath the bottom plate. Heat is then transferred through the module and bottom plate to reach the grease. The whole setup is shown in figure (Figure 4.8).

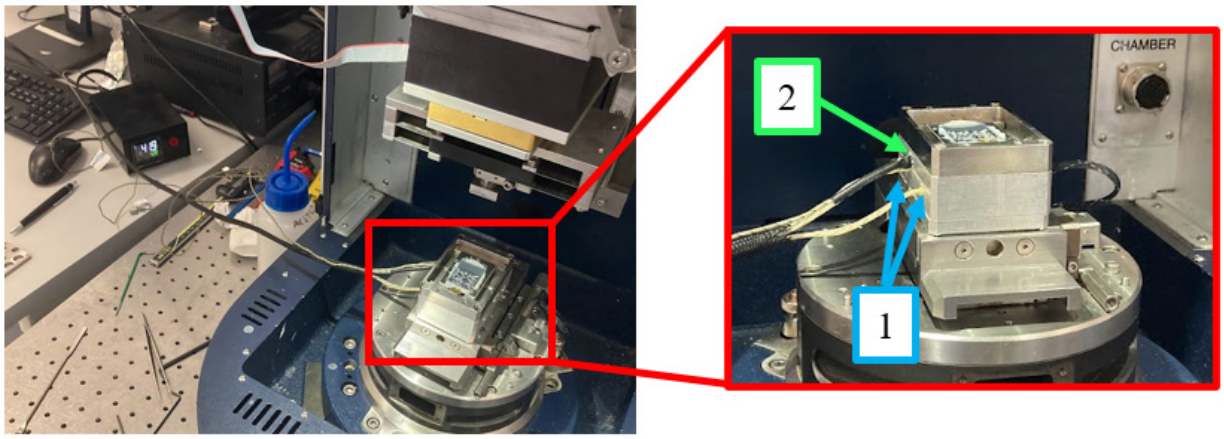

Figure 4.8. Heating of the grease using heating cartridges (1) and a heat sensor (2).

Grease smearing. The grease should be spread to ensure a continuous layer over the entire moving plate area. This is achieved by positioning the upper plate 0.5 mm above the bottom plate and then moving the bottom plate with an amplitude of 15 mm (5 mm beyond the measurement) at a frequency of 1 Hz. This action effectively smears the grease. Once the measurement is taken at a specific gap, such as 0.2 mm, the smearing process is repeated at that gap as well to ensure consistent application.

Measurement. To initiate measurement, the upper plate is positioned at the specified height and the grease is uniformly smeared. Subsequently, the frequency of the reciprocal drive is adjusted to the desired value, and the measurement process is commenced. Throughout the measurement, the forces in both vertical and directional movements are monitored and recorded along with the corresponding positions obtained from the LVDT sensor.

4.4 Measurement uncertainty

The uncertainty of measurement can be introduced by several factors.

Sensor resolution. This refers to the smallest change in the input quantity that can be detected by the sensor. It represents the smallest division or increment of the sensor´s output scale. The manufacturer states that the resolution of sensor is set at 2.5 mN. [56]

$$u_{resolution} = 0.0025\ N \tag{4.18}$$

Sensor non-linearity and hysteresis. Non-linearity refers to the maximum deviation of a measured value from a specified straight line that connects the maximum value and minimum value possible to measure. Hysteresis arises when the sensor´s output not only depends on the current input but also on its previous input history. This phenomenon is particularly pronounced in cyclically applied forces or strains, as is the case in this experiment, and can contribute to non-linear behavior. The exact value was measured directly on used sensor DFM-5-G. It is important to note that this value is valid within the sensor range and values below this range may vary.

$$u_{hysteresis} = 0.0149\ N \tag{4.19}$$

Sensor noise. Noise refers to a random variations or fluctuations in the sensor output that are not related to the measured quantity. This can be due to electronic interference, thermal fluctuations, or other environmental factors. The manufacturer states that the value of sensor noise is 0.02 % of full scale values. [56] In addition to the causes already mentioned, vibrations from the surroundings can be added. To get more precise values, the measurement was done. This included ”idle” measurements, i.e. measurements when no part of the machine was moving (Figure 4.9). From the chart it can be seen that the average value of noise during the measurement is approximately 0.007 N.

$$u_{noise} = 0.007\ N \tag{4.20}$$

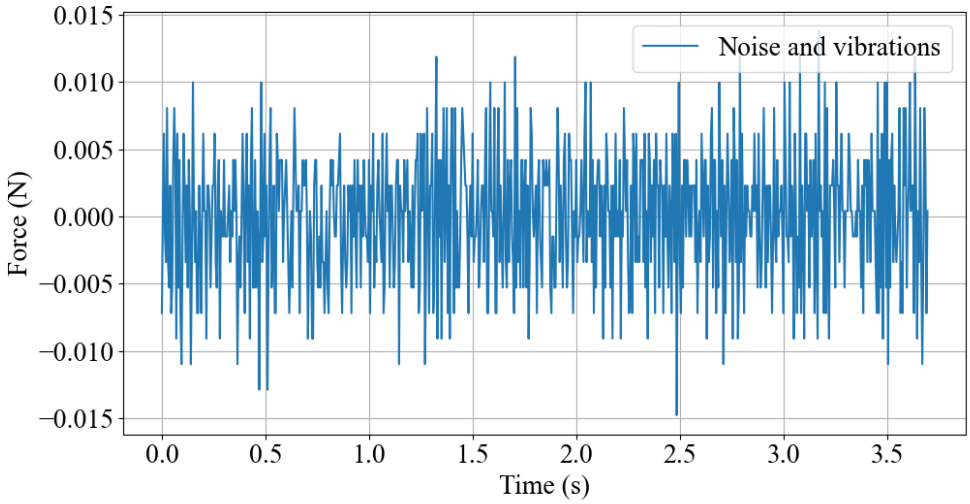

Figure 4.9. Noise of sensor output caused by surroundings vibrations and sensor noise itself.

Sensor accuracy. Considering the sensor range specified by the manufacturer is 0.5 N to 50 N and the values of measured force are in the range of 0.1 N to 1.5 N the sensor accuracy may vary from values specified by manufacturer. Therefore the measurement was done to evaluate the sensor accuracy.
The principle of the first measurement is to monitor the force generated by placing a body of precise weight on the sensor. This was achieved by placing screws one by one on the sensor as it is shown in figure (Figure 4.10).

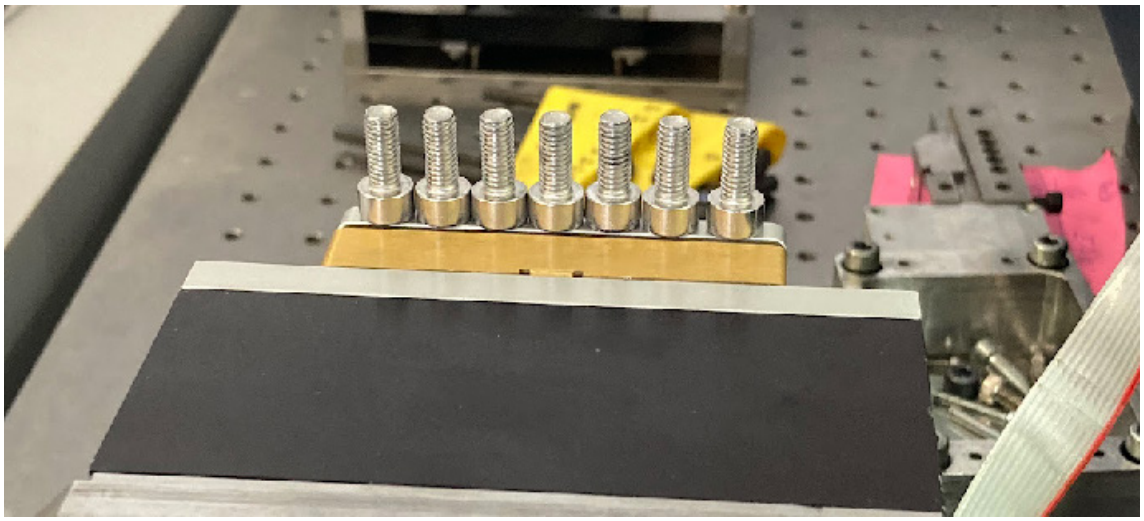

Figure 4.10. Screws placed on the sensor, which is positioned on its side.

Considering the precise weight of the screws is known, the gravitational force can be calculated using formula (Equation 4.21).

$$F_g = m \cdot g \tag{4.21}$$

Where: F_g (N) is the gravitational force, m (kg) represents the weight of the screw and the g ($m \cdot s^{-2}$) is the gravitational acceleration.

The calculated force was then compared with the measured force, and the slope of the linear regression between these two data sets was determined (Figure 4.11).

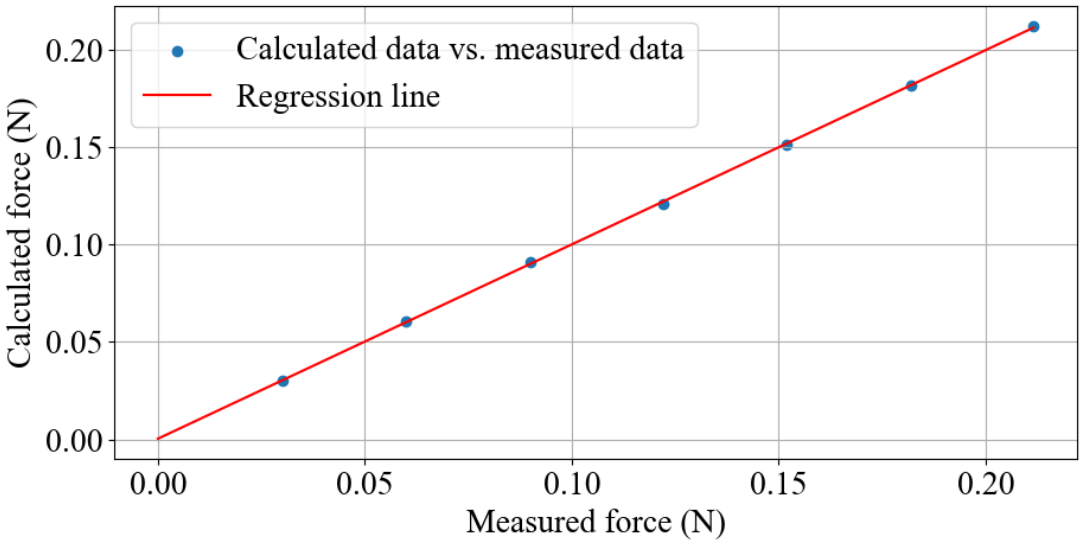

Figure 4.11. Calculated gravitational force generated by screws vs. measured force generated by screws.

The found slope is $k_{screws} = 1.0035$, which means that the sensor is behaving almost perfectly linearly. Unfortunately, the weight of the sensor itself generate considerable force - to be precise 1.1915 N. This force shifts the measurement area into the sensor range and therefore this method of measurement is not suitable for the purpose of determining the accuracy of the sensor in areas of near-zero values.

Therefore, a second method is proposed, which allows the sensor to be positioned upside down. This method measures the magnitude of force exerted on the sensor by objects leaning against it. The objects were selected to have a constant cross-section and sufficient length to rest on the corner of the sensor. Additionally, the mass of these objects was accurately measured. The measurement setup is shown in figure (Figure 4.12).

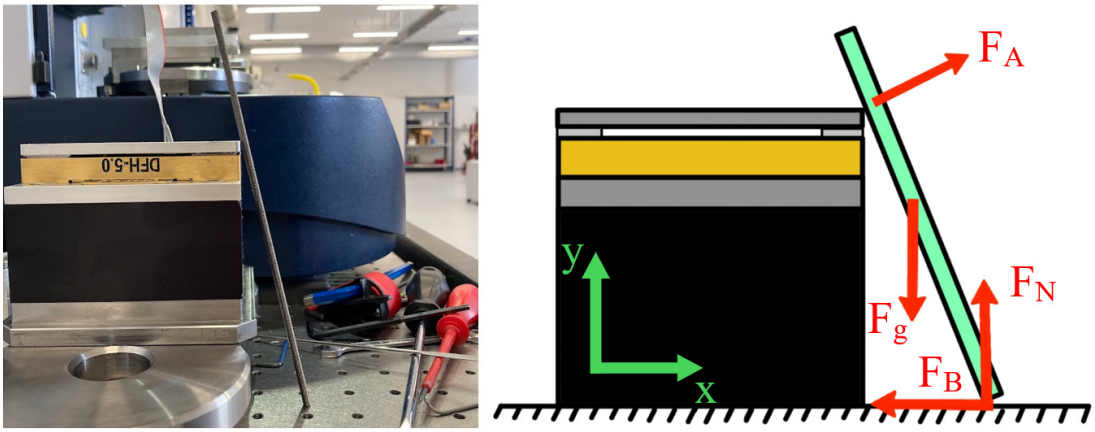

Figure 4.12. The second method of force measurement near zero-values, photo of measurement on the left and free-body diagram on the right.

The gravitational force F_g acts on the object at its center of gravity, while the force F_A is exerted by the sensor perpendicular to the object. The floor exerts a normal force F_N on the object. The frictional force between the floor and the object is denoted as F_B. The friction between the sensor and the object is neglected.
Given that the forces acting on the rod maintain its equilibrium, the resultant force on the object and the resultant moment of force has to be zero. That can be mathematically expressed as (Equation 4.22) (Equation 4.23).

$$\vec{F_A} + \vec{F_g} + \vec{F_B} + \vec{F_N} = 0 \tag{4.22}$$

$$\vec{M_A} + \vec{M_g} + \vec{M_B} + \vec{M_N} = 0 \tag{4.23}$$

By solving these equations, the force of interest can be calculated, according to equation (Equation 4.24).

$$F_{Ax} = F_B = m \cdot g \cdot \frac{L}{H} \cdot \frac{sin(2 \cdot \alpha) \cdot cos(\alpha)}{4} \tag{4.24}$$

Where: F_{Ax} (N) represents the force acting on the sensor from the leaning object, m (kg) is the weight of the object, g ($m \cdot s^{-2}$) is the gravitational acceleration, L (m) represents the length of the object, H (m) is the height of the point where the object and the sensor are in the contact and α (°) represents the angle between the sensor and the object

The calculated force was then compared with measured force and the slope of linear regression between these sets of data was determined (Figure 4.13).

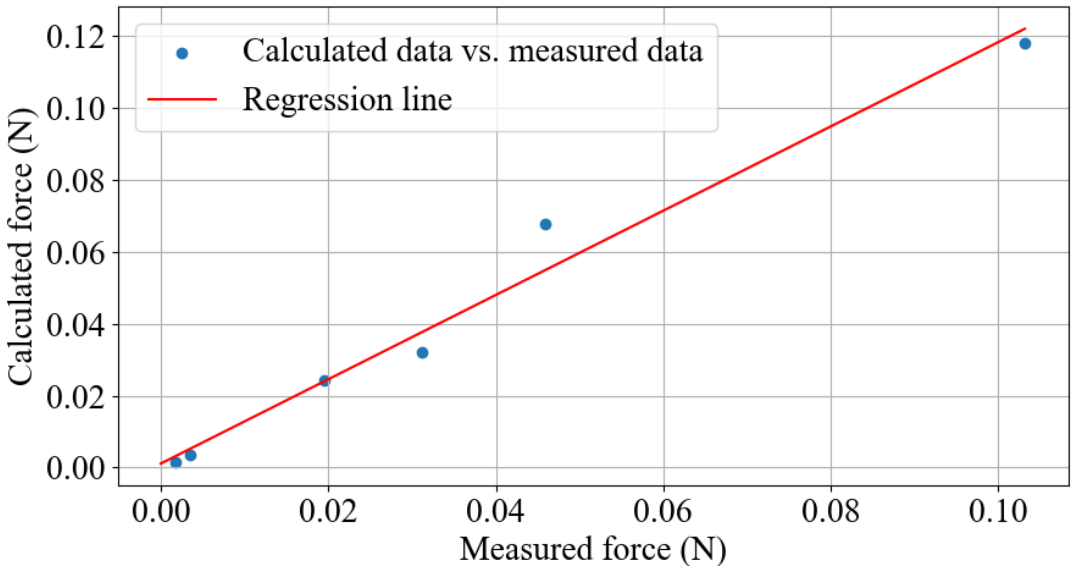

Figure 4.13. Calculated force acting on the sensor from leaning object vs. measured force generated by leaning object.

The value of found slope is $k_{LeaningObjects} = 0.8581$. The value less than 1 suggest that the sensor response is slightly lower than expected for a given input force. While the sensitivity is slightly lower than ideal, it´s still relatively close to 1, indicating that the sensor is responsive to changes in force, and therefore can be used for measurement.

The next step is calculating the standard deviation of residuals of the measurement according to formula (Equation 4.25).

$$\sigma = \sqrt{\frac{\sum_{i=1}^{n}(x_i - \bar{x})^2}{n}} = 0.00912N \tag{4.25}$$

Where: σ (N) denotes the standard deviation, x_i (N) represents the each individual measurement, $\bar{x}$ (N) is the mean of all measurements and n (-) is the total number of measurements.

The value of standard deviation can be assumed as the uncertainty of the measurement in the area of near-zero values. Mathematically expressed as (Equation 4.26).

$$u_{accuracy} = 0.00912\ N \tag{4.26}$$

To evaluate measurement the method called root sum square (RSS) will be used. This method is applicable when the sources of uncertainty are independent or can be treated as independent. [59]
In the case of experiment, the uncertainties can be assumed as independent. The measured value, in this case force on plate, is directly used for further evaluation, and is not used to calculate further entities.
The RSS method is based on the principle that when combining uncertainties from different sources, the combined uncertainty is the square root of the sum of squares of individual uncertainties. That can be mathematically expressed as (Equation 4.27).

$$U = \sqrt{u_1^2 + u_2^2 + ... + u_n^2} = \sqrt{\sum_{i=1}^{n} {u_i}^2} \tag{4.27}$$

Where: U (-) is the combined uncertainty, u_i (-) is individual uncertainty and n (-) is the total number of uncertainties.

By substituting the observed values the equation (Equation 4.28) is obtained.

$$\begin{aligned} U_{\text{force}} &= \sqrt{\sum_{i=1}^{n} {u_i}^2} = \\ &= \sqrt{u_{\text{resolution}}^2 + u_{\text{hysteresis}}^2 + u_{\text{noise}}^2 + u_{\text{accuracy}}^2} = \\ &= \sqrt{0.0025^2 + 0.0149^2 + 0.007^2 + 0.00912^2} = \\ &= 0.01899\,\text{N} \end{aligned} \tag{4.28}$$

The magnitude of measurement uncertainty is not significantly high compared to the measured values. However, it can be concluded that when the measured value is near zero, the results may vary considerably. For a measured force of 0.1 N, the uncertainty is almost 20 %, which is relatively high. Therefore, primarily measurements with force magnitudes higher than 0.5 N will be evaluated.

4.5 Results

The table (Table 4.1) presents a comprehensive list of all experiments conducted. These experiments encompassed three distinct gap sizes, three levels of relative speed for the moving plate, and utilized moving plates with three different areas, as explained in section (Section 4.1). Additionally, the upper plate, measuring 20 mm x 10 mm, can be moved in two orientations: with the smaller edge (10 mm) perpendicular to the direction of movement or with the larger edge (20 mm) perpendicular to the direction of movement. In the table, the "Plate dimension" column includes entries such as "20 x 10 both," indicating that the test was conducted for both setups.

All of the results are shown in the appendix (Appendix H). All of the results are normalized on y-axis to ensure the confidentiality of the given force magnitude. Normalization of the results is achieved by dividing all measurements by the same value - the maximum measured force value.

For good clarity of the visualised data, only some results will be shown in this section. For same reason only measured data will be shown without the measurement uncertainty involved.

The results (Figure 4.14) show the influence of frequency of the movement, thus the influence of speed of the moving plate. The results in figure (Figure 4.14) are shown only for tests done with upper plate with dimensions 20 mm x 20 mm at 0.1 mm gap thickness for good clarity.

Table 4.1: List of experiments done at UMT Bruker TriboLab.

Frequency	Gap thickness	Plate dimensions	Temperature
Hz	mm	mm	°C
0.25	0.05	20 x 20, 20 x 10 both, 10 x 10	20, 40
0.5	0.05	20 x 20, 20 x 10 both, 10 x 10	20, 40
0.5	0.1	20 x 20, 20 x 10 both, 10 x 10	20, 40
1	0.05	20 x 20, 20 x 10 both, 10 x 10	20, 40
1	0.1	20 x 20, 20 x 10 both, 10 x 10	20, 40
1	0.2	20 x 20, 20 x 10 both, 10 x 10	20, 40
2	0.1	20 x 20, 20 x 10 both, 10 x 10	20, 40
2	0.2	20 x 20, 20 x 10 both, 10 x 10	20, 40
4	0.2	20 x 20, 20 x 10 both, 10 x 10	20, 40

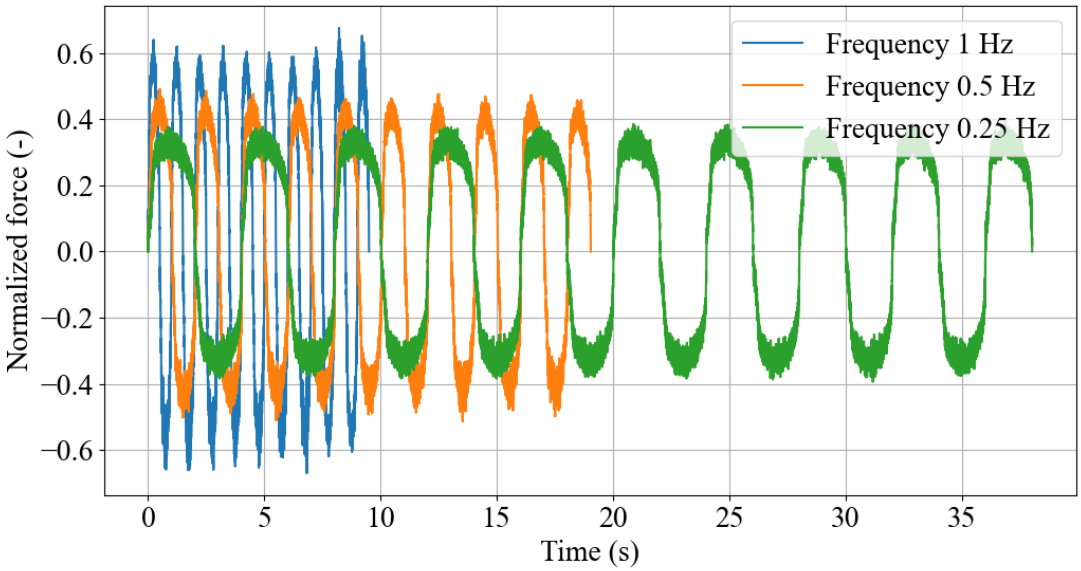

Figure 4.14. Results of the measurement at temperature 20 °C, with upper plate with dimensions 20 mm x 20 mm at 0.1 mm gap thickness for 3 different frequencies. The results are normalized on y-axis.

It can be concluded that with a higher frequency of the moving plate, the amplitude of the measured force increases. This conclusion holds true across almost all measurements conducted. Additionally, it´s observed that the force neither rises nor declines over time for each test, indicating that the force measured on the upper plate remains stable throughout.

In figure (Figure 4.15) the influence of the temperature of the grease is visualised.

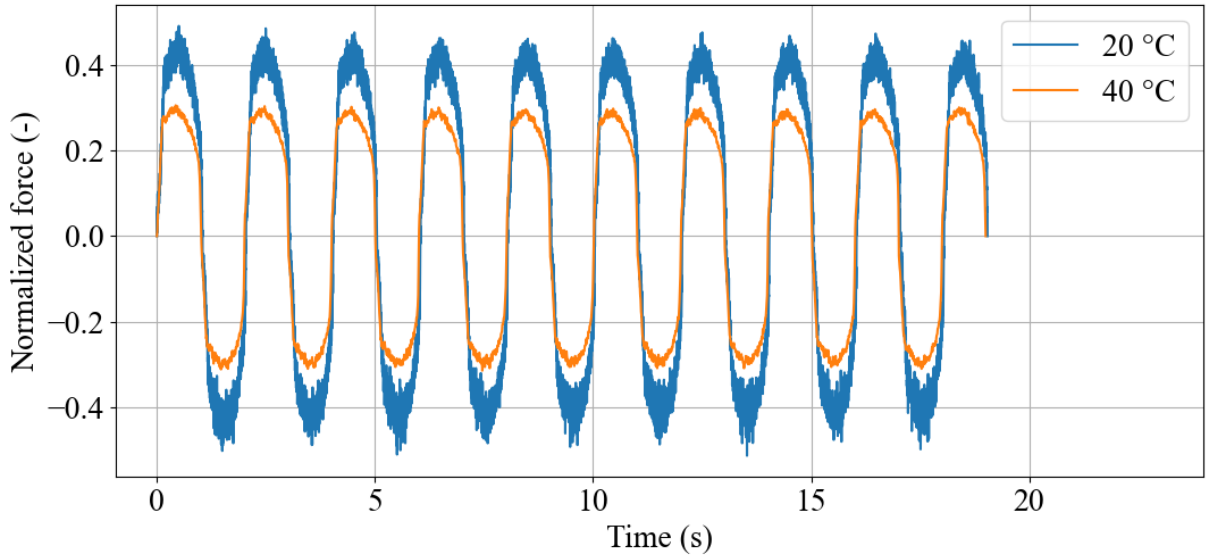

Figure 4.15. Comparison of the same measurement (with upper plate with dimensions 20 mm x 20 mm at 0.1 mm gap thickness at movement frequency 0.5 Hz) at 2 different temperatures: 20 °C and 40 °C. The results are normalized on y-axis.

It is evident that the force amplitude decreases with higher temperatures, aligning with expectations. Specifically, the dynamic viscosity at 40°C is lower than that at 20°C, while the remaining measurement quantities remain constant. Consequently, the force is expected to decrease accordingly across all measurements.

The experiments were done with three different types of upper plates, while the middle plate can be moved in two directions as already explained above (Section 4.5). The influence of the type of plate is shown in figure (Figure 4.16).

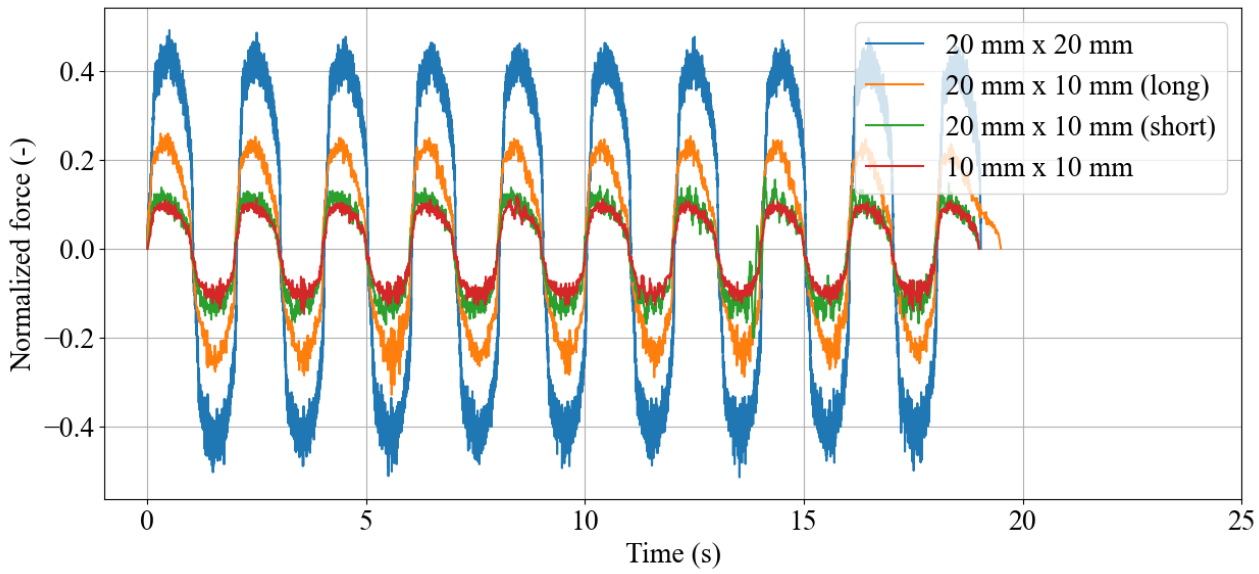

Figure 4.16. Influence of the upper plate dimensions on the force magnitude. The results are shown for test at gap thickness 0.1 mm, frequency 0.5 Hz and temperature 20 °C. The results are normalized on y-axis.

It can be concluded that with smaller are of the upper plate, the force magnitude is decreasing as expected. The magnitude of force on the plate with dimensions 20 mm x 10 mm (short - where the short edge is perpendicular to the direction of moving) is smaller than than the force on the plate 20 mm x 10 mm (long). That can indicate that the grease shearing is not the only source of the force generated on the moving plate. That is confirmed by the results with the smallest plate, even tho the area is half the size of the medium plate, the force on the plate in not half of the force magnitude, but is just slightly smaller. A likely other source of force is the rolling of grease in front of the upper plate. Another reason could be the measurement uncertainty, which can influence the results up to 20 % for the smallest plate and the middle plate with short side perpendicular to the movement direction.

The measurement of the force acting upon upper plate can be influenced by the surface roughness of both upper and bottom plate. This was tested in the experimental research by changing the surface roughness of the upper plate. The figure (Figure 4.17) shows the three structures of the surface used for measurement. The surface roughness of the bottom plate is constant at Ra 0.4.

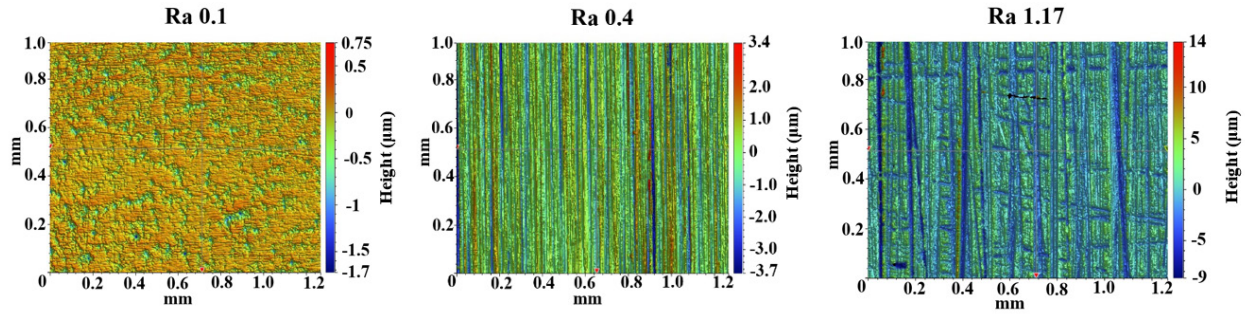

Figure 4.17. Three different surface roughness of the upper plate measured on the optic profilometer Bruker Contour GT-X8.

The results of the measurement are shown in figure (Figure 4.18).

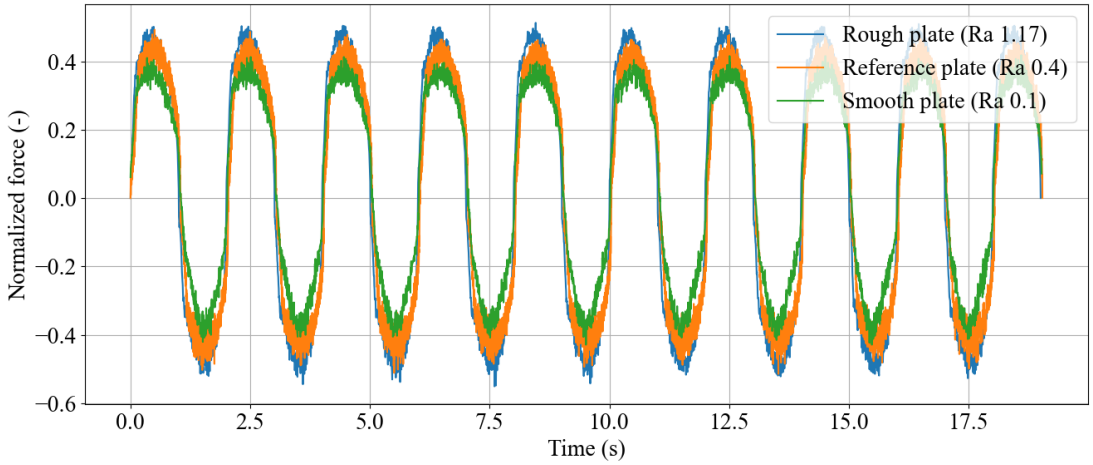

Figure 4.18. Results of test done at temperature 20 °C at frequency 0.5 Hz with upper plate with dimensions 20 mm x 20 mm with 3 different surface roughness. The results are normalized on y-axis.

It can be concluded, that there is slight influence of surface roughness. With smoother upper plate, the force magnitude declines. The difference between the reference plate (Ra 0.4) and smooth plate (Ra 0.1) is approximately 12 %. This fact negatively affects the results and should be can further influence the force magnitude when compared to the simulation results.

5 CFD simulations

The initial simulations aim to identify the optimal material model among those outlined in chapter (Chapter 3). Subsequently, simulations based on the experimental investigation outlined in chapter (Chapter 4) are conducted initially in 2-D, followed by a single calculation in 3-D. These simulations outcomes serve as a basis for further modeling the flow of grease within an actual ball joint, utilizing the geometry obtained in chapter (Chapter 2).

5.1 2-D simulation

As mentioned, these simulations aim to find the optimal material model. Thus, the geometry corresponds to the experimental setup - bottom plate, upper plate and grease between them. The geometry is shown in figure (Figure 5.1).

Figure 5.1. Geometry of the 2-D simulation.

5.1.1 Viscous model

To determine whether the flow is laminar, the Reynolds number can be used. Because the simulations can be simplified to two plates sliding against each other, the best approach is to use formula for plane Couette flow. The paper [60] states that the Reynolds number for plane Couette flow can be calculated according to the conventional formula (Equation 5.1).

$$Re = \frac{\rho \cdot U \cdot h}{\mu} \tag{5.1}$$

Where: Re (-) is the Reynolds number, ρ $(kg \cdot m^{-3})$ represents the fluid density, U $(m \cdot s^{-1})$ is the speed of the moving plate, μ $(Pa \cdot s)$ is the dynamic viscosity of the fluid and the h (m) is the gap between the plates.

Calculating the Reynolds number for non-Newtonian fluids is more intricate compared to Newtonian fluids due to the viscosity´s dependence on factors like the velocity of the upper plate and the gap thickness. In the case of pseudoplastic fluids, as the viscosity decreases with higher shear rates, the Reynolds number increases with rising velocity for constant gap thickness. Assuming constant density and velocity, the Reynolds number becomes solely a function of the gap thickness. This relationship is depicted in figure (Figure 5.2).

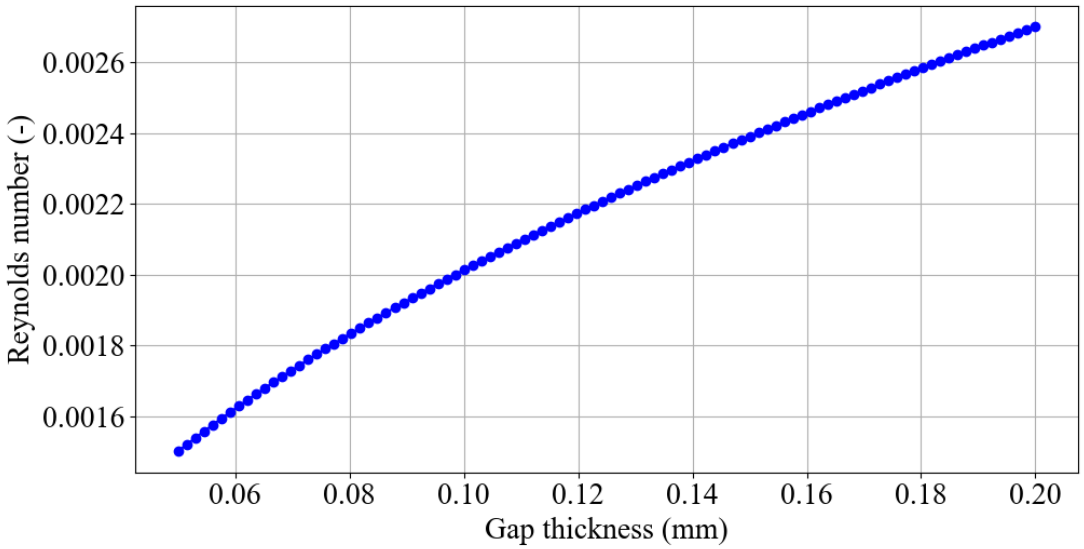

Figure 5.2. Dependency of Reynolds number on the gap thickness for constant density and velocity (velocity corresponds to a frequency 4 Hz of moving plate).

The experimental study was carried out earlier by J. Leutheusser and H. Chu [61]. The results showed that the critical Reynolds number for Couette flow lies within values 280 to 750. Further experimental studies using flow visualization done by Daviuad et al [62] and Tillmark and Alfredsson [63] are in the agreement that the critical Reynolds number lies within 370 ± 10. This number was confirmed even by numerical study carried out by Lundbladh and Johansson [64].

It can be easily concluded that because the Reynolds number calculated is much smaller than critical Reynolds number, and thus the flow, and viscous model, can be assumed as laminar.

5.1.2 Multiphase model

To simulate the multi phase behavior, the Volume of fluid (VOF) with explicit formulation was selected. This model and formulation is particularly useful for problems involving free surface flow, which is the case of this calculation. The phases are defined as follows: grease is the primary phase, and air is the secondary phase. The interaction between them is modelled using constant surface tension coefficient. Considering the exact value of surface tension for the grease used in this simulation is not known, the value of base oil only will be used. The paper by R. Mozes et al. [65] states that the surface tension coefficient is approximately $\sigma = 0.031\, N \cdot m^{-1}$ and contact angle for base oil of lubricants is approximately $\theta = 30\,°$. The surface tension and even the contact angle are highly affected by additives added to the base oil, so the values are only indicative. [66]

To capture the effects of grease near the moving wall, the surface tension force modelling is enabled with continuum surface force and wall adhesion setting.

5.1.3 Boundary conditions

The boundary conditions are shown in figure (Figure 5.4). The whole domain is divided into four fluid domains. The Fluid (middle) domain is moving from left to right using User Defined Function shown in figure (Figure 5.3). The values of the constants A and B are found by fitting the velocity magnitude record of the reciprocal module from the measurement for each simulation.

```
#include "udf.h"
#include "dynamesh_tools.h"
#define DEBUG 0

DEFINE_CG_MOTION(moving_wall,dt,vel,omega,time,dtime)
{
    real A = 1;
    real B = 1;
    NV_S (vel, = , 0.0);
    vel[0] = A*cos(B*time);
}
```

Figure 5.3. User Defined Function for 2-D simulation.

The fluid domains at the sides - Fluid (left) and Fluid (right), are re-meshing using Dynamic mesh with method Layering. The pressure outlets - shown as blue in the figure (Figure 5.4) are set to Gauge pressure = 0 Pa. The walls are set to stationary, with no-slip conditions and contact angle set to $\theta = 30\,^{\circ}$ as explained in the subsection (Subsection 5.1.2).

Among the reference values, depth and area are particularly important. The depth is set according to the dimensions of the upper plate - for 20 mm x 20 mm the depth is set to 20 mm, and likewise for the rest. Similarly, the area is derived from the upper plate´s dimensions - for 20 mm x 20 mm the area is established as 400 mm^2

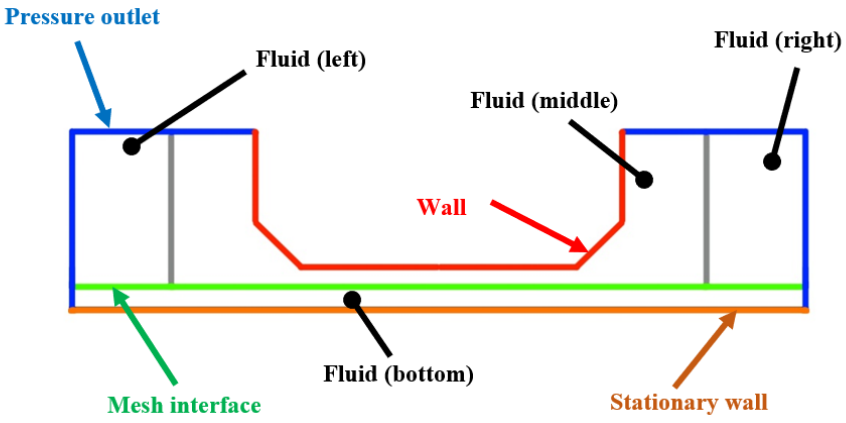

Figure 5.4. Boundary conditions of the 2-D geometry (the figure is not to scale for better clarity).

5.1.4 Mesh

The software Ansys Meshing was used to mesh the geometry. In the domains Fluid (left), Fluid (right) and Fluid (bottom) is structured quadrilateral mesh. In the Fluid (middle) domain it is not possible to create decomposition that would allow a quadrilateral mesh over the entire area, due to incompatibility with Dynamic mesh methods. The mesh is shown in figure (Figure 5.5).

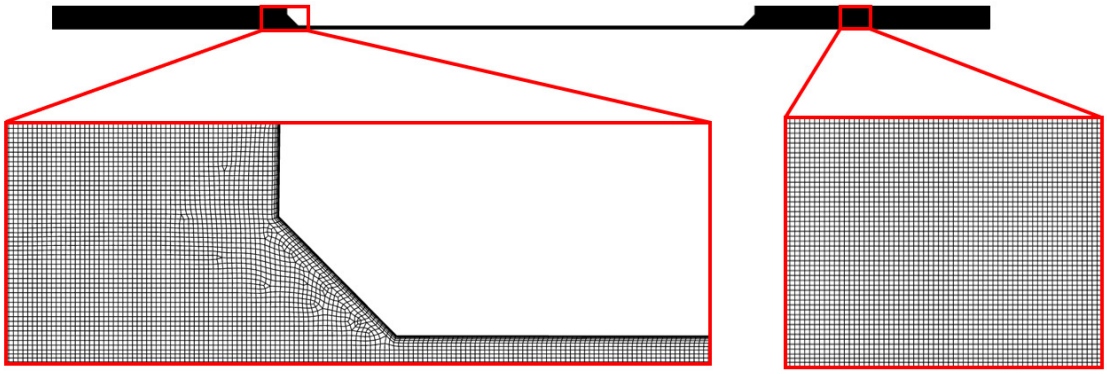

Figure 5.5. The whole mesh of the 2-D geometry and 2 details of important places - The area near wall, and the plate where the re-meshing is happening.

The mesh comprises 61 656 cells and 65739 nodes. The quality of the mesh is depicted in the table (Table 5.1).

Table 5.1: Mesh quality of the 2-D geometry.

Metrics	Minimum	Average	Maximum
Element quality	0.16146	0.9267	0.99947
Aspect ratio	1	1.53	11.263
Skewness	1.3057e-10	1.8593e-2	0.76802

To ensure the movement of domain, the dynamic mesh method Layering is selected. This method split or merge quadrilateral cells (in case of 2-D calculation) with the adjacent cell layer. The Split factor and Collapse factor are used to select if the cell will be merged or split. For purpose of this calculation the method is set as height based. In this approach, each cell is divided into two layers: one with a fixed height denoted as h_{ideal}, and the other with the remaining height represented as $h - h_{\text{ideal}}$. [67] The Split factor set as $\alpha_s = 0.4$ and Collapse factor is set as $\alpha_c = 0.2$.

5.1.5 Solution setting

All the settings of the solution methods are listed in the table (Table 5.2). Additionally, the solver is set to Double Precision.

Table 5.2: Solution methods used for calculation of 2-D geometry.

	Setting
Scheme	SIMPLE
Gradient	Least square cell based
Pressure	PRESTO!
Momentum	QUICK
Volume fraction	Modified HRIC
Transient formulation	First order implicit

The time step size was determined based on the requirement of the dynamic mesh, which stipulates that the moving domain cannot traverse more than one mesh element within a single time step. This condition can be expressed mathematically as (Equation 5.2).

$$\Delta t = \frac{x}{u} \tag{5.2}$$

Where: Δt (s) is the time step size, x represents the smallest size of the mesh element on the dynamic mesh border and the u ($m \cdot s^{-2}$) is the maximum speed of the moving domain.

The speed of the moving plate is given by equation (Equation 5.3), where the constants A ($m \cdot s^{-1}$) and B ($rad \cdot s^{-1}$) are found by fitting the measured data and are listed in the table (Table 5.3). It is obvious, that maximal velocity is given by the amplitude, i.e. the velocity that is added to the formula (Equation 5.2) is the value of the amplitude. The smallest size of the mesh element on the dynamic mesh border is set at x = 0.00002 m. The time step sizes for each condition are presented in the table (Table 5.3).

$$u = A \cdot cos(B \cdot t) \tag{5.3}$$

Where: u ($m \cdot s^{-1}$) represents the speed of the upper plate, A ($m \cdot s^{-1}$) is the amplitude of the velocity, B (s^{-1}) is the angular frequency and the t (s) denotes the time.

Table 5.3: Solution methods used for calculation of 2-D geometry.

A $(m \cdot s^{-1})$	**B** $(rad \cdot s^{-1})$	**Maximal time step size (s)**	**Time step size used (s)**
0.0041	0.7912	0.005	0.001
0.0082	1.5751	0.00244	0.001
0.0155	3.1425	0.0012903	0.001
0.0302	6.3012	0.000667	0.0006
0.0620	12.6284	0.000323	0.0003
0.1210	25.2458	0.000167	0.00015

5.2 2-D simulation results

The results from each simulation are compared with experimental measurement or another simulation. Considering the time dependence of the force is oscillatory, the evaluation is performed using two methods - Root mean squared error (RMSE) and Mean percentage difference (MPD).

Root mean square error method provides a measure of the standard deviation of the residuals, i.e., the spread of errors. The RMSE method results in the same units as the dependent value, meaning it is easier to interpret. Mathematically, the RMSE method for comparing the magnitude of force between experiment and simulation can be expressed as (Equation 5.4).

$$RMSE = \sqrt{\frac{1}{n}\sum_{i=1}^{n}(y_i - \hat{y}_i)^2} \tag{5.4}$$

Where: n (-) is the number of data points, y_i (N) is the measured experimental data and the $\hat{y}_i$ (N) represents the data obtained from the simulation.

Mean percentage difference measures the average relative difference between the actual and predicted values as a percentage of the actual values. This methods is particularly useful when dealing with datasets with varying scales. Mathematically, the MPD method for comparing the magnitude of force between experiment and simulation can be expressed as (Equation 5.5).

$$MPD = \frac{1}{n}\sum_{i=1}^{n}\left|\frac{y_i - \hat{y}_i}{y_i}\right| \cdot 100 \tag{5.5}$$

Where: n (-) is the number of data points, y_i (N) is the measured experimental data and the $\hat{y}_i$ (N) represents the data obtained from the simulation.

5.2.1 Mesh independence study

The mesh independence study in CFD calculations is conducted to determine the appropriate mesh size required to obtain accurate results without unnecessarily high computational time. [68]

The mesh independence study typically involves:

Step 1. - Initial mesh. Conduct calculations using the initial mesh to establish a baseline for the simulation results.

Step 2. - Mesh refinement. Globally refine the mesh by halving the cell size throughout the entire domain. This step aims to increase the mesh resolution to better capture fine-scale features and gradients within the domain.

Step 3. - Simulation rerun. Re-run the simulation using the refined mesh to obtain a new set of results. Ensure that the simulation settings and boundary conditions remain consistent with those used in the initial simulation to facilitate a direct comparison between the results obtained from different mesh resolutions.

Step 4. - Comparison of Results. Analyze and compare the results obtained from different mesh resolutions to assess the impact of mesh refinement on solution accuracy and convergence behavior.

Step 5. - Optimal mesh determination. Based on the comparison of results, identify the optimal mesh resolution that balances computational cost with solution accuracy.

All the used meshes are shown in the table (Table 5.4). The reference mesh is mesh with elements size 1e-5 m. The root mean square error (RMSE) and mean percentage difference (MPD) are calculated for all the results.

Table 5.4: Size of each mesh used for mesh independence study.

Mesh type -	Cells count (-)	Node count (-)	MPD (%)	RMSE (N)
Mesh - 62k cells	61656	65739	3.4273	0.00479
Mesh - 103k cells	102967	108403	3.0757	0.00419
Reference mesh - 231k cells	231215	239346	-	-
Mesh - 410k cells	409702	420564	3.5666	0.00399

Calculations were attempted using mesh sizes with cell count of 30 000 and 22 000, but encountered a ”floating point exception” error. This likely occurred due to the small number (2 to 4) of elements present in the gap between the plates. The resolution proved insufficient, particularly in front of the moving upper plate, where grease accumulates as a result of rolling and as said between the plates. Therefore, it can be concluded that a computational mesh with a cell count of 62k cells (element size 2e-5 m) is adequate in terms of both solution accuracy and computational efficiency, because the results do not vary across the mesh sizes. The visual representation of mesh independence study is shown in figure (Figure 5.6).

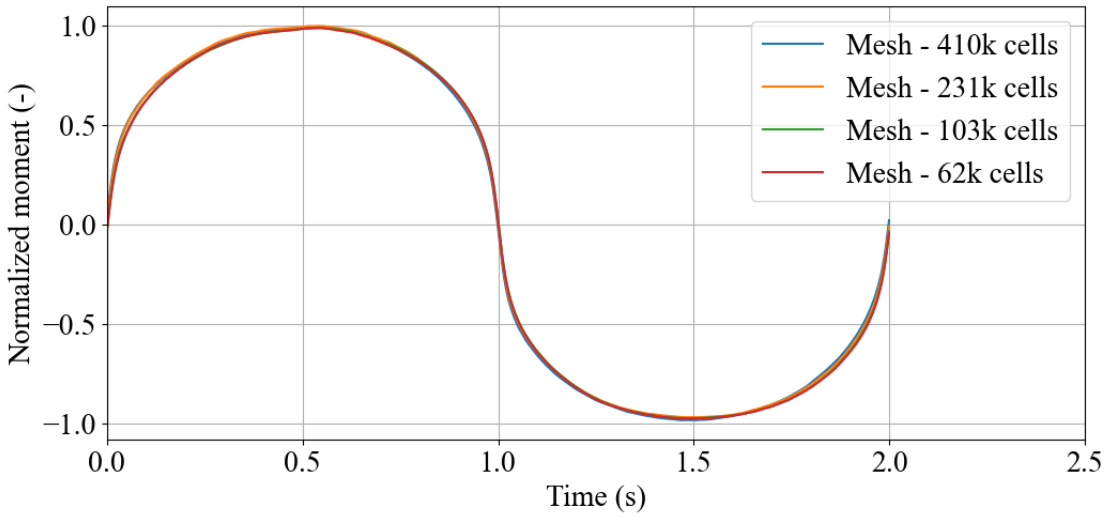

Figure 5.6. The results of calculation with same conditions on different mesh sizes.

5.2.2 Material model selection

The primary objective of this 2-D simulation is to identify the appropriate non-Newtonian material model. This is accomplished by conducting simulations with identical boundary conditions, mesh, and solver settings, but varying the material models — Power-Law, Herschel-Bulkley, Cross, and Carreau fluid model.
In this simulation, a 20 mm x 20 mm upper plate was chosen, with a gap thickness of 0.1 mm and a movement frequency of 0.5 Hz. The results are shown in figure (Figure 5.7) and are listed in the table (Table 5.5).

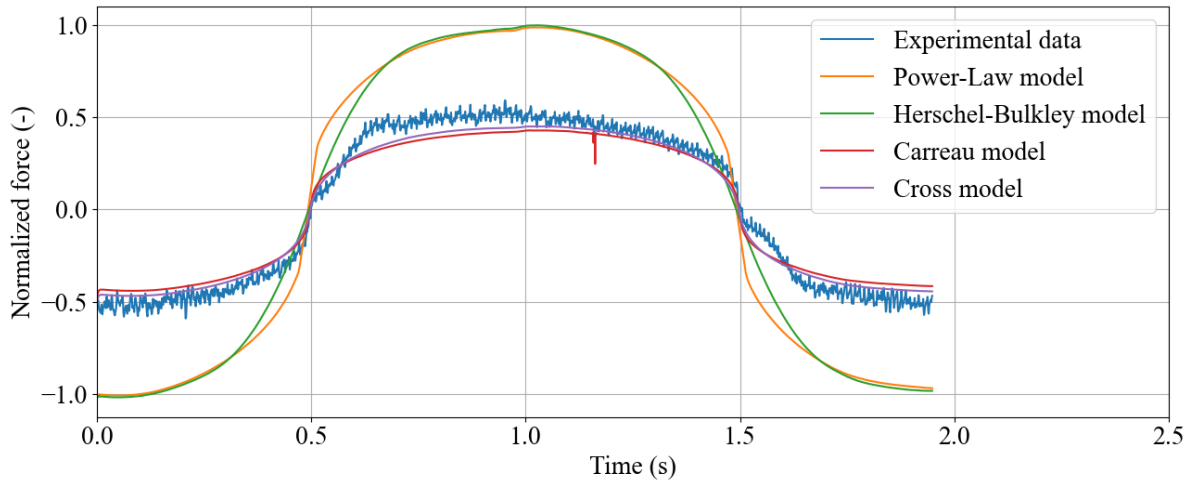

Figure 5.7. The results of calculation with varying non-Newtonian model compared with experimental measurement with conditions: 20 mm x 20 mm upper plate dimensions, frequency of movement 0.5 Hz, gap thickness 0.1 mm and 20 °C temperature. The results are normalized on the y-axis.

From the figure (Figure 5.7), it´s evident that Power-Law and Herschel-Bulkley models do not accurately capture the behavior of the grease in this application. This observation is further supported by the results presented in table (Table 5.5), where the mean percentage difference (MPD) is approximately 95 % for both models.

The Cross and Carreau model demonstrates a better match during both loading and unloading phases, although the force magnitude is slightly lower compared to the measured values, which can be attributed to the measurement inaccuracy.

Table 5.5: The results of simulation compared to measured data for each material model with conditions: 20 mm x 20 mm upper plate dimensions, frequency of movement 0.5 Hz, gap thickness 0.1 mm and 20 °C temperature.

Non-Newtonian fluid model	**MPD (%)**	**RMSE (N)**
Power-Law model	106.8002	0.4583
Herschel-Bulkley model	87.2534	0.4469
Cross model	19.0748	0.07195
Carreau model	24.8536	0.0912

Considering the difference between the Carreau model and Cross model is only 5 % (according to MPD), it is imperative to conduct further simulations to determine the most suitable material model. Due to the considerable computational time required, the simulations will be limited to a upper plate dimensions 20 mm x 20 mm under both temperature conditions. The results for temperature 20 °C are listed in tables (Table 5.6), (Table 5.7) and (Table 5.8).

Table 5.6: Results of simulations for temperature 20 °C with upper plate dimensions 20 mm x 20 mm at gap thickness 0.05 mm.

Gap thickness 0.05 mm, Temperature 20 °C			
Frequency	**Results**	**Cross model**	**Carreau model**
0.125 Hz	MPD	14.5621 %	14.5273 %
	RMSE	0.0515 N	0.0467 N
0.25 Hz	MPD	8.2194 %	9.5436 %
	RMSE	0.0351 N	0.0319 N
0.5 Hz	MPD	12.7797 %	17.4425 %
	RMSE	0.0494 N	0.0705 N

Table 5.7: Results of simulations for temperature 20 °C with upper plate dimensions 20 mm x 20 mm at gap thickness 0.1 mm.

Gap thickness 0.1 mm, Temperature 20 °C			
Frequency	**Results**	**Cross model**	**Carreau model**
0.25 Hz	MPD	29.1692 %	27.6875 %
	RMSE	0.0755 N	0.0829 N
0.5 Hz	MPD	19.0748 %	24.8536 %
	RMSE	0.0720 N	0.0912 N
1 Hz	MPD	60.8084 %	70.6477 %
	RMSE	0.1078 N	0.1411 N

Table 5.8: Results of simulations for temperature 20 °C with upper plate dimensions 20 mm x 20 mm at gap thickness 0.2 mm.

Gap thickness 0.2 mm, Temperature 20 °C			
Frequency	**Results**	**Cross model**	**Carreau model**
1 Hz	MPD	23.8149 %	28.7920 %
	RMSE	0.1215 N	0.1462 N
2 Hz	MPD	24.3154 %	51.1153 %
	RMSE	0.1704 N	0.2152 N
4 Hz	MPD	56.8149 %	44.4645 %
	RMSE	0.2987 N	0.2980 N

For better clarity the results are shown graphically in figure (Figure 5.8). It is evident that Cross fluid model is more adequate for this kind of application. The average Mean percentage difference for Cross model is $MPD_{Average,Cross} = 27.73\,\%$ and for Carreau model the value is $MPD_{Average,Carreau} = 32.12\,\%$. Even tho the difference is still just 5 %, the difference is consistent for almost every simulation performed, and thus the selected non-Newtonian fluid model for temperature 20 °C is Cross model for better match with measured data.

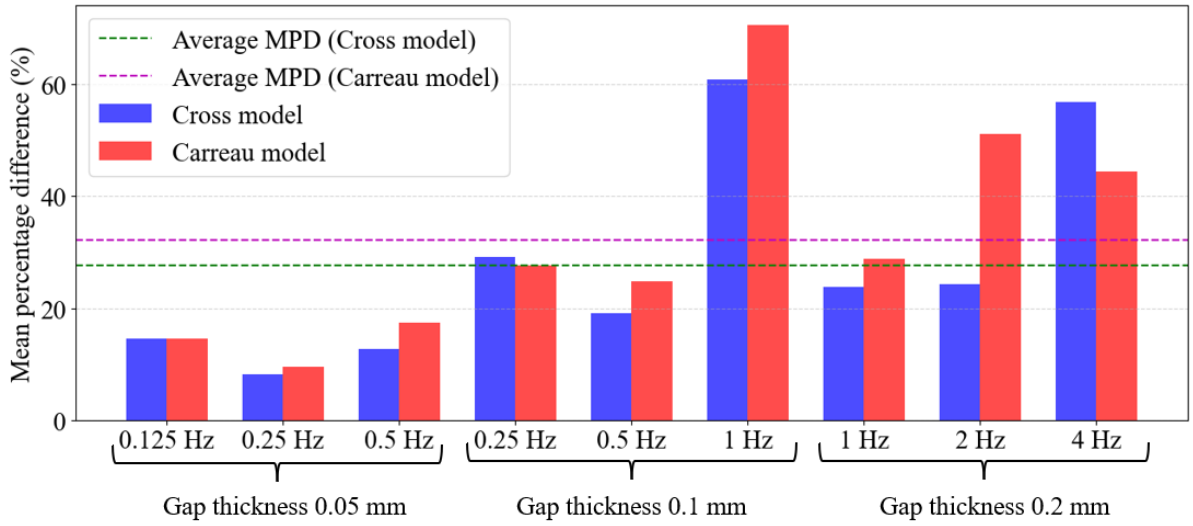

Figure 5.8. The graphic representation of results for Cross and Carreau material model calculated for upper plate with dimensions 20 mm x 20 mm at temperature 20 °C.

Same simulations were done for temperature 40 °C. The upper plate dimensions are 20 mm x 20 mm for each simulation. The results for gap thickness 0.1 mm and movement frequency 0.5 Hz are shown in figure (Figure 5.9) and the results for this exact simulation are listed in the table (Table 5.9).

Considering only experimental data for two temperatures (20 °C and 40 °C) were provided, the fluid models will be chosen separately for each temperature. That means that the model for 40 °C can be different than model for 20 °C, instead of one model for both temperatures with Arrhenius law included.

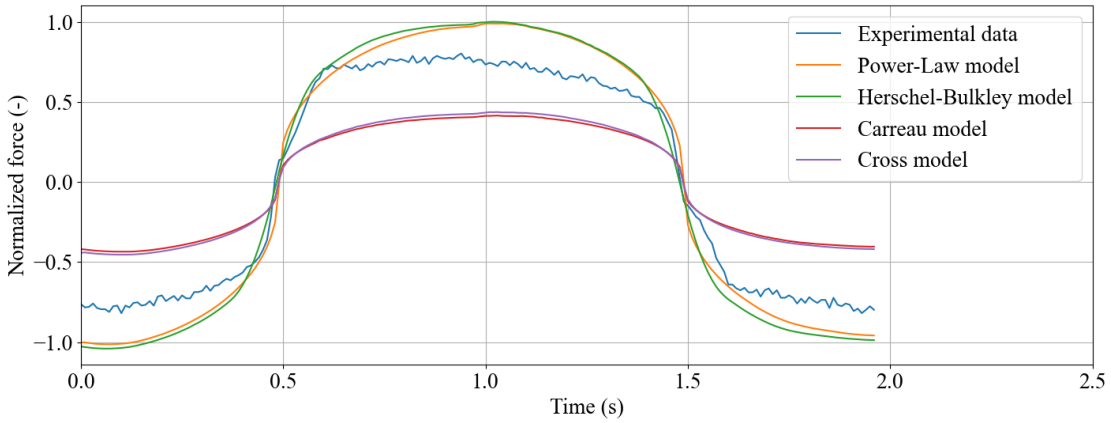

Figure 5.9. The results of calculation with varying non-Newtonian model compared with experimental measurement with conditions: 20 mm x 20 mm upper plate dimensions, frequency of movement 0.5 Hz, gap thickness 0.1 mm and 40 °C temperature. The results are normalized on the y-axis.

From the figure (Figure 5.9) it is evident that the Power-Law and Herschel-Bulkley model are slightly better fit to measured data than Carreau and Cross fluid model. This observation is further supported by the results presented in the table (Table 5.9), where the Cross and Carreau models have approximately doubled values of MPD and RMSE. For this reason, only Power-Law and Herschel-Bulkley models will be used in further simulation to find the most appropriate fluid model for temperature 40 °C.

Table 5.9: The results of simulation compared to measured data for each material model with conditions: 20 mm x 20 mm upper plate dimensions, frequency of movement 0.5 Hz, gap thickness 0.1 mm and 20 °C temperature.

Non-Newtonian fluid model	**MPD (%)**	**RMSE (N)**
Power-Law model	34.7570	0.0903
Herschel-Bulkley model	29.3873	0.1005
Cross model	19.0748	0.07195
Carreau model	50.7499	0.0912

Same as for room temperature, the difference between Power-Law and Herschel-Bulkley is only approximately 5 %, and thus it is imperative to conduct further simulations to determine the most suitable material model for temperature 40 °C. The results are listed in the tables (Table 5.10), (Table 5.11) and (Table 5.12).

Table 5.10: Results of simulations for temperature 40 °C with upper plate dimensions 20 mm x 20 mm at gap thickness 0.05 mm.

Gap thickness 0.05 mm, Temperature 40 °C			
Frequency	**Results**	**Power-Law model**	**Herschel-Bulkley model**
0.125 Hz	MPD	16.6975 %	25.9002 %
	RMSE	0.0464 N	0.0683 N
0.25 Hz	MPD	23.5306 %	40.5212 %
	RMSE	0.0791 N	0.0994 N
0.5 Hz	MPD	26.9300 %	35.2290 %
	RMSE	0.1163 N	0.1376 N

Table 5.11: Results of simulations for temperature 40 °C with upper plate dimensions 20 mm x 20 mm at gap thickness 0.1 mm.

Gap thickness 0.1 mm, Temperature 40 °C			
Frequency	**Results**	**Power-Law model**	**Herschel-Bulkley model**
0.25 Hz	MPD	28.8298 %	26.5597 %
	RMSE	0.0504 N	0.0683 N
0.5 Hz	MPD	34.7570 %	29.3873 %
	RMSE	0.0903 N	0.1005 N
1 Hz	MPD	48.3922 %	46.7305 %
	RMSE	0.1540 N	0.1660 N

Table 5.12: Results of simulations for temperature 40 °C with upper plate dimensions 20 mm x 20 mm at gap thickness 0.2 mm.

Gap thickness 0.2 mm, Temperature 40 °C			
Frequency	**Results**	**Power-Law model**	**Herschel-Bulkley model**
1 Hz	MPD	49.7572 %	56.5335 %
	RMSE	0.1297 N	0.1501 N
2 Hz	MPD	77.3244 %	83.4577 %
	RMSE	0.2258 N	0.2403 N
4 Hz	MPD	107.3460 %	132.1026 %
	RMSE	0.3173 N	0.3372 N

For better clarity the results are shown graphically in figure (Figure 5.10). The average Mean percentage difference for Power-Law model is $MPD_{Average,Power-Law} = 45.95\,\%$ and for the Herschel-Bulkley model, it is $MPD_{Average,Herschel-Bulkley} = 52.94\,\%$. These values highlight that the Power-Law model is more suitable for this application at temperature 40 °C. Although the average MPD difference between the models is only 5 %, this difference remains consistent across all shear rates. Therefore, the Power-Law model is selected as the preferred fluid model at 40°C due to its closer match with the measured data.

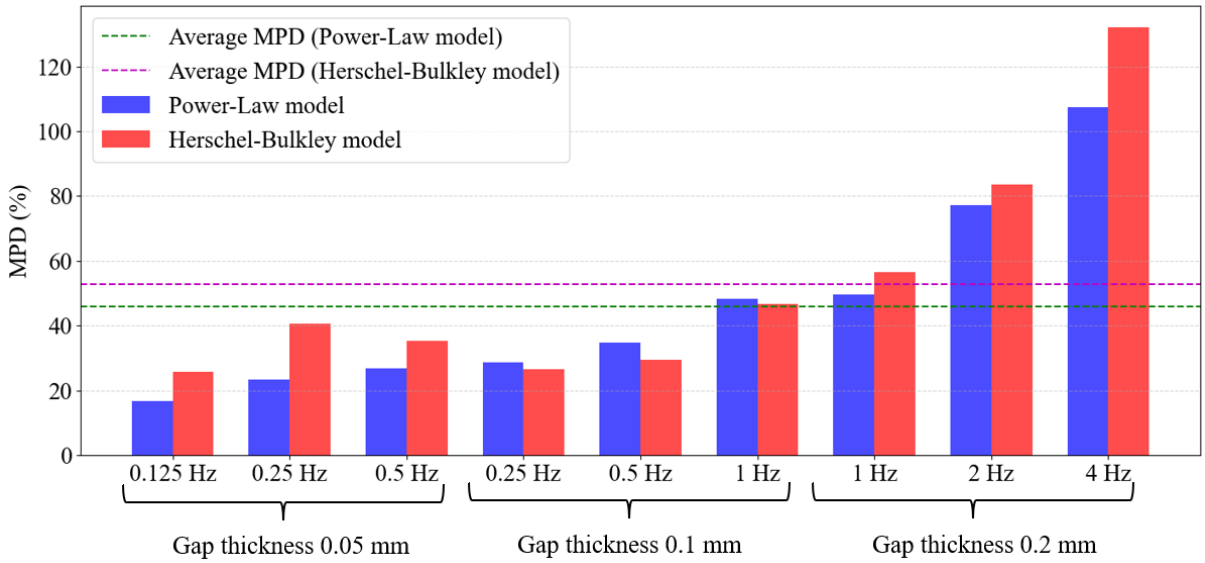

Figure 5.10. The graphic representation of results for Power-Law and Herschel-Bulkley material model calculated for upper plate with dimensions 20 mm x 20 mm at temperature 40 °C.

5.2.3 Comparison simulation vs. experiment vs. analytical model

The goal of this subsection is to compare the simulation data with the experimental data and with analytical model derived in the section (Section 4.1).
The final shape of equation for calculating the force magnitude is (Equation 5.6).

$$F_{frictional} = \mu(\dot{\gamma}) \cdot \frac{U}{h} \cdot S \tag{5.6}$$

Where: $F_{frictional}$ (N) represents the frictional force acting upon the moving plate, S (m^2) is the area of the moving plate, μ $(m^2 \cdot s^{-1})$ is the dynamic viscosity of the fluid between the plates that is function of shear rate $\dot{\gamma}$ (s^{-1}), U $(m \cdot s^{-1})$ is the speed of the moving plate in the x_1 direction and h (m) is the gap between the parallel plates.

The apparent viscosity for Cross model is defined as (Equation 5.7) with given assumptions described in subsection (Subsection 3.4.4).

$$\eta_a = \frac{\eta_0}{1 + (\lambda \cdot \dot{\gamma})^{1-n}} \tag{5.7}$$

Where: η_a $(Pa \cdot s)$ describe the apparent viscosity, η_0 $(Pa \cdot s)$ represents the viscosity at zero shear rate, λ (s) is the time constant and n (-) represents the flow behavior index.

The comparison between measured data, simulation data and analytical solution using combination of equations (Equation 5.7) and (Equation 5.6) is shown in figure (Figure 5.11). It can be clearly seen that the simulation and analytical data are in very good agreement for temperature 20 °C and therefore the Cross fluid model. The slight difference between the force can be caused by grease rolling in front of the moving upper plate, which is not considered in analytical equation or any other assumption that was established during the analytical formula derivation, for example the steady-state assumption.

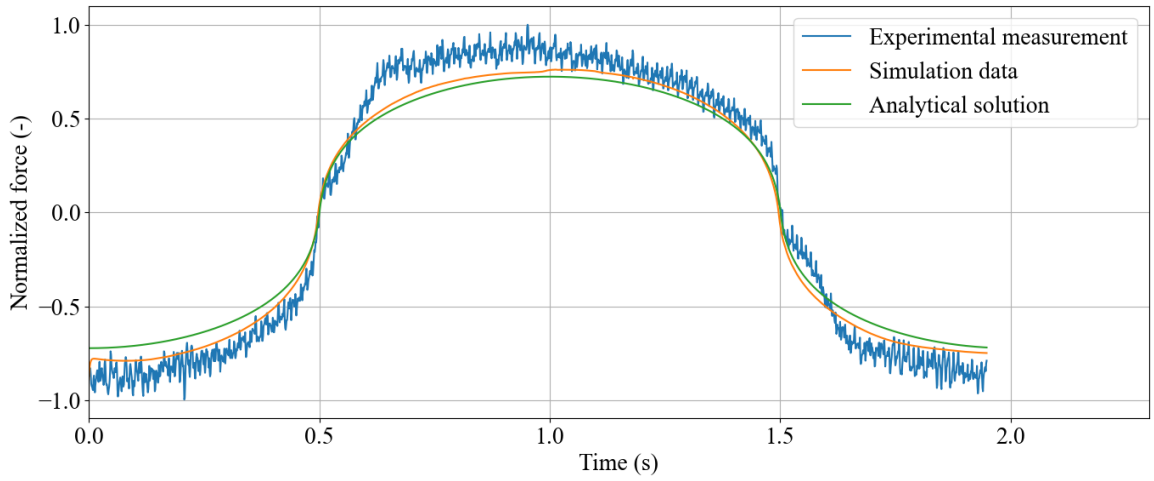

Figure 5.11. The comparison of results obtained by experimental measurement, CFD simulation and analytical solution. The results are shown for temperature 20 °C, movement frequency 0.5 Hz, gap thickness 0.1 mm and upper plate dimensions 20 mm x 20 mm. The results are normalized on the y-axis.

The fluid model selected for temperature 40 °C is Power-Law model. The apparent viscosity for Power-Law model can be calculated using equation (Equation 5.8).

$$\eta_a = K \cdot \dot{\gamma}^{n-1} \cdot H(T) = K \cdot \dot{\gamma}^{n-1} \tag{5.8}$$

By substituting the apparent viscosity into the equation (Equation 5.6) the solution can be acquired using simple calculation.

The comparison for temperature 40 °C between the experimental measurement, CFD simulation and the obtained analytical solution is shown in figure (Figure 5.12). Same as for temperature 20 ° C, the results are very similar.

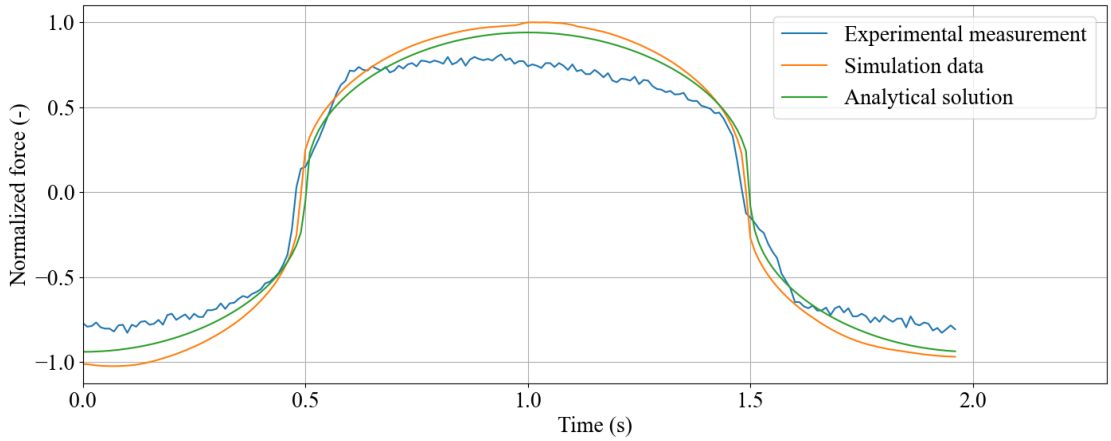

Figure 5.12. The comparison of results obtained by experimental measurement, CFD simulation and analytical solution. The results are shown for temperature 40 °C, movement frequency 0.5 Hz, gap thickness 0.1 mm and upper plate dimensions 20 mm x 20 mm. The results are normalized on the y-axis.

The slight difference between the CFD simulation and analytical solution can be the grease rolling in front of upper moving plate, or the fact, that the analytical solution assumes steady state flow, instead of transient which is calculated in this CFD simulation.

It is worth noting the value of residuals during calculations. The continuity residual stayed below the value 1e-5 throughout the calculation and the x-velocity and y-velocity residuals stayed below the value 1e-7 during the calculations. These values indicate a sufficient level of accuracy, allowing to consider the calculation as converged.

5.3 3-D simulation

The purpose of this simulation is to validate whether the 2-D model (Section 5.1) is precise enough to accurately capture the behavior of grease between two plates. Therefore, the geometry corresponds to the experimental setup - bottom plate, upper plate and grease between them. The geometry is shown in figure (Figure 5.13). To minimize the geometry and thus the mesh size, the model is modelled using symmetry in the half of the plate and the plate 10 mm x 10 mm was selected.

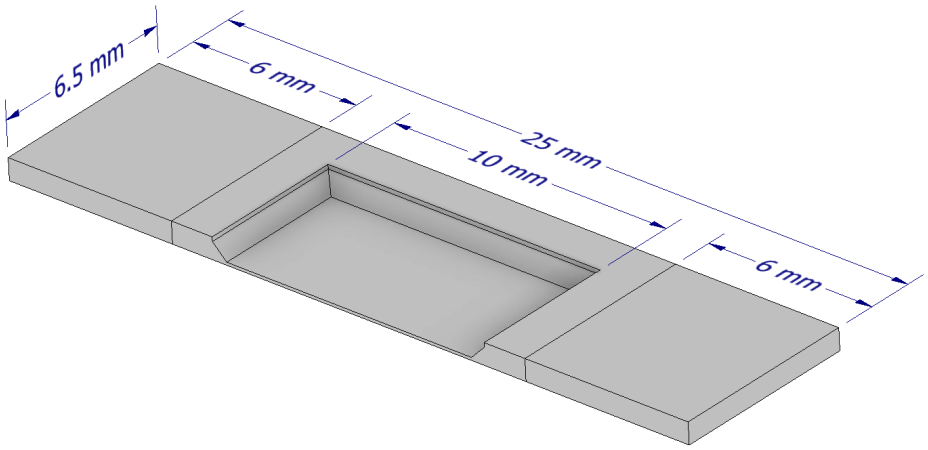

Figure 5.13. The geometry of 3-D simulation with the main dimensions plotted, the gap thickness is 0.1 mm.

5.3.1 Simulation setting

Considering the flow conditions are the same as those for the 2-D simulation, the viscous model is set to laminar. The multiphase model is configured as Volume of Fluid (VOF) with explicit formulation. Grease is defined as the primary phase, and air as the secondary phase. The interaction between the grease and air is modeled with a constant surface tension coefficient $\sigma = 0.031\ N \cdot m^{-1}$.

To capture the effects of grease near the moving wall, the surface tension force modelling is enabled with continuum surface force and wall adhesion setting. Where the contact angle is set as $\theta = 30\,^{\circ}$

5.3.2 Boundary conditions

The boundary conditions are shown in figure (Figure 5.15) and (Figure 5.16). The whole domain is divided into four domains. The Fluid (middle) is moving according to User Defined Function (UDF) shown in figure (Figure 5.14). Due to the high time consumption of the 3-D calculation, the amplitude and frequency of the movement is different than values listed in the table (Table 5.3). The 2-D simulation was performed with the same settings as 3-D simulation for comparable results.

```
#include "udf.h"
#include "dynamesh_tools.h"
#define DEBUG 0

DEFINE_CG_MOTION(moving_wall1,dt,vel,omega,time,dtime)
{

    NV_S (vel, = , 0.0);
    vel[1] = 0.0049*cos(3.1397*time);

}
```

Figure 5.14. User Defined Function for 3-D simulation.

The fluid domains at the sides - Fluid (left) and Fluid (right) are re-meshing using dynamic mesh with method Layering. The pressure outlets (shown as blue) are set to Gauge pressure = 0 Pa. The walls are set to stationary, with no-slip conditions and contact angle set to $\theta = 30\,°$.

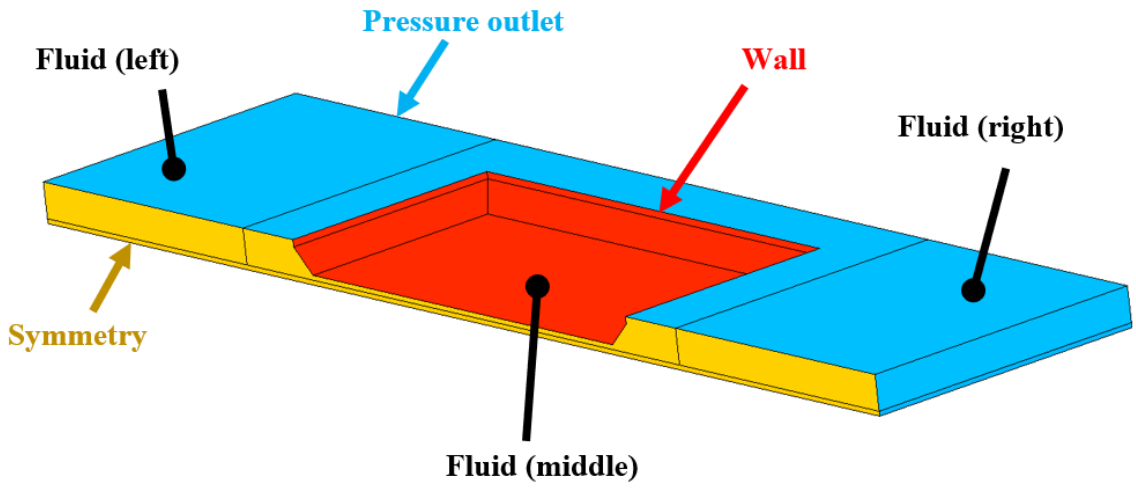

Figure 5.15. The boundary conditions of the 3-D geometry.

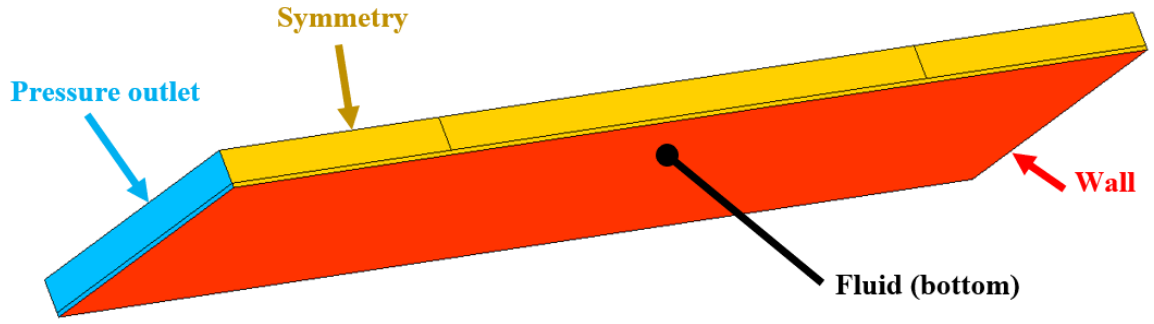

Figure 5.16. The boundary conditions of the 3-D geometry. The view is taken from the bottom of the geometry, looking from the back side.

5.3.3 Mesh

The Ansys meshing software was used to generate mesh. In the domains Fluid (left), Fluid (right) and Fluid (bottom) is the structured hexahedral mesh. In the domain Fluid (middle) it is not possible to create a geometry decomposition, that would allow for a structured mesh. Therefore the unstructured tetrahedral mesh is used. The mesh is shown in figure (Figure 5.17).

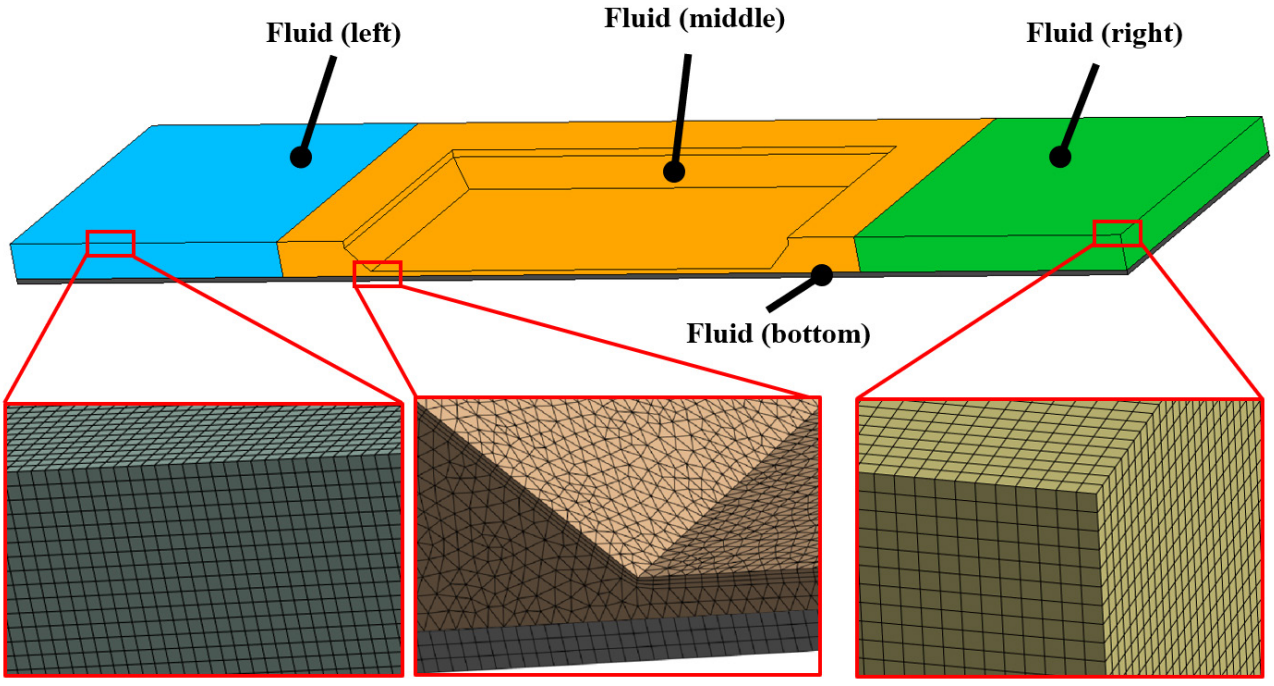

Figure 5.17. The whole mesh of the 3-D geometry and 3 details of different places - The left domain, the area near wall (middle and bottom domain), and the right domain.

The mesh comprises 17 869 884 elements and 10 546 650 nodes. The quality of the mesh is depicted in the table (Table 5.13).

Table 5.13: Mesh quality of the 3-D geometry.

Metrics	Minimum	Average	Maximum
Element quality	0.16514	0.8798	1
Aspect ratio	1.01154	1.6632	11.01
Skewness	1.3037e-10	0.13269	0.79995

To facilitate domain movement, the Layering method in dynamic meshing is employed. Same as for 2-D simulation, the method is set as cell based, with split factor set as $\alpha_s = 0.4$ and collapse factor set as $\alpha_c = 0.2$.

5.3.4 Solution setting

All the settings of the solution methods are listed in the table (Table 5.14). Additionally, the solver is set to Double Precision.

Table 5.14: Solution methods used for calculation of 2-D geometry.

	Setting
Scheme	SIMPLE
Gradient	Least square cell based
Pressure	PRESTO!
Momentum	QUICK
Volume fraction	Modified HRIC
Transient formulation	First order implicit

The time step was determined based on the condition (Equation 5.2) specified by dynamic mesh method. Because the time step size was not small enough, the second method of time step size evaluation is based on Courant number magnitude. The Courant number can be defined as the number of mesh cells traveled at a given time step, mathematically expressed as (Equation 5.9).

$$C = \frac{U \cdot \Delta t}{\Delta h} \tag{5.9}$$

Where: C (-) is the Courant number, Δt (s) represents the time step size and Δh (m) refers to the characteristic size of the mesh cell.

Generally the Courant number is advised to be smaller than 1, ideally smaller than 0.7. [69] [70] That can be mathematically expressed as (Equation 5.10).

$$C = \frac{U \cdot \Delta t}{\Delta h} < C_{max} = 0.7 \tag{5.10}$$

Where: C (-) is the Courant number, Δt (s) represents the time step size, Δh (m) refers to the characteristic size of the mesh cell and C_{max} (-) is the maximum desired Courant number.

Therefore, the time step size can be calculated as (Equation 5.11). Where the minimal element size is near the wall with size approximately 3.75e-6 m. The maximal velocity of the flow is on the upper wall, with value 0.0049 $m \cdot s^{-1}$.

$$\Delta t_{max} = \frac{C_{max} \cdot \Delta h}{U} = \frac{0.7 \cdot 3.75e-6}{0.0049} = 0.000535\ s \tag{5.11}$$

Due to the calculation failure made with calculated time step size, because of too high global Courant number, the final time step size was halved. Value of the final time step size is therefore 2.5e-4 s (Equation 5.12).

$$\Delta t = 2.5e-4\ s \tag{5.12}$$

This value has proved to be sufficient enough.

5.4 3-D simulation results

There are several purposes of the 3-D simulation of the plates with grease between them. On of the main reasons is to validate, whether the simplification of the calculation to 2-D case is possible, without any major deviation on the results.
The second reason for this calculation is to see the behavior of the grease on the corner of the upper moving plate and the behavior on the sides of the upper moving plate.

Considering the high time consumption of this simulation, only one period of the movement was calculated for comparison of results for 2-D and 3-D simulation. The result is shown in figure (Figure 5.18).

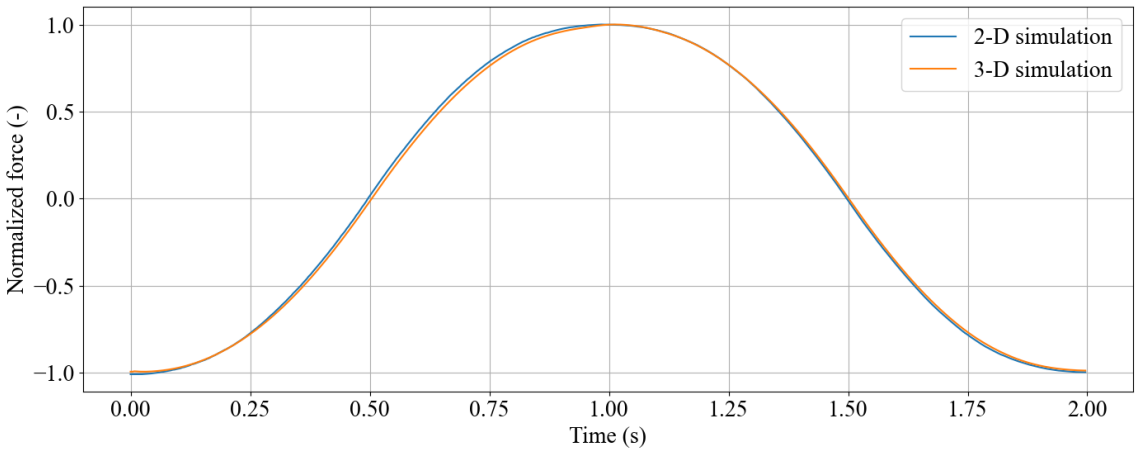

Figure 5.18. Comparison of force acting on upper plate for 2-D simulation and 3-D simulation. The results are normalized on the y-axis.

It is evident that the magnitude of force is consistent in both types of simulations. The minor variation observed occurs during the loading phase, likely due to the 3-D simulation including flow around corners and along the sides of the upper plate, unlike the 2-D simulation.

Also the assumption made for 2-D simulation, that the depth is equal to the 20 mm and area is equal to 400 mm^2 for plate with dimensions 20 mm x 20 mm is correct, even tho the chamfer of the upper plate is slightly reducing these dimensions, because this increase in surface area compensates for the fact that it is not possible to simulate the grease flow around the sides of the upper plate.

The behavior near the corner of the upper moving plate is shown in figure (Figure 5.19). The picture shows, that the area influenced by the corner is only near the corner. Considering this area can be considered small in comparison with whole geometry, the influence is expected to be also small or even negligible.

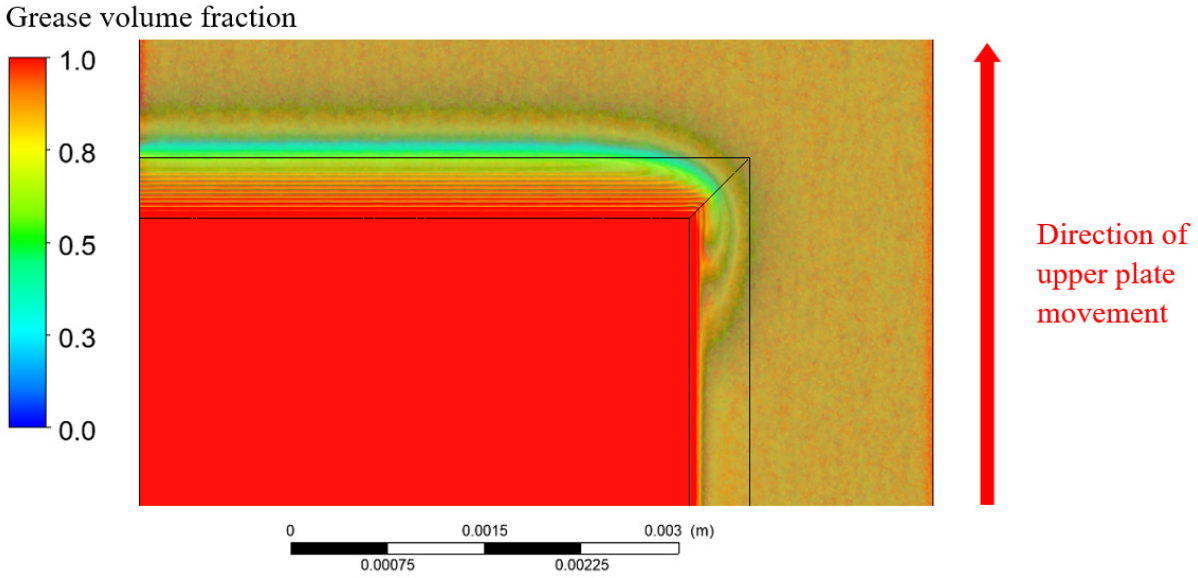

Figure 5.19. View from the top. The behavior of the grease near the corner of the upper moving plate.

The figure (Figure 5.20) illustrates the behavior of grease along the side of the moving plate. It suggests that the region where shear forces act is slightly expanded due to the flow of grease, particularly near the corner (depicted as Area 1 on the figure). This area is gradually rising during the movement, because of grease is pushed out from under the upper plate. This observation supports the use of a 2-D simulation area, specifically for the upper plate measuring 20 mm x 20 mm, chosen as 400 mm^2. Despite the chamfer on the upper plate slightly reducing this area, the slight expansion of the effective region reinforces the validity of this assumption.

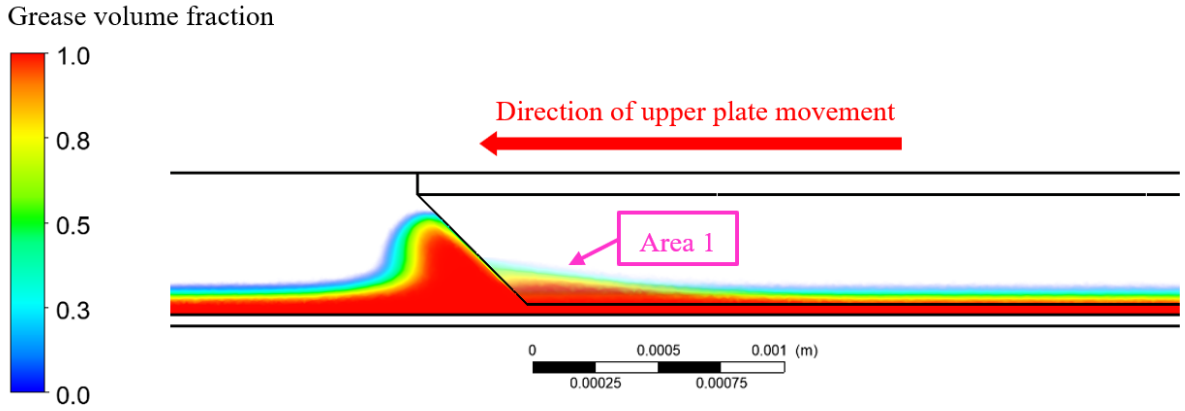

Figure 5.20. View from the side. The behavior of the grease near the corner and along the side of the upper moving plate.

The 3-D simulation can also serve to validate whether the 2-D simulation accurately captures the behavior. Figure (Figure 5.21) demonstrates a notable agreement in the grease behavior ahead of the moving upper plate. This observation is significant because the rolling grease in front of the plate contributes to the generated force. The slight difference can be caused by different type of mesh element and different size of mesh cells in the area of interest.

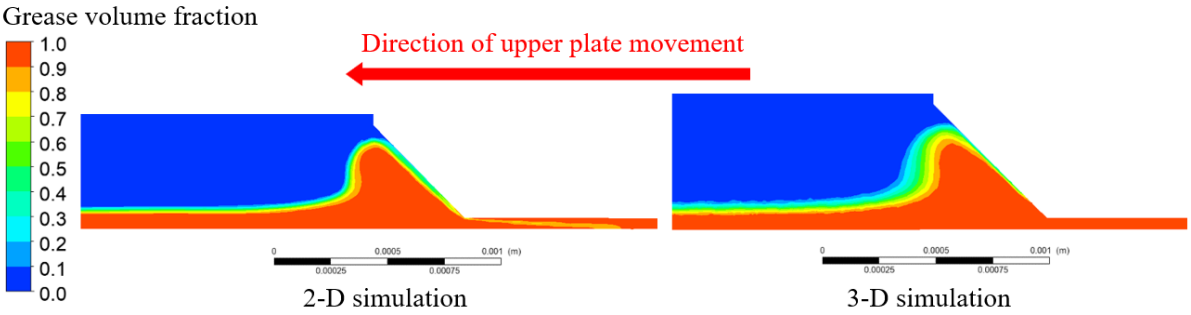

Figure 5.21. View from the side. The behavior of the grease ahead of the upper moving plate for both 2-D and 3-D simulations.

During the upper plate movement the grease ”sticks” to the plate and a depression forms behind the plate. This phenomenon has been observed in both 2D and 3D simulations and the experiment. The depression is shown in figure (Figure 5.22). Again the slight difference can be caused by different mesh in the area of interest.

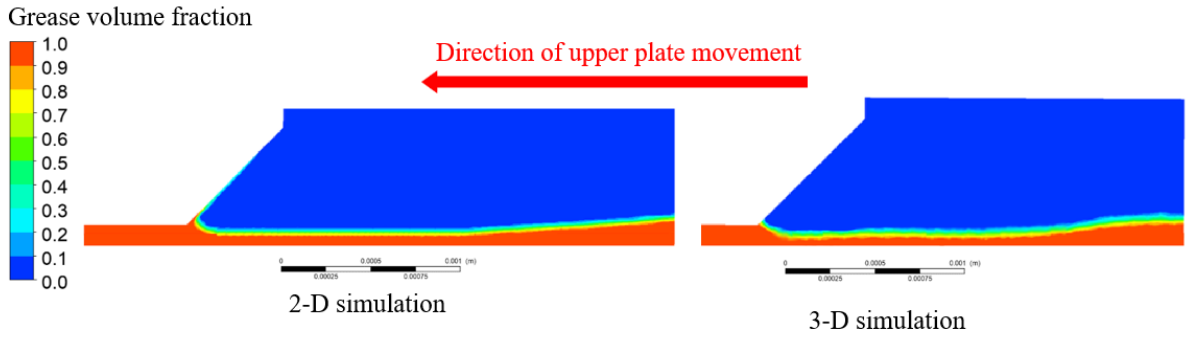

Figure 5.22. View from the side. The behavior of the grease behind the upper moving plate.

In general it can be stated that the simulations in 2-D and 3-D match each other and the difference is only minimal. This was verified in several ways - by comparing the magnitude of the recorded force and by visually comparing the behaviour of the grease in front of and behind the moving plate. In both cases there was significant agreement - the behaviour of the grease at the corners and along the edges of the upper plate did not significantly affect the results. The 2-D simulations can thus be declared as sufficient enough.

It is worth noting the value of residuals during calculations. The continuity residual stayed below the value 1e-3 throughout the calculation and the x-velocity, y-velocity and z-velocity residuals stayed below the value 1e-7 during the calculations. These values indicate a sufficient level of accuracy, allowing to consider the calculation as converged.

5.5 Axisymmetrical simulation

The purpose of this simulation is to calculate the moment acting in the real ball joint geometry, that was acquired in the chapter (Chapter 2). To minimize the mesh size and the complexity of the geometry, the ball joint is modelled as axisymmetrical. The geometry is shown in figure (Figure 5.23).

Figure 5.23. Geometry of the real ball joint, axisymmetrical case.

5.5.1 Simulation setting

Given that the shear rate (gap thickness and wall velocity) is similar to the shear rate in the simulations of the plates, the Reynolds number should also be very similar. This justifies setting the viscous model to laminar. In this case, the air gaps are not modeled, so the multiphase model is turned off.

Since the main velocity is in the circumferential direction (swirl velocity), the solution of the momentum equation in the circumferential direction must be enabled by activating the Axisymmetric Swirl option.

5.5.2 Boundary conditions

The boundary conditions are shown in figure (Figure 5.24). The moving wall (red in the picture) has rotational wall velocity set using User Defined Function, which is shown in figure (Figure 5.25). The conditions of the movement are set to mimic the movement of the real ball joint during initial testing after the ball joint assembly. The procedure is shown in figure (Figure. 5.26) in normalized value in both x-axis and y-axis to ensure the confidentiality of the process.

Two reference values are relevant: the area and the length. The area is set to 0.0008109 m^2 based on the inner moving wall´s surface area. Additionally, the length is set to 0.015 m, corresponding to the radius of the ball stud.

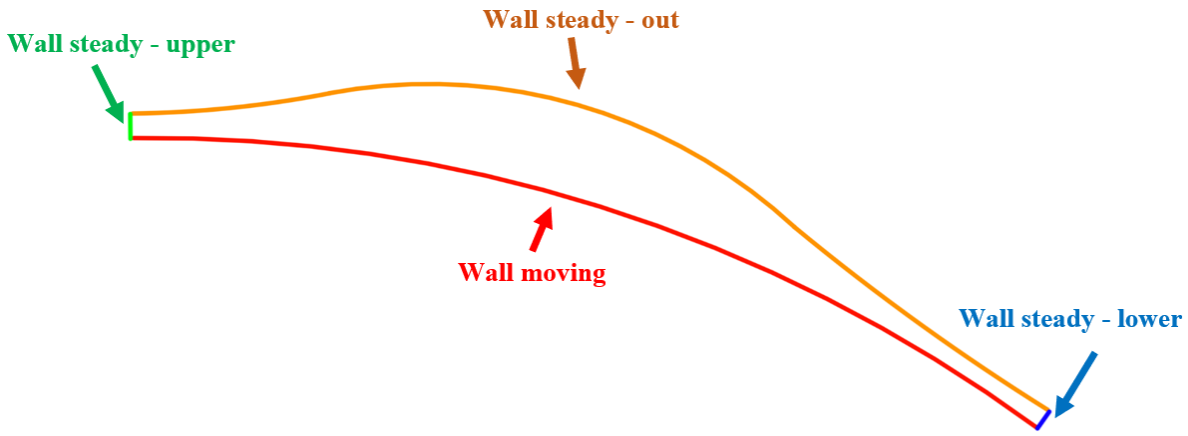

Figure 5.24. The boundary conditions of the axisymmetrical simulations. The figure is not in scale for batter clarity.

```
#include "udf.h"
DEFINE_PROFILE(rotational_velocity, thread, position)
{
    real time = CURRENT_TIME;
    real r, velocity, omega_max;
    //Only one condition is shown, the rest are
       according to the movement during ball joint
       testing
    if (time >= X && time <= Y) // X and Y vary with
       the conditions
    {
        omega_max = A * time + B; // A and B vary with
           the conditions
    }
    face_t f;
    begin_f_loop(f, thread)
    {
        velocity = omega_max;
        F_PROFILE(f, thread, position) = velocity;
    }
    end_f_loop(f, thread)
}
```

Figure 5.25. User Defined Function - Axisymmetrical simulation.

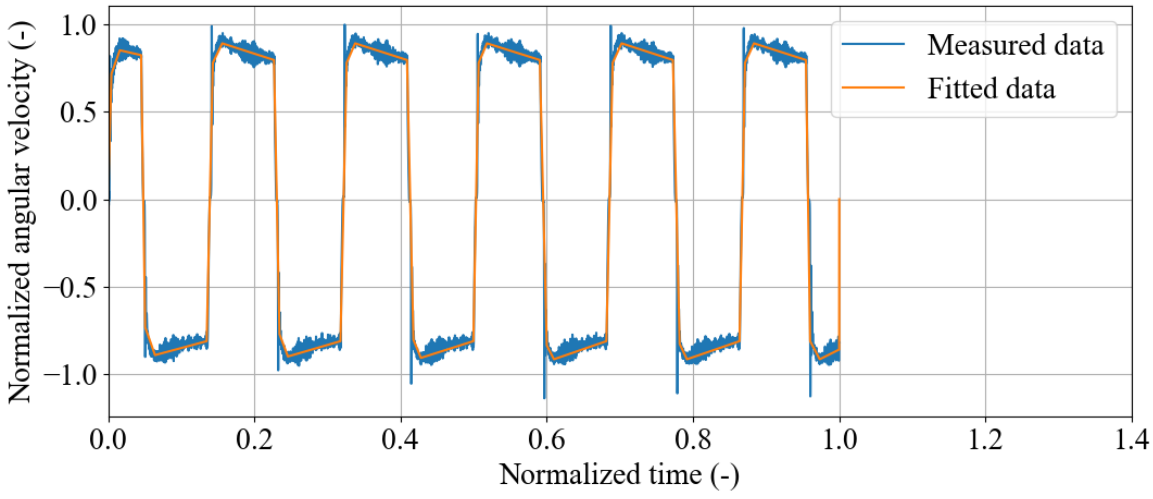

Figure 5.26. The measured data of ball joint movement during the initial testing and fitted data used for axisymmetrical simulation in normalized values on both x-axis and y-axis.

5.5.3 Solution setting

All the settings of the solution methods are listed in the table (Table 5.15). Additionally, the solver is set to Double Precision.

Table 5.15: Solution methods used for calculation of axisymmetrical geometry.

	Setting
Scheme	SIMPLE
Gradient	Least square cell based
Pressure	Second Order Upwind
Momentum	Second Order Upwind
Swirl velocity	Second Order Upwind
Transient formulation	First order implicit

Considering the grease is fully enclosed in the grease layer, and the only movement is rotation of the inner wall, there is no expectation of the complex fluid movement, that would need a short time step size. For that reason the time step size is set to 0.1 s.

5.5.4 Mesh

The software Ansys Meshing was used to generate mesh of the axisymmetrical geometry. The mesh is generated with automatic method, with inflation near the walls. The mesh is shown in figure (Figure 5.27). The mesh comprises mainly from quadrilateral cells.

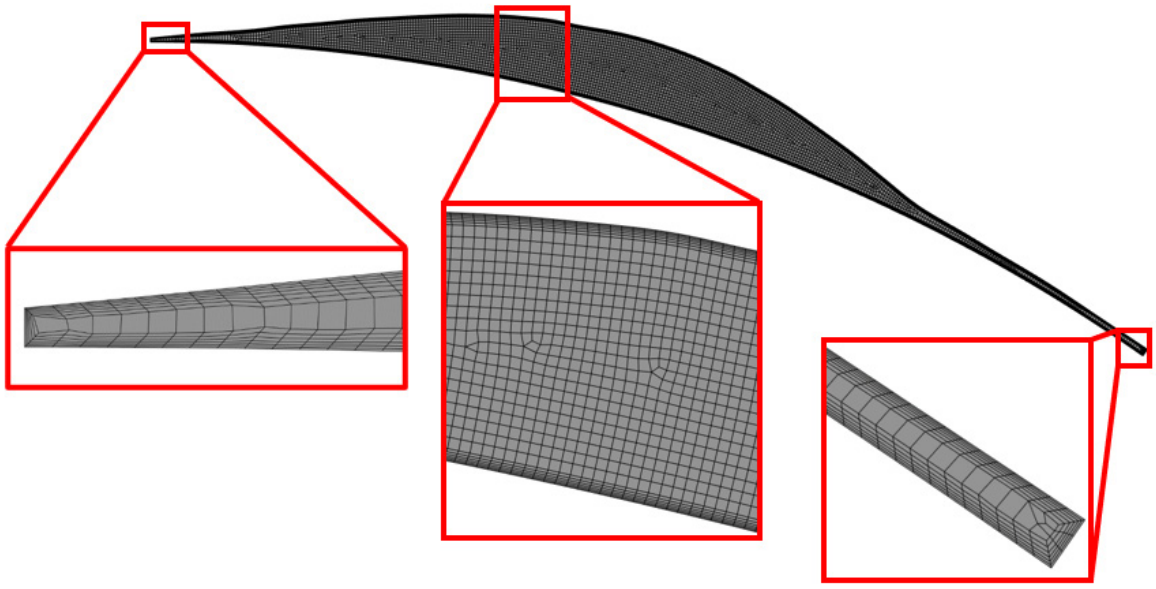

Figure 5.27. The whole mesh of the axisymmetrical geometry with 3 details of important places - two areas near 3 walls and the middle of the geometry.

The mesh consist of 8401 cells and 8763 nodes. The quality of the mesh is depicted in the table (Table. 5.16).

Table 5.16: Mesh quality of the axisymmetrical geometry.

Metrics	Minimum	Average	Maximum
Element quality	4.5667e-002	0.61412	10.99932
Aspect ratio	1	3.9241	33.092
Skewness	4.0036e-004	0.13944	0.65748

5.6 Axisymmetrical simulation results

The results from simulation are compared to experimental measurement data, obtained by measuring on the real ball joint. To maximize the simulation accuracy, the mesh independence study was carried out.

5.6.1 Mesh independence study

The mesh independence study in CFD simulations aims to determine the optimal mesh size for obtaining accurate results. In this specific simulation, which focuses on a single condition rather than multiple scenarios, reducing computational time is not a critical concern. The mesh independence procedure in this case is the same as for 2-D plate geometry, described in the subsection (Subsection 5.2.1). Meaning three calculation were done, one with reference mesh described in the subsection (Subsection 5.5.4), one with finer mesh and one with less cell count. Sizes of the meshes used are listed in the table (Table 5.17).

Table 5.17: Size of each mesh used for mesh independence study.

Element size (m)	Cells count (-)	Node count (-)	MPD (%)	RMSE (Nm)
Mesh - 3k cells	3074	3257	57.5542	6.366e-5
Reference mesh - 8k cells	8401	8763	0	0
Mesh - 26k cells	26716	25997	5.9988	5.2768e-6

Graphical representation of the mesh independence study is shown in figure (Figure 5.28)). It can be seen that the mesh with 3074 cells is slightly shifted in the x-axis compared to the other two calculations. This caused the 57.5542 % difference according to MPD calculation.

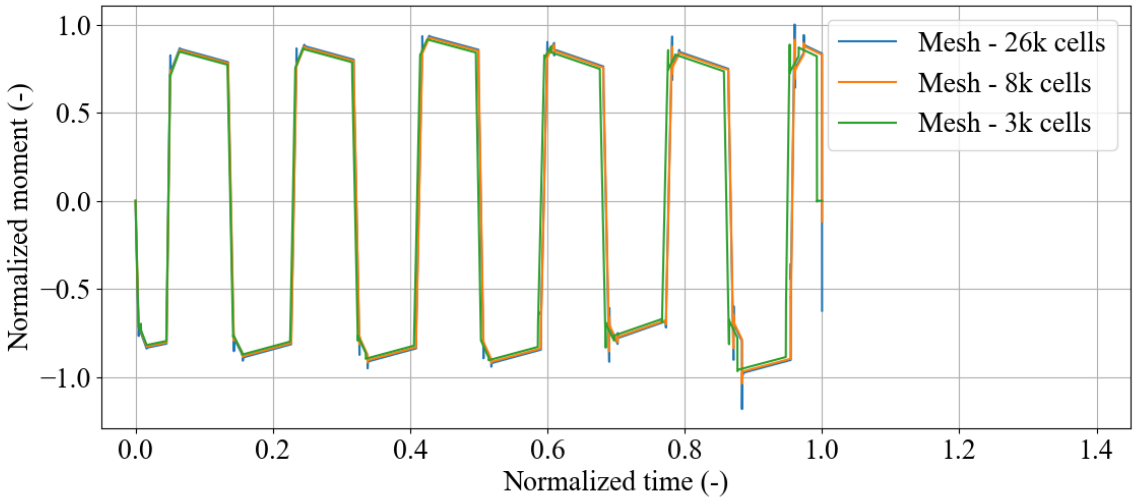

Figure 5.28. The results of mesh independence study for axisymmetrical case. The results are normalized on both x-axis and y-axis.

The difference between the reference mesh (8k cells) and finer mesh (26k cells) is only 6 % according to MPD. From visual inspection the difference is negligible, except the area, where the movement direction is changing and the spikes are occurring. But considering the area of interest is not around the spikes, this difference can be neglected. For these reasons the results calculated with reference mesh is taken as accurate enough.

5.6.2 Experiment vs. simulation

The primary object of this simulation is to the results with the experimental measurement. The comparison is shown in figure (Figure 5.29), where the x-axis and y-axis are normalized to ensure the confidentiality of true scale of measured data.

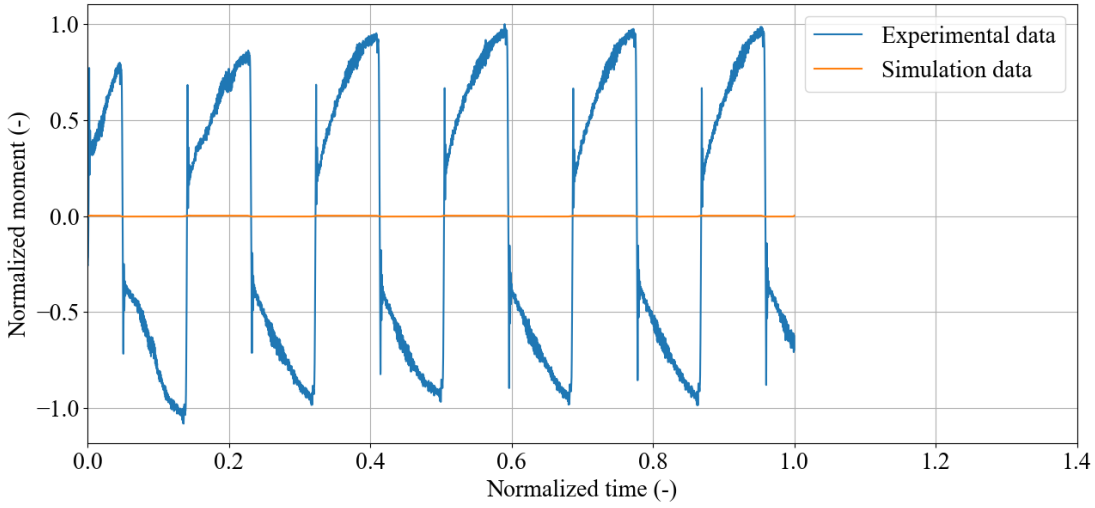

Figure 5.29. The comparison of measured data and data from axisymmetrical simulation. The results are normalized on both x-axis and y-axis.

Even from the visual inspection it can be clearly said, that there is a vast difference between measurement and simulation. The mean percentage difference and root means squared error are calculated and listed in the table (Table 5.18).

Table 5.18: The results of MPD and RMSE calculated for axisymmetrical simulation vs. experimental measurement.

Metric	Result
Mean percentage difference (MPD)	98.2552 %
Root mean square error (RMSE)	1.5066 Nm

Considering the simulation data are much smaller than the experimental data, the moment calculated by the simulation is scaled by 200 for better clarity. This is shown in figure (Figure 5.30).

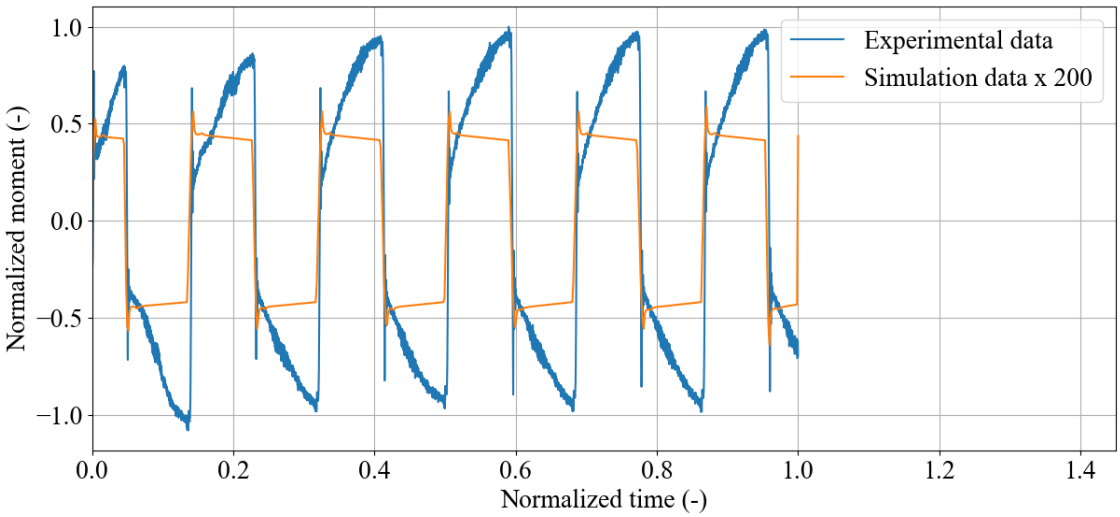

Figure 5.30. The comparison of measured data and data from axisymmetrical simulation scaled by 50. The results are normalized on both x-axis and y-axis.

Upon the visual inspection it can be said, that the simulation data almost perfectly copy the shape of the angular velocity vs. time curve, shown in figure (Figure 5.26). This is probably caused by the fact, that the geometry is considered perfectly axisymmetrical, without changing gap thickness. The simulation is also calculated without the influence of the air gaps. This facts makes this simulation the perfect case of grease layer in the ball joint. The shape of the measured data is different, because it is measure on real ball joint with number of imperfections and most importantly, there is direct contact between the plastic bearing and ball stud in real ball joint.

The contact between plastic bearing and ball stud is also the reason of the high difference between measured and simulated data. The friction in the presence of grease is mostly due to the viscous resistance of the grease itself, which is significantly lower than

the dry friction between the solid surfaces.

The figure (Figure 5.30) shows that there are spikes of moment magnitude occurring when the direction of the movement is changed during testing. This spike is called breakaway torque moment. It can be seen that the simulation shows the same behavior, even tho the spikes are much smaller. This can indicate, that the grease itself can be contributing to the magnitude of the breakaway torque, due to its behavior.

It is worth noting the value of residuals during calculations. The continuity residual stayed below the value 1e-16 throughout the calculation and the x-velocity, y-velocity residuals stayed below the value 1e-6 during the calculations. The axisymmetrical simulation further solve the velocity in the swirl direction, the residual for swirl stayed below 1e-5.These values indicate a sufficient level of accuracy, allowing to consider the calculation as converged. This also confirms the assumption, that there are no complex fluid movement in this type of simulation and therefore the time step with size 0.1 s is sufficient enough.

5.7 3-D grease layer simulation

The objective of this simulation is to validate whether the 2-D axisymmetrical model described in section (Section 5.5) accurately captures the grease behavior within the real ball joint geometry. The geometry therefore corresponds to geometry of the grease layer obtained in the section (Section 2.8). The geometry is shown in figure (Figure 5.31).

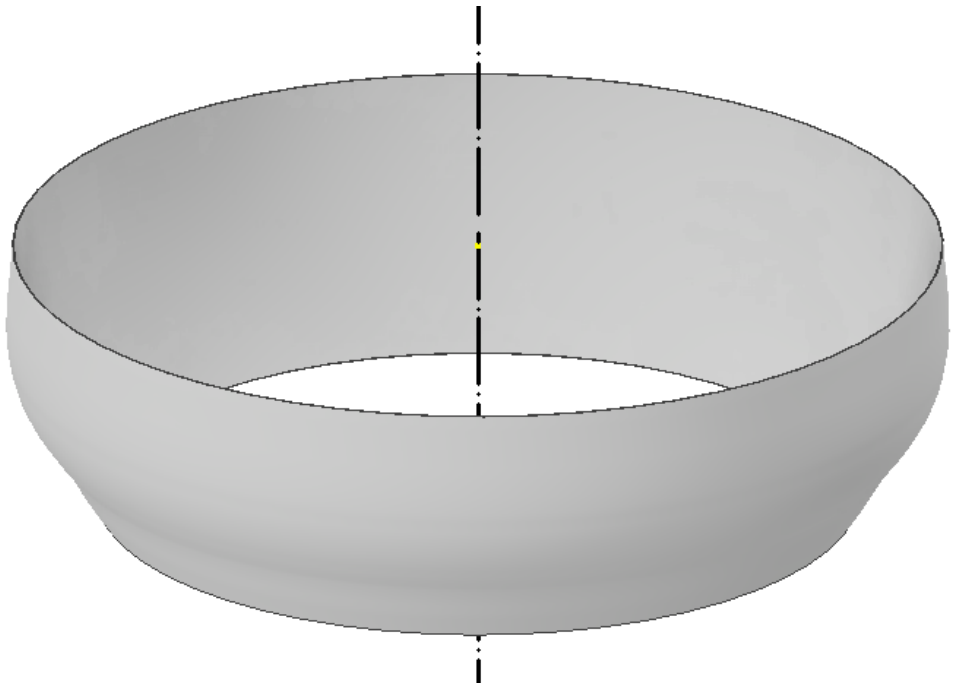

Figure 5.31. The geometry of the grease layer in the real ball joint used for the 3-D simulation.

5.7.1 Simulation settings

Same as for other simulation, the viscous model can be set as laminar, due to high viscosity and low velocities and dimensions. Because only the grease is modelled in this simulation, the single phase model is used.

Considering that the shear rate (gap thickness and wall velocity) closely resembles the shear rate observed in plate simulations and 2-D axisymmetrical simulation, it is reasonable to assume that the Reynolds number will also be similar. Consequently, setting the viscous model to laminar is justified. Additionally, since the air gaps are not explicitly modeled, the multiphase model is disabled.

5.7.2 Boundary conditions

The boundary conditions are shown in figure (Figure 5.33). The moving wall has rotational wall velocity set using User Defined Function shown in figure (Figure 5.32). The conditions of the movement are same as for axisymmetrical simulation, meaning the movement is same as for the initial ball joint testing. This procedure was depicted earlier in figure (Figure 5.26) and is normalized in both x-axis and y-axis to ensure the confidentiality of the process.
Among the reference values, length and area are particularly important. The area is set to 0.0008109 m^2 according to the area of inner moving wall (depicted as red in the figure). The length is set to 0.015 m according to the radius of the ball stud.

```
#include "udf.h"
DEFINE_PROFILE(rotational_velocity, thread, position)
{
    real time = CURRENT_TIME;
    real r, velocity, omega_max;
    //Only one condition is shown, the rest are according to the
       movement during ball joint testing
    if (time >= X && time <= Y) // X and Y vary with the conditions
    {
        omega_max = A * time + B; // A and B vary with the conditions
    }
    face_t f;
    begin_f_loop(f, thread)
    {
        velocity = omega_max;
        F_PROFILE(f, thread, position) = velocity;
    }
    end_f_loop(f, thread)
}
```

Figure 5.32. User Defined Function - 3-D grease layer simulation.

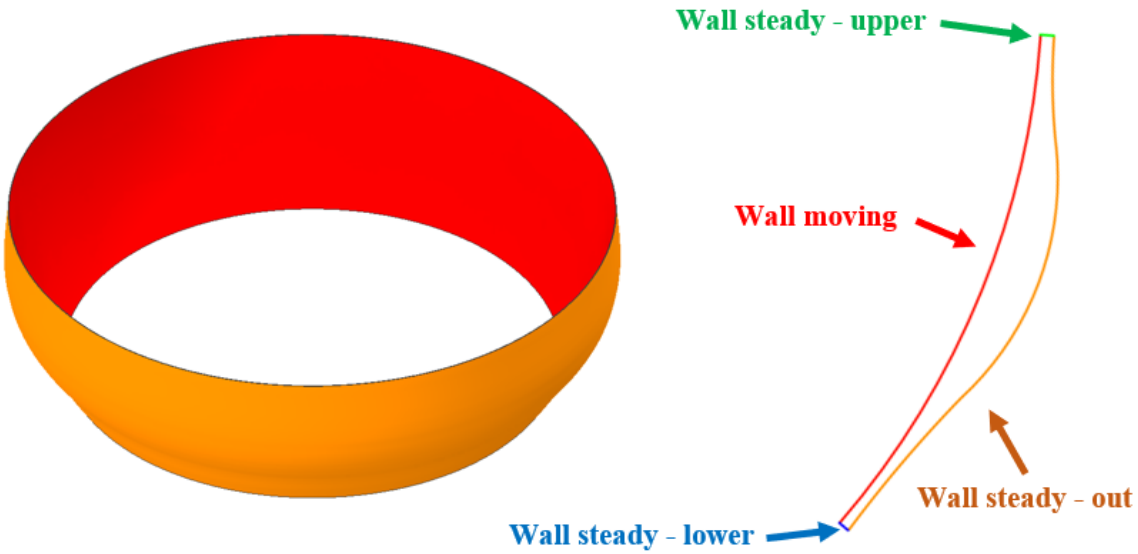

Figure 5.33. The boundary conditions of the full 3-D ball joint geometry. On the right there is the sectional cut through the geometry.

5.7.3 Mesh

The Ansys meshing software was used to generate mesh, which is shown in figure (Figure 5.34). Since the geometry is rotationally symmetric, the Multizone method was used to create the mesh, which is fully structured, meaning the mesh consist of only hexahedral cells.

The reference mesh consist of 278 160 cells and 297 192 nodes. The quality of the mesh is depicted in the table (Table. 5.19).

Table 5.19: Mesh quality of the 3-D grease layer geometry.

Metrics	Minimum	Average	Maximum
Element quality	7.446e-004	6.512e-002	0.4958
Aspect ratio	3.7208	60.774	232.46
Skewness	4.074e-003	0.10041	0.39506

The average aspect ratio 60.774 is relatively high value. This is caused by the fact, that the geometry is long and thin at the same time, so the cells has to be long and thin as well. Considering this can cause a deviation from the correct results, the mesh independence study will be carried out.

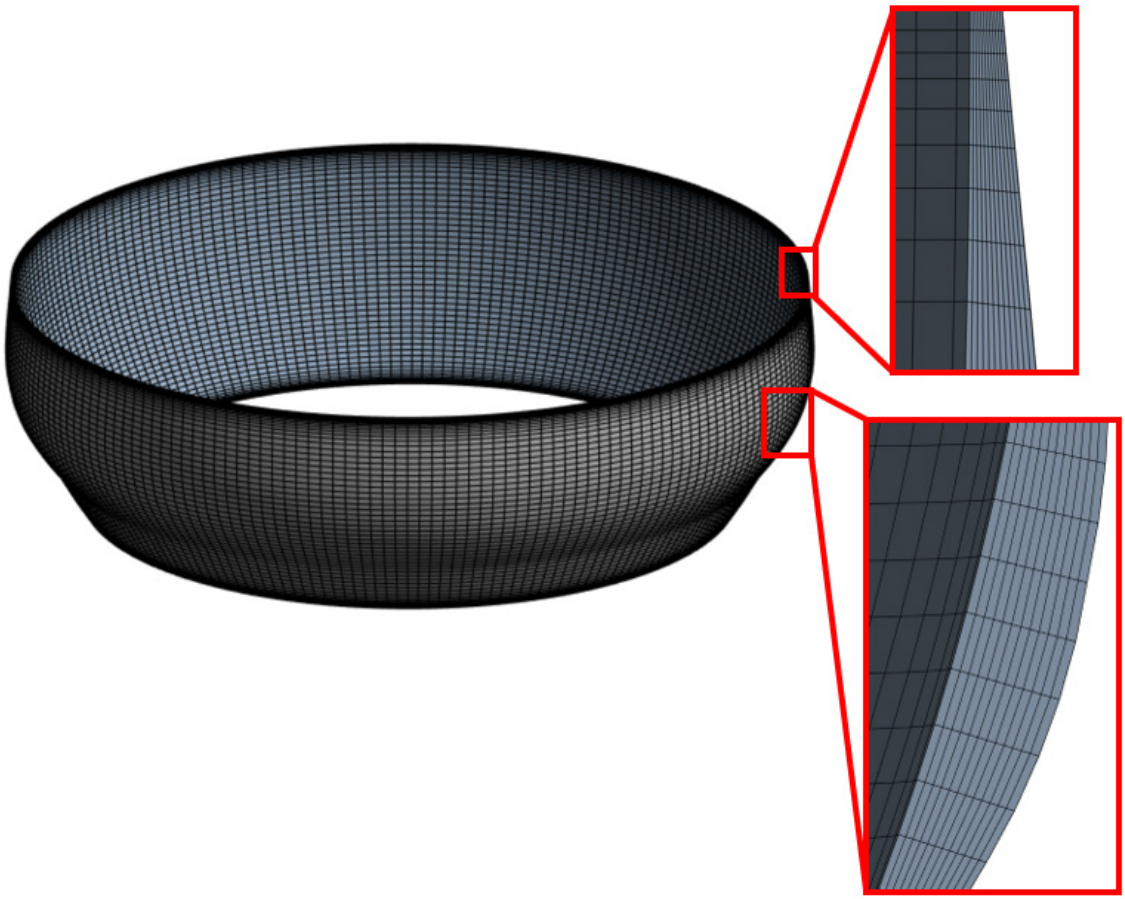

Figure 5.34. The mesh of the 3-D grease layer geometry. Two details on the right show mesh inside the geometry, meaning the pictures are from the cut of the geometry from the place the small rectangle is showing.

5.7.4 Solution settings

All the settings of the solution methods are listed in the table (Table 5.20). Additionally, the solver is set to Double Precision.

Table 5.20: Solution methods used for calculation of 3-D grease layer geometry.

	Setting
Scheme	SIMPLE
Gradient	Least square cell based
Pressure	Second Order Upwind
Momentum	Second Order Upwind
Transient formulation	First order implicit

Considering the grease is fully enclosed in the grease layer, and the only movement is rotation of the inner wall, there is no expectation of the complex fluid movement, that

would need a short time step size. For that reason the time step size is set to 0.1 s. this assumption has been shown to be justified in the case of axisymmetrical geometry, and there is no reason to assume that anything changes for full 3-D geometry.

5.8 3-D grease layer simulation results

The results from this simulation are compared with experimental data measured on the real ball joint and with data obtained from axisymmetrical simulation.

As mentioned earlier, the mesh independence study is carried out, to test whether the size of the mesh cells has an effect on the results.

It is worth noting the value of residuals during calculations. The continuity residual stayed below the value 1e-4 throughout the calculation and the x-velocity, y-velocity and z-velocity residuals stayed below the value 1e-7 during the calculations. These values indicate a sufficient level of accuracy, allowing to consider the calculation as converged.

5.8.1 Mesh independence study

Same as for the axisymmetrical case, this simulation is done purely with one conditions. That means that the reduction of computational time is not primary objective. The main objective is to ensure the results quality. The mesh independence study procedure is same as in the case of 2-D plate geometry and axisymmetrical geometry described in the subsection (Subsection 5.2.1).
Several calculation were done, one with reference mesh described in the subsection (Subsection 5.7.3), one with less cell count and three calculation were done with finer mesh. The sizes of used mesh are listed in the table (Table 5.21).

Table 5.21: Size of each mesh used for mesh independence study for 3-D grease layer geometry.

Mesh type	Cells count	Node count	MPD	RMSE
-	(-)	(-)	(%)	(Nm)
Mesh - 16k cells	34194	40866	6.1273	3.1734e-4
Reference mesh - 60k cells	59340	66792	0	0
Mesh - 122k cells	110544	122200	5.5733	2.5574e-4
Mesh - 280k cells	278160	297192	24.2147	0.0012482
Mesh - 500k cells	494760	528612	24.3022	0.0012533

From the calculated MPD values, it is evident that the mesh with sizes 280k cells and 500k cells have almost similar results. The difference between these two is approximately 0.1 %. Therefore, the final mesh used for calculation is mesh with 280k cells, as the results does not change with finer mesh anymore. The results are also shown graphically

in figure (Figure 5.35). On the figure, it is evident, that the results from two finest meshes is directly on each other, and therefore confirms the results calculated by MPD.

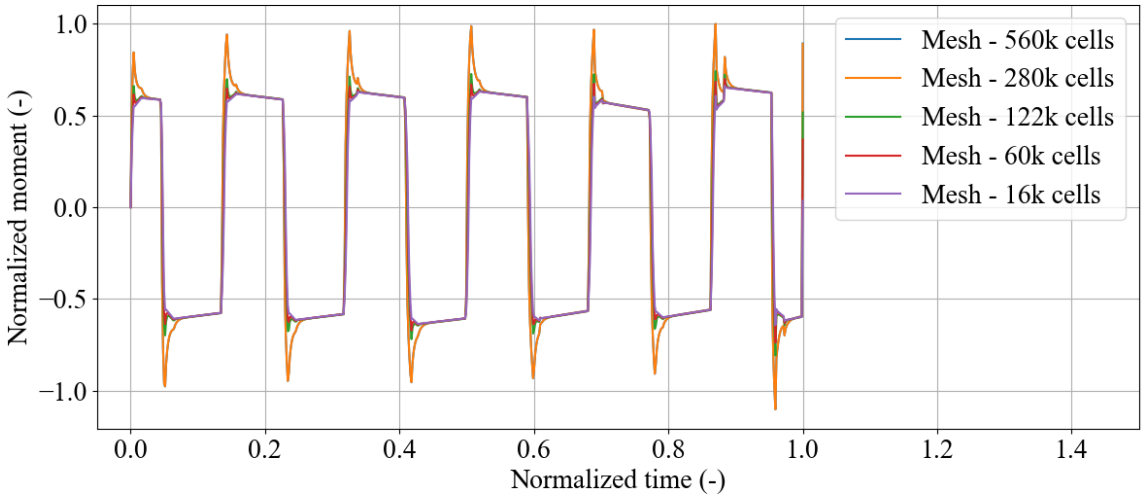

Figure 5.35. The results of calculation with same conditions on different mesh sizes. The results are normalized in both x-axis and y-axis.

5.8.2 Comparison with axisymmetrical case and experiment

The main purpose of this simulation is to validate, whether the simplification of the geometry to 2-D axisymmetrical case is possible, without any major deviation on the results. The results are shown in figure (Figure 5.36).

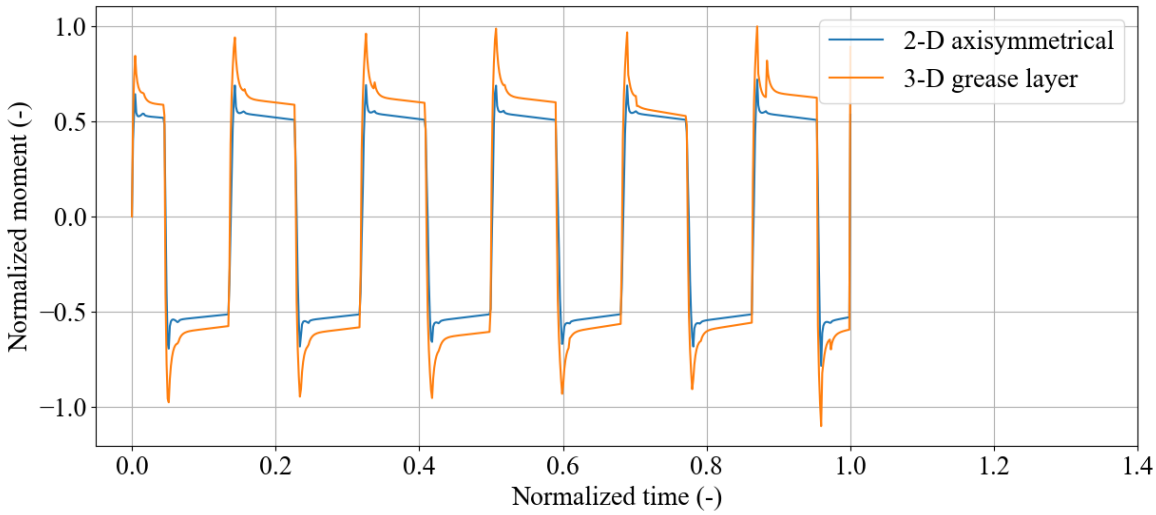

Figure 5.36. Comparison of data from simulation of 2-D axisymmetrical case and 3-D grease layer case. Data are normalized in both x-axis and y-axis.

It is evident that the results differ significantly. The spikes following changes in movement direction are higher in the 3-D simulation. Additionally, the moment magnitude varies in places where the speed remains nearly constant. The total difference is calculated using MPD and RMSE, with MPD at 42.7459 % and RMSE at 0.00129 Nm. Given that the reference values for both simulations are identical, the results should theoretically match. Generally, the 3-D simulation is expected to be more accurate. Therefore, the observed discrepancies suggest that the 2-D axisymmetrical model may not be suitable for this type of application.

Nevertheless, even tho the moment is slightly higher with 3-D simulation, the comparison with experimental data still show vast difference between the moment magnitude. The comparison is shown in figure (Figure 5.37). Same as for axisymmetrical simulation, the vast difference makes the data from simulation almost straight line, for that reason the scaled simulation data are shown in comparison with experimental data in figure (Figure 5.38)

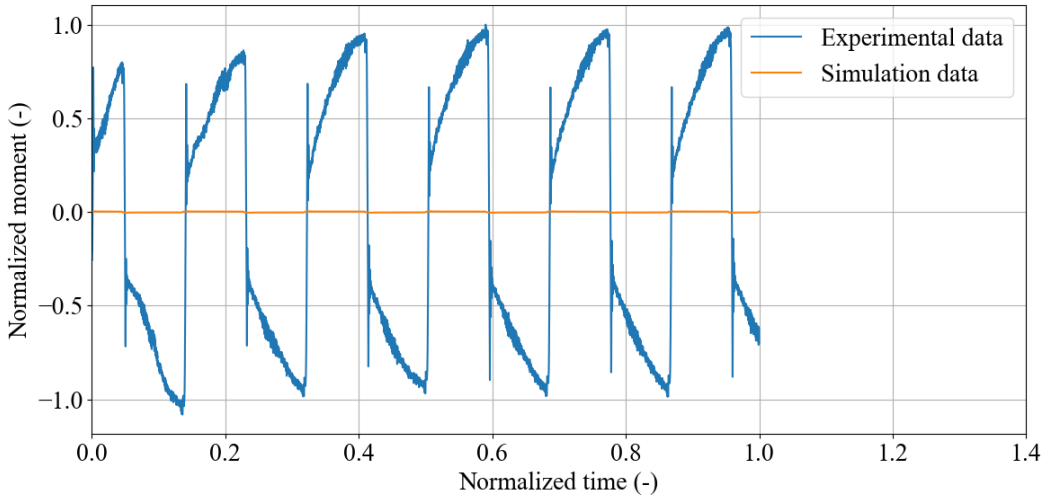

Figure 5.37. Comparison of data from simulation of 3-D grease layer case and experimental data. Data are normalized in both x-axis and y-axis.

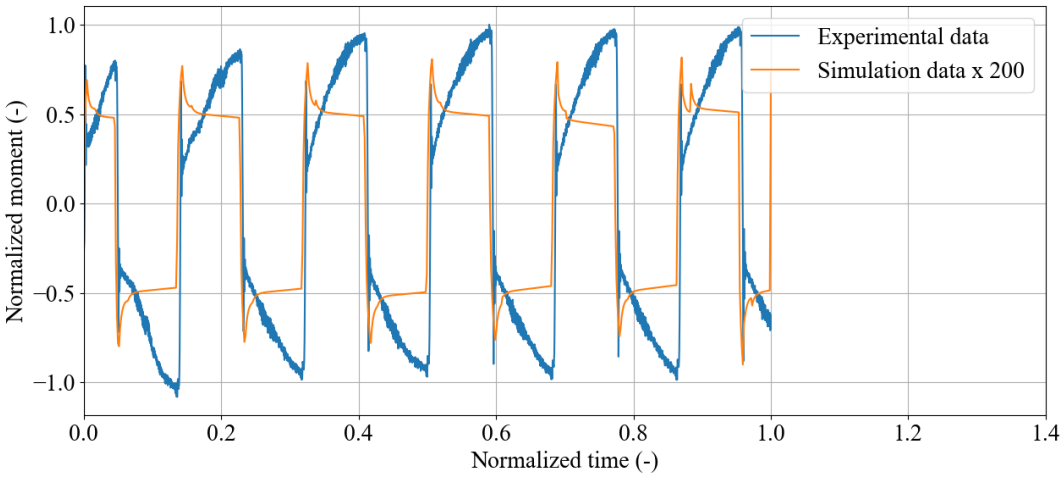

Figure 5.38. Comparison of data from simulation scaled by number 200 of 3-D grease layer case and experimental data. Data are normalized in both x-axis and y-axis.

Same as for axisymmetrical simulation, it can be concluded that the simulation data almost perfectly copy the shape of the angular velocity vs. time curve, shown in figure (Figure 5.26). The geometry even in 3-D is considered perfectly symmetrical without any imperfections. The absence of air gaps can also influence the results.

The main source of difference between the measured moment and simulated moment is still the fact, that there is no dry friction between the plastic bearing and steel ball stud considered in the CFD simulation. The grease viscosity is not nearly high enough to cause that high moment just by shearing.

The spikes observed during changes in movement direction suggest a potential correlation between grease behavior at low shear rates and the presence and magnitude of the breakaway moment. In real ball joints, grease is not only present in the simulated grease layer but also enclosed in small pockets across the plastic bearing surface. Considering that the grease behaves as a solid material when there is no movement, lubrication quality during this phase could be significantly affected.

Conclusion and discussion

This master thesis aims to describe the behavior of grease inside ball joints. The first chapter starts by detailing the parts and components of ball joints and their use in automotive suspension and steering systems. It then provides an overview of the grease used as a lubricant in these joints. Finally, the chapter concludes with a discussion of the properties of ball joints that are crucial for assessing their functionality.

In the X-ray computed tomography section, the process of obtaining the grease layer and air gaps is described. Several tests were conducted, with the first one performed at CEITEC CTLAB on the Brno campus. This initial measurement aimed to gather information about image resolution and contrast among grease, polyoxymethylene, and steel. The results indicated that the resolution and contrast were insufficient.

To address this, a new ball joint was designed, replacing the steel with aluminum and adding tungsten nanoparticles to the grease. This modified ball joint was then tested at the Institute of Physics of the Czech Academy of Sciences in Prague. The fast scan test showed that the contrast and resolution were now adequate for a full scan. The full scan provided a complete geometry of the grease layer, which was used to reconstruct the geometry of air gaps within the ball joint.

To evaluate the thickness of the grease layer, another scan with higher resolution and better contrast between the three components was performed. This sectional scan was used to accurately reconstruct the thickness of the grease layer.

There is potential to further improve this procedure. First, the preparation of the ball joint sample could be enhanced by not only replacing the steel with aluminum but also removing unnecessary material that doesn´t affect the ball joint´s integrity when stationary. This modification would allow for a higher resolution scan with better contrast.

Additionally, it was discovered that the tungsten nanoparticles had the opposite effect, worsening the contrast between the components. The increased overall density reduced the transmittance of the grease. Therefore, avoiding the use of tungsten nanoparticles or exploring alternative contrast agents could lead to better imaging results.

Nevertheless, the findings of this chapter are an important step toward understanding the behavior of grease within the ball joint immediately after assembly. The scans enabled the determination of both the amount of grease present in the ball joint and the quantity of air trapped within the grease layer.

The third chapter focuses on interpolating measured rheograms of non-Newtonian fluid to develop a fluid model. The experimental data provided by the manufacturer included shear stress versus shear rate measurements at two temperatures: 20 °C, corresponding to ball joint operation, and 40 °C, corresponding to ball joint assembly. Additionally, the viscosity-shear rate dependency was calculated from the provided data to stabilize the curve-fitting process. Using Python scripts, four fluid models were obtained for each temperature: Power-law, Herschel-Bulkley, Cross, and Carreau. The quality of the fit was determined using the coefficient of determination, which was higher than 0.99 for all fits, indicating that each model is a good fit to the measured data.

An improvement to this part of the thesis could involve finding the constants for the Arrhenius Law to account for temperature dependency. However, this requires more than two sets of data. Therefore, additional data would need to be provided by the manufac-

turer or measured using a rheometer.

The experimental part of the thesis focuses on determining the force relations during the motion of a plate over a very thin lubricating film. First, an equation describing the magnitude of the force is derived from the Navier-Stokes equation. This equation identifies the factors on which the force depends: gap thickness, speed of the moving plate, fluid viscosity, and the area of the moving plate.

Based on these factors, an experimental measurement was designed. In this experiment, one plate slides over a stationary plate with a specified gap thickness between them filled with grease. Given the dependencies of force magnitude, the conditions of the measurements varied: three different gap thicknesses, three different speeds for each gap thickness, and three types of upper plates with different face areas. Additionally, since viscosity depends on both shear rate and temperature, measurements were conducted at both temperatures.

First, the measurement uncertainty was evaluated, primarily because the force magnitude measured for some conditions was below the sensor range specified by the manufacturer. The sensor´s precision near zero values was found to be sufficient, with a measurement uncertainty of 0.01899 N, which is about 2 % compared to the measured force magnitude of around 1 N.

The issue arises when dealing with values near zero. Measurements taken with an upper plate measuring 10 mm x 10 mm are particularly close to these near-zero values, resulting in a potential measurement error of up to 20 %. Consequently, these results are significantly impacted.

The initial evaluation of the measured data showed that the force magnitude increases with the speed of the upper plate, even though the viscosity decreases with higher shear rates. This occurs because the shear rate is in a range where viscosity does not change drastically, making the upper plate´s velocity the primary factor for the increasing force.

The second evaluation revealed the influence of temperature. The force magnitude at 40°C is lower than at 20°C. This is due to the lower viscosity at higher temperatures, and with all other conditions remaining the same, the force magnitude decreases accordingly.

Next, the influence of the moving plate´s area was evaluated. The force magnitude increases with a larger face area. Given that the smallest plate´s area is exactly one-quarter of the largest plate´s area, the force magnitude was expected to be similarly proportionate. This expectation was confirmed, though not entirely accurately, likely because the force values were close to zero with the smallest plate, reducing measurement accuracy.

The final evaluation assessed the influence of surface roughness. The results showed a slight increase in force magnitude with higher surface roughness of the upper plate. This can negatively impact comparison between the experimental measurement and simulation, because the simulation assume the perfectly smooth surface during calculation.

Future improvements could include using a sensor with a wider measurement range to capture all nuances during measurement and reduce the measurement error at near-zero values. Additionally, improving the clamping mechanism for the upper plate could reduce inaccuracies caused by improper clamping.

The final part of the thesis deals with numerical simulations. The first type of simulation is based on the experimental setup, consisting of one stationary plate and one

moving plate with grease between them. The geometry is simplified to a 2-D case. Given the high number of simulations performed, a mesh independence study was conducted to balance accuracy and computational time.

Initially, calculations were performed for each non-Newtonian fluid model discussed in the third chapter. These simulations were conducted under the same experimental conditions for easy comparison. At 20°C, the Cross and Carreau models showed the best match with experimental data, with only a 5 % difference between them. Further simulations revealed that the Cross model consistently outperformed the Carreau model by 5 %, making it the best representation of grease behavior at temperature 20°C.

A similar procedure was followed for simulations at temperature 40°C. Two models Power-Law and Herschel-Bulkley showed the best match with experimental data, with a 5 % difference between them according to MPD. Further simulations demonstrated that the Power-Law model performed consistently better by approximately 6 %, thus it was chosen as the best match at temperature 40°C.

The results of the simulations were then compared with the analytical model described in Chapter 4. The comparison showed that the simulation results were very similar to the analytical model, with a mean percentage difference (MPD) of approximately 2 %. This suggests that, for this case of Couette flow, the correct material model can be selected using analytical calculations, which provide almost immediate results compared to the time-consuming CFD simulations. The slight differences could be due to several factors: the rolling of grease in front of the plate, which is not considered in the analytical model, and the assumption of stationary flow in the analytical model, which is not true in this scenario (one plate moving harmonically).

The second simulation was based on the experimental setup but this time in 3-D with symmetry in the middle of the geometry. The purpose of this simulation was to validate the assumption of 2-D geometry made in the previous simulations and to observe the behavior of the grease around the corners and along the sides of the upper plate.

The results showed a perfect match in force magnitude between the 2-D and 3-D geometries. The behavior around the corners and along the sides had no significant effect on the force magnitude during movement. According to MPD the difference is only approximately 4 %, which can be easily considered as perfect match. Additionally, visual comparisons between the 2-D and 3-D simulations showed no discernible differences. This confirms that the 2-D simulations are sufficient for accurately modeling the force relationships in this setup.

The third type of simulation aims to investigate force relations in a real joint geometry, simplified to an axisymmetric problem using the geometry reconstructed in the second chapter. The motion of the rotating wall is derived from real measurements of the ball joint after assembly.

Initially, a mesh independence study was conducted to ensure the reliability of the results in terms of the size of the mesh cells. Subsequently, the results obtained with the appropriate mesh were compared with experimental data. However, the comparison revealed a significant difference between the experimental and simulation data.

The reason for this disparity is straightforward: the model used in this simulation assumes only the grease layer, meaning the force generated is solely from grease shearing. In contrast, the real ball joint comprises the full geometry, where the grease layer is only a small part of the entire system. The primary source of force in the real joint is the dry

contact between the plastic bearing and steel ball stud. Therefore, while these two sets of data can be compared, the conditions of measurement and simulation are vastly different.

The same results were obtained for the last type of simulation, which involved the full 3-D geometry of the grease layer. The purpose of this simulation was to validate the results from the simplified axisymmetric geometry.

The comparison between the 2-D and 3-D geometries showed a 42 % difference according to MPD, with the main variation occurring during changes in movement direction. In the 3-D geometry, the spikes were much higher, and the moment after the spikes smoothed out slightly higher as well.

Despite these differences, the gap between the experimental data and simulation remained significant. Thus, the conclusion that the primary source of moment is the dry contact between the plastic bearing and steel ball stud still holds true.

Nevertheless, despite the differing conditions of measurement and simulation, a few conclusions can still be drawn.

The breakaway torque moment, which occurs after the ball joint has been stationary for some time, may be partially attributed to the grease. The grease behaves as a solid until the yield stress is exceeded. This behavior is also evident in the simulations during changes in movement direction, where spikes occur. In real ball joints, grease is not only found in the simulated grease layer but also enclosed in small pockets across the plastic bearing surface. Since the grease behaves like a solid material when there is no movement, the lubrication quality during this phase could be significantly impacted. This can contribute to the breakaway moment during the ball joint measurement.

Furthermore, the moment generated by grease shearing is much smaller than that generated by dry contact in the ball joint. This observation suggests that torque moment reduction could be achieved by improving the lubrication mechanisms within the ball joint.

Overall, this thesis delves into a comprehensive investigation of grease behavior within ball joints, covering experimental, numerical, and analytical aspects. Through X-ray computed tomography, fluid modeling, experimental force measurements, and numerical simulations, significant insights into the complexities of grease lubrication have been gained. While challenges remain, particularly in reconciling experimental and simulation data within real joint geometries, the findings contribute substantially to understanding the intricate dynamics at play. These insights lay the groundwork for potential advancements in optimizing lubrication mechanisms within ball joints, which could have far-reaching implications for automotive suspension and steering systems.

List of References

[1] MANG, Theo; DRESEL, Wilfried. *Lubricants and Lubrication*. 1. Aufl. Weinheim: Wiley-VCH, 2007. ISBN 9783527314973.

[2] *Ball joint greases* [Internal Report]. THK RHYTHM AUTOMOTIVE CZECH, a.s., 2023.

[3] KATIYAR, Jitendra Kumar; BHATTACHARYA, Shantanu; PATEL, Vinay Kumar; KUMAR, Vikram. *Automotive Tribology*. 1st ed. 2019. Singapore: Springer Singapore Pte. Limited, 2019. Energy, Environment, and Sustainability. ISBN 9811504334. ISSN 2522-8366.

[4] *Naše výrobky* [online]. [N.d.]. [visited on 2024-04-18]. Available from: https://thkdacice.cz/o-nas/nase_vyrobky/.

[5] *Link Stabilizers* [online]. [N.d.]. [visited on 2024-04-20]. Available from: https://www.delphiautoparts.com/en-gb/products-and-technologies/braking-steering-suspension/steering-suspension/link-stabilizers.

[6] *What Is A Lower Control Arm And Why Is It Important?* [online]. [N.d.]. [visited on 2024-04-20]. Available from: https://www.nissanpartsplus.com/blog/lower-control-arms-explained.

[7] *4x4 upper control arms explained* [online]. 2018. [visited on 2024-04-20]. Available from: https://www.whichcar.com.au/gear/4x4-upper-control-arms-explained.

[8] *Suspension ball joints* [online]. [N.d.]. [visited on 2024-04-20]. Available from: https://www.zf.com/products/en/cars/products_65851.html.

[9] *Tie rods* [online]. [N.d.]. [visited on 2024-04-20]. Available from: https://www.moogparts.com/parts/steering/tie-rod-ends.html.

[10] *Costumer requirements - Ball joint* [Internal Report]. THK RHYTHM AUTOMOTIVE CZECH, a.s., 2023.

[11] *Hidden Structures Revealed* [online]. [N.d.]. [visited on 2024-04-20]. Available from: https://www.swri.org/node/1833796.

[12] CHIENG, Raymond. *X-ray production* [online]. 2023. [visited on 2024-04-20]. Available from: https://radiopaedia.org/articles/x-ray-production-2.

[13] BAGGETT, Tony. *Stationary Anode vs. Rotating Anode: Two C-Arm Tube Types Compared* [online]. 2019. [visited on 2024-04-20]. Available from: https://info.blockimaging.com/bid/100911/stationary-anode-vs-rotating-anode-two-c-arm-tube-types-compared.

[14] PRECISION, Matsusada. *Types of X-ray tubes and high-voltage power supplies* [online]. 2021. [visited on 2024-04-20]. Available from: https://www.matsusada.com/column/xray_tube_ps.html.

[15] NIKL, Martin. Scintillation detectors for x-rays. 2006, vol. 17, no. 4, R37–R54. ISSN 0957-0233.

[16] LUTZ, G.; KLANNER, R. Solid State Detectors. In: *Particle Physics Reference Library: Volume 2: Detectors for Particles and Radiation*. Ed. by FABJAN, Christian W.; SCHOPPER, Herwig. Cham: Springer International Publishing, 2020, pp. 137–200. ISBN 978-3-030-35318-6. Available from DOI: 10.1007/978-3-030-35318-6_5.

[17] TONG, Sheng; ALESSIO, Adam M.; KINAHAN, Paul E. Image reconstruction for PET/CT scanners: past achievements and future challenges. *Imaging Med.* 2010, vol. 2, no. 5, pp. 529–545. Available from DOI: 10.2217/iim.10.49.

[18] RI, Hwisong; KIM, Jongchol; LEE, Muchol; HWANG, Hyok; PAK, Jonghyok. Sinogram restoration based on shape property in computed tomography. *Informatics in Medicine Unlocked*. 2020, vol. 20, p. 100350. ISSN 2352-9148. Available from DOI: https://doi.org/10.1016/j.imu.2020.100350.

[19] KALKE, Martti; SILTANEN, Samuli. Sinogram Interpolation Method for Sparse-Angle Tomography. *Applied Mathematics*. 2014, vol. 05, pp. 423–441. Available from DOI: 10.4236/am.2014.53043.

[20] BUI, Ngoc Ha; BUI, Tien Hung; TRAN, Thuy Duong; TRAN, Kim Tuan; TRAN, Ngoc Toan. Evaluation of the effect of filters on reconstructed image quality from cone beam CT system. *Nuclear Science and Technology*. 2021, vol. 11, no. 1, pp. 35–47. Available from DOI: 10.53747/jnst.v11i1.130.

[21] CHEN, Honglei; LIU, Zenghua. Application and Challenges of Signal Processing Techniques for Lamb Waves Structural Integrity Evaluation: Part B-Defects Imaging and Recognition Techniques. In: 2018. ISBN 978-1-78923-787-0. Available from DOI: 10.5772/intechopen.79475.

[22] SINGH, M.P.; SANDHU, B.S.; SINGH, Bhajan. Measurement of effective atomic number of composite materials using scattering of -rays. *Nuclear Instruments and Methods in Physics Research Section A: Accelerators, Spectrometers, Detectors and Associated Equipment*. 2007, vol. 580, no. 1, pp. 50–53. ISSN 0168-9002. Available from DOI: https://doi.org/10.1016/j.nima.2007.05.037. Proceedings of the 10 th International Symposium on Radiation Physics.

[23] *Steels microstructure and properties*. 3rd ed. Amsterdam: Elsevier, Butterworth-Heinemann, 2006. ISBN 1-280-64271-8.

[24] AKKURT, Iskender. Effective atomic and electron numbers of some steels at different energies. *Annals of Nuclear Energy*. 2009, vol. 36, no. 11, pp. 1702–1705. ISSN 0306-4549. Available from DOI: https://doi.org/10.1016/j.anucene.2009.09.005.

[25] YILMAZ, D.; AKTAŞ, B.; ÇALIK, A.; AYTAR, O.B. Boronizing effect on the radiation shielding properties of Hardox 450 and Hardox HiTuf steels. *Radiation Physics and Chemistry*. 2019, vol. 161, pp. 55–59. ISSN 0969-806X. Available from DOI: https://doi.org/10.1016/j.radphyschem.2019.04.019.

[26] WACHARAWICHANANT, Sirirat; YASUMLEE, Nipawan. Morphology and Properties of Polyoxymethylene/Polypropylene/Microcrystalline Cellulose Composites. *Key Engineering Materials*. 2017, vol. 751, pp. 264–269. ISBN 3035710821. ISSN 1013-9826.

[27] BIRNBACHER, Lorenz; WILLNER, Marian; MARSCHNER, Mathias; PFEIFFER, Daniela; PFEIFFER, Franz; HERZEN, Julia. Accurate effective atomic number determination with polychromatic grating-based phase-contrast computed tomography. *Optics Express*. 2018, vol. 26, p. 15153. Available from DOI: 10.1364/OE.26.015153.

[28] LÊ, Huy; MOLLOI, Sabee. Segmentation and quantification of materials with energy discriminating computed tomography: A phantom study. *Medical physics*. 2011, vol. 38, pp. 228–37. Available from DOI: 10.1118/1.3525835.

[29] LUBRICATION, Klüber. *Klübersynth M115-01 material list* [online]. [N.d.]. [visited on 2024-01-28]. Available from: https://www.qualitybearingsonline.com/content/Lubricants/MSDS%20and%20TDS%20PDFs/Kluber/Kl%C3%BCbersynth_M_115-04_094085_PI_EN_en.pdf.

[30] *Air - Density, Specific Weight and Thermal Expansion Coefficient vs. Temperature and Pressure* [online]. [N.d.]. [visited on 2023-11-20]. Available from: https://www.engineeringtoolbox.com/air-density-specific-weight-d_600.html.

[31] KUMAR, T.Kiran; REDDY, K.Venkata. Effective atomic numbers for materials of dosimetric interest. *Radiation Physics and Chemistry*. 1997, vol. 50, no. 6, pp. 545–553. ISSN 0969-806X. Available from DOI: https://doi.org/10.1016/S0969-806X(97)00089-3.

[32] *XCOM: Photon Cross Sections Database* [online]. 2019. [visited on 2023-11-05]. Available from: https://www.nist.gov/pml/xcom-photon-cross-sections-database.

[33] *Aluminium 6082 -T6* [online]. 2001. [visited on 2023-11-06]. ISSN 1562-6016. Available from: https://www.matweb.com/search/datasheet_print.aspx?matguid=fad29be6e64d4e95a241690f1f6e1eb7.

[34] QADR, Hiwa. Calculation of gamma-ray attenuation parameters for aluminium, iron, zirconium and tungsten. *Problems of Atomic Science and Technology*. 2020, pp. 60–65.

[35] *Tungsten disulfide* [online]. 2001. [visited on 2023-11-06]. Available from: https://www.sigmaaldrich.com/CZ/en/product/aldrich/808806.

[36] *Xradia 610 and 620 Versa* [online]. 2020. [visited on 2023-12-06]. Available from: https://material-testing.com.vn/en/shop/xradia-610-and-620-versa/.

[37] *Image Filters and Settings* [online]. [N.d.]. [visited on 2023-12-08]. Available from: http://www.theobjects.com/dragonfly/dfhelp/4-0/Content/05_Image%20Processing/Image%20Filters%20and%20Settings.htm.

[38] BARTYZEL, Krzysztof. Adaptive Kuwahara filter. *Signal, Image and Video Processing*. 2015, vol. 10, pp. 1–8. Available from DOI: 10.1007/s11760-015-0791-3.

[39] PENG-O, Thaufig; CHAIKAN, Panyayot. High performance and energy efficient sobel edge detection. *Microprocessors and Microsystems*. 2021, vol. 87, p. 104368. ISSN 0141-9331. Available from DOI: https://doi.org/10.1016/j.micpro.2021.104368.

[40] ZHENG, Tao; DUAN, Zhizhao; WANG, Jin; LU, Guodong; LI, Shengjie; YU, Zhiyong. Research on Distance Transform and Neural Network Lidar Information Sampling Classification-Based Semantic Segmentation of 2D Indoor Room Maps. *Sensors*. 2021, vol. 21, p. 1365. Available from DOI: 10.3390/s21041365.

[41] WHITE, F.M. *Fluid Mechanics*. McGraw Hill, 2011. McGraw-Hill series in mechanical engineering. ISBN 9780073529349.

[42] BERK, Zeki. *Food process engineering and technology*. 1st ed. Amsterdam: Academic, 2009. ISBN 0123736609.

[43] RAPP, Bastian E. *Microfluidics: Modeling, Mechanics and Mathematics*. Elsevier, 2016. Micro and nano technologies series. ISBN 9781455731510.

[44] LI, Yanggui; WANG, Lei; ZHAO, Yun; WANG, Heping; LI, Shengshan; JIA, Jinfang. Numerical investigation of the flow characteristics of Bingham fluid on a slope with corrected smooth particle hydrodynamics. *Frontiers in Environmental Science*. 2022, vol. 10. ISSN 2296-665X. Available from DOI: 10.3389/fenvs.2022.1060703.

[45] RUDOLPH, Natalie; OSSWALD, Tim A. *Polymer Rheology - Fundamentals and Applications*. 1st ed. München: Hanser Publishers, 2015. ISBN 1569905177.

[46] TESCH, Krzysztof. On Invariants of Fluid Mechanics Tensors. *TASK Quarterly*. 2013, vol. 17, no. 3-4, pp. 223–230.

[47] ANSYS®, Research Fluent. *User's Guide 12.0* [online]. [N.d.]. [visited on 2024-01-25]. Available from: https://www.afs.enea.it/project/neptunius/docs/fluent/html/ug/node297.htm.

[48] MUKHERJEE, Siddhartha; BISWAL, Prayag; CHAKRABORTY, Suman; DASGUPTA, Sunando. Effects of viscous dissipation during forced convection of power-law fluids in microchannels. *International Communications in Heat and Mass Transfer*. 2017, vol. 89, pp. 83–90. ISSN 0735-1933. Available from DOI: https://doi.org/10.1016/j.icheatmasstransfer.2017.09.018.

[49] VIRTANEN, Pauli; GOMMERS, Ralf; OLIPHANT, Travis E.; HABERLAND, Matt; REDDY, Tyler; COURNAPEAU, David; BUROVSKI, Evgeni; PETERSON, Pearu; WECKESSER, Warren; BRIGHT, Jonathan; VAN DER WALT, Stéfan J.; BRETT, Matthew; WILSON, Joshua; MILLMAN, K. Jarrod; MAYOROV, Nikolay; NELSON, Andrew R. J.; JONES, Eric; KERN, Robert; LARSON, Eric; CAREY, C J; POLAT, İlhan; FENG, Yu; MOORE, Eric W.; VANDERPLAS, Jake; LAXALDE, Denis; PERKTOLD, Josef; CIMRMAN, Robert; HENRIKSEN, Ian; QUINTERO, E. A.; HARRIS, Charles R.; ARCHIBALD, Anne M.; RIBEIRO, Antônio H.; PEDREGOSA, Fabian; VAN MULBREGT, Paul; SCIPY 1.0 CONTRIBUTORS. SciPy 1.0: Fundamental Algorithms for Scientific Computing in Python. *Nature Methods*. 2020, vol. 17, pp. 261–272. Available from DOI: 10.1038/s41592-019-0686-2.

[50] MULLINEUX, Glen. Non-linear least squares fitting of coefficients in the Herschel–Bulkley model. *Applied Mathematical Modelling*. 2008, vol. 32, no. 12, pp. 2538–2551. ISSN 0307-904X. Available from DOI: https://doi.org/10.1016/j.apm.2007.09.010.

[51] CHHABRA, R. P; RICHARDSON, J. F. *Non-Newtonian Flow and Applied Rheology - Engineering Applications (2nd Edition)*. 2nd ed. Oxford: Elsevier, 2008. ISBN 9780750685320.

[52] CROSS, Malcolm M. Rheology of non-Newtonian fluids: A new flow equation for pseudoplastic systems. *Journal of Colloid Science*. 1965, vol. 20, no. 5, pp. 417–437. ISSN 0095-8522. Available from DOI: https://doi.org/10.1016/0095-8522(65)90022-X.

[53] KARPÍŠEK, Zdeněk. *Matematika IV: statistika a pravděpodobnost*. 4., přeprac. vyd. Brno: Akademické nakladatelství CERM, 2014. ISBN 978-80-214-4858-2.

[54] *Bruker tribometers* [online]. [N.d.]. [visited on 2024-03-22]. Available from: https://www.bruker.com/en/products-and-solutions/test-and-measurement/tribometers-and-mechanical-testers/umt-tribolab.html.

[55] NETME. *Laboratoř Tribologie* [online]. 2016. [visited on 2024-03-23]. Available from: http://netme.cz/cs/tribology-laboratory/.

[56] MARKUS, Patrick. *Concept and Applications of UMT TriboLab* [online]. [N.d.]. [visited on 2024-03-28]. Available from: https://www.ucs.br/site/midia/arquivos/05-06-18-ensaios-tribologicos-e-mecanicos.pdf.

[57] SNOPEK, Lukáš. *Konstrukce modulu simulátoru pro analýzu tření a opotřebení zubů při čištění* [Bakalářská práce]. Brno, 2021. Dostupné také z: https://www.vutbr.cz/studenti/zav-prace/detail/131886.

[58] STAFF, LFW. *Optical profiler from Bruker features 3D microscope* [online]. Laser Focus World, 2020 [visited on 2024-03-24]. Available from: https://www.laserfocusworld.com/software-accessories/software/article/16562646/optical-profiler-from-bruker-features-3d-microscope.

[59] ARAVINNA, A. G. *Basic Concepts of Measurement Uncertainty*. 2018. Available from DOI: 10.13140/RG.2.2.27778.99520.

[60] DOU, Hua-Shu; KHOO, Boo Cheong. Investigation of Turbulent transition in plane Couette flows Using Energy Gradient Method. *arXiv.org*. 2010. ISSN 2331-8422.

[61] AYDIN, E. M.; LEUTHEUSSER, H. J. Plane-Couette flow between smooth and rough walls. *Experiments in Fluids*. 1991, vol. 11, pp. 302–312. Available from DOI: 10.1007/BF00194862.

[62] DAVIAUD, F; HEGSETH, J; BERGE, P. SUBCRITICAL TRANSITION TO TURBULENCE IN PLANE COUETTE-FLOW. *Physical review letters*. 1992, vol. 69, no. 17, pp. 2511–2514. ISSN 0031-9007.

[63] TILLMARK, Nils; ALFREDSSON, P. Henrik. Experiments on transition in plane Couette flow. *Journal of Fluid Mechanics*. 1992, vol. 235, pp. 89–102. Available from DOI: 10.1017/S0022112092001046.

[64] LUNDBLADH, Anders; JOHANSSON, Arne V. Direct simulation of turbulent spots in plane Couette flow. *Journal of Fluid Mechanics*. 1991, vol. 229, pp. 499–516. Available from DOI: 10.1017/S0022112091003130.

[65] MOZES, Robert; COOPER, Peter; ATKIN, Rob; LI, Hua. Ionic Liquids as Grease Base Liquids. *Lubricants*. 2017, vol. 5, p. 31. Available from DOI: 10.3390/lubricants5030031.

[66] UHLMANN, Lars; MANNENS, Robby; WEISER, Ingo; HERRIG, Tim; BERGS, Thomas. Identification of Influencing Factors in Machine Hammer Peening with Consideration of Lubricant Influences. *Key Engineering Materials*. 2022, vol. 926, pp. 834–842. Available from DOI: 10.4028/p-l7jb8c.

[67] *Dynamic mesh methods* [online]. ANSYS, Inc., [n.d.] [visited on 2024-04-12]. Available from: https://www.afs.enea.it/project/neptunius/docs/fluent/html/th/node40.htm#dynam-layer-meth.

[68] GASPARINI, Ricardo. *Mesh sensitivity study for CFD projects: Knowledge base* [online]. 2022. [visited on 2024-04-16]. Available from: https://www.simscale.com/knowledge-base/mesh-sensitivity-cfd/.

[69] THERESA. *What is a Courant Number?* [online]. 2020. [visited on 2024-04-26]. Available from: https://www.simscale.com/knowledge-base/what-is-a-courant-number/.

[70] *Courant number in CFD simulations* [online]. [N.d.]. [visited on 2024-04-26]. Available from: https://www.idealsimulations.com/resources/courant-number-cfd/.

List of abbreviations

Abbreviation	Meaning
CT	Computed tomography
CFD	Computational fluid dynamics
MPD	Mean percentage difference
PAO	Polyalphaolefin
PFPE	Perfluoropolyether
PTFE	Polytetrafluoroethylene
POM	Polyoxymethylene
WS_2	Tungsten disulfide
ROI	Region of interest
LVDT	Linear variable differential transformer
VOF	Volume of fluid
RMSE	Root mean squared error

List of appendixes

A Appendix A - Power-Law fit

```python
import numpy as np
import pandas as pd
import matplotlib.pyplot as plt
from scipy.optimize import curve_fit

# Load the data
data = pd.read_excel() # Specify the path to an excel
x = np.array(data.x)
y_viscosity = np.array(data.derivation)
y_shear_stress = np.array(data.y)

# Define the Power_law_model function
def Power_law_model(gamma, K, n):
    return K * gamma ** n

# Define the combined fitting function
def combined_fit(gamma, K, n):
    shear_stress_fit = Power_law_model(gamma, K, n)
    viscosity_fit = np.diff(shear_stress_fit) / np.diff(gamma)
    viscosity_fit = np.concatenate(([viscosity_fit[0]], viscosity_fit
        ))
    return np.concatenate((shear_stress_fit, viscosity_fit))

# Perform the combined curve fitting
popt, pcov = curve_fit(combined_fit, x, np.concatenate((
    y_shear_stress, y_viscosity)), p0=[1, 1])

# Extract the optimized parameter values
K_fit, n_fit = popt

# Generate the fitted data using the optimized parameters
gamma_fit = np.linspace(0, max(x), 1000)  # Range of gamma values for
     plotting
shear_stress_fit = Power_law_model(gamma_fit, *popt)
viscosity_fit = np.diff(shear_stress_fit) / np.diff(gamma_fit)
viscosity_fit = np.concatenate(([viscosity_fit[0]], viscosity_fit))

# Calculation of coefficient of determination (R_squared)
residuals = np.concatenate((y_shear_stress, y_viscosity)) -
    combined_fit(x, *popt)
TSS = np.sum((np.concatenate((y_shear_stress, y_viscosity)) - np.mean
    (np.concatenate((y_shear_stress, y_viscosity))))**2)
RSS = np.sum(residuals**2)
r_squared = 1 - (RSS / TSS)

# Create subplots
fig, (ax1, ax2) = plt.subplots(1, 2, figsize=(12, 6))
```

```
43
44 # Plot the shear stress - shear rate
45 ax1.scatter(x, y_shear_stress, color='blue', label='Experimental data
       ')
46 ax1.plot(gamma_fit, shear_stress_fit, color='red', label='Fitted
       Power-Law')
47 ax1.set_xlabel('Shear rate (s^-1)')
48 ax1.set_ylabel('Shear stress (Pa)')
49 ax1.legend()
50 ax1.grid(True)
51
52 # Plot the viscosity - shear rate
53 ax2.scatter(x, y_viscosity, color='green', label='Derived viscosity')
54 ax2.plot(gamma_fit, viscosity_fit, color='purple', label='Fitted
       Power-Law')
55 ax2.set_xlabel('Shear rate (s^-1)')
56 ax2.set_ylabel('Viscosity (Pa.s)')
57 ax2.legend()
58 ax2.grid(True)
59
60 # Plot charts
61 plt.tight_layout()
62 plt.show()
63
64 # Print and display results
65 results_text = f"R²: {r_squared:.8f} (-)\nFlow index: {n_fit:.3f} (-)
       \nConsistency factor K: {K_fit:.2f} (Pa*s^n)"
66 print(results_text)
```

B Appendix B - Herschel-Bulkley fit

```
import numpy as np
import pandas as pd
import matplotlib.pyplot as plt
from scipy.optimize import curve_fit

# Load the data
data = pd.read_excel() # Specify the path to an excel
x = np.array(data.x)
y_viscosity = np.array(data.derivation)
y = np.array(data.y)
x_integrated = x
y_integrated = y

# Define necessary constants
m = len(x)
accuracy = 10000
n = np.linspace(0,5,accuracy)

# Define constants recommended by article
XXX = max(x)
YYY = max(y)

# calculation of the matrix elements
F = np.zeros(accuracy)
for j in range(accuracy):
    nn = n[j]
    C = 1/((XXX**(3*nn))*YYY)
    m11 = m
    m12 = sum(x**nn)
    m13 = sum((x**nn)*(np.log(x)))
    m21 = sum(x**nn)
    m22 = sum(x**(2*nn))
    m23 = sum((x**(2*nn))*(np.log(x)))
    m31 = sum(y)
    m32 = sum((x**nn)*y)
    m33 = sum((x**nn)*y*(np.log(x)))

    # Calculate the determinant af matrix in range of "n"
    F[j] = C * (((m11 * m22  * m33) + (m21 * m32 * m13) + (m31 * m12
       * m23)) - ((m13 * m22 * m31) + (m23 * m32 * m11) + (m33 * m12
       * m21)))

#Find the inflection point in determinant function
for i in range (1,accuracy - 1):
    if F[i-1] < F[i] and F[i] > F[i+1]:
        inflex_point_1 = i

```

```
#Set the values from zero to inflection point as value in inflection point
for i in range (0,inflex_point_1):
    F[i] = F[inflex_point_1]

#Function to find the index of the element in the array that is closest to the given value
def find_zero_index(array, value):
    array = np.asarray(array)
    index = (np.abs(array - value)).argmin()
    return index

n_constant = n[find_zero_index(F, value = 0)]

# Define the Herschel_Bulkley model function
def HB_model(gamma, tau_0, K):
    return tau_0 + K * gamma ** n_constant

# Define the combined fitting function
def combined_fit(gamma, tau_0, K):
    shear_stress_fit = HB_model(gamma, tau_0, K)
    viscosity_fit_fit = np.diff(shear_stress_fit) / np.diff(gamma)
    viscosity_fit_fit = np.concatenate(([viscosity_fit_fit[0]], viscosity_fit_fit))
    return np.concatenate((shear_stress_fit, viscosity_fit_fit))

# Combine the data arrays
combined_y = np.concatenate((y_integrated, y_viscosity))

# Perform the combined curve fitting
popt, pcov = curve_fit(combined_fit, x, combined_y, p0=[1, 1])

# Extract the optimized parameter values
Tau_0_fit, K_fit = popt

# Specify the percentage increase threshold
percentage_increase_threshold = 10

# Find the index where shear stress exceeds the threshold
threshold_index = np.argmax(y > y[0] * (1 + percentage_increase_threshold / 100))

# Estimate the critical shear stress and shear rate
critical_shear_stress = y[threshold_index]
critical_shear_rate = x[threshold_index]

# Generate the fitted data using the optimized parameters
gamma_fit = np.linspace(min(x), max(x), 1000)  # Range of gamma values for plotting
shear_stress_fit = HB_model(gamma_fit, *popt)
```

```
viscosity_fit_fit = np.diff(shear_stress_fit) / np.diff(gamma_fit)
viscosity_fit_fit = np.concatenate(([viscosity_fit_fit[0]],
    viscosity_fit_fit))

# Calculation of coefficient of determination (R_squared)
residuals = combined_y - combined_fit(x, *popt)
TSS = np.sum((combined_y - np.mean(combined_y))**2)
RSS = np.sum(residuals**2)
r_squared = 1 - (RSS / TSS)

# Subplot definition
fig, (ax1, ax2) = plt.subplots(1, 2, figsize=(12, 6))

# Plot the viscosity - shear rate
ax1.scatter(x_integrated, y_integrated, color='blue', label='
    Experimental␣data')
ax1.plot(gamma_fit, shear_stress_fit, color='red', label='Fitted␣
    Herschel-Bulkley')
ax1.set_xlabel('Shear␣rate␣(s^-1)')
ax1.set_ylabel('Shear␣stress␣(Pa)')
ax1.grid(True)
ax1.legend()

# Plot the shear stress - shear rate
ax2.scatter(x, y_viscosity, color='green', label='Derived␣viscosity')
ax2.plot(gamma_fit, viscosity_fit_fit, color='purple', label='Fitted␣
    Herschel-Bulkley')
ax2.set_xlabel('Shear␣rate␣(s^-1)')
ax2.set_ylabel('Viscosity␣(Pa.s)')
ax2.grid(True)
ax2.legend()

# Plot the graphs
plt.tight_layout()

# Print and display results
results_text = f"R²:␣{r_squared:.8f}␣(-)\nFlow␣index:␣{n_constant:.3f
    }␣(-)\nConsistency␣factor␣K:␣{K_fit:.2f}␣(Pa.s^n)\nYield␣stress:␣{
    Tau_0_fit:.3f}␣(Pa)\nCritical␣shear␣stress:␣{critical_shear_stress
    :.3f}␣(Pa)\nCritical␣shear␣rate:␣{critical_shear_rate:.3f}␣(s^-1)"
print(results_text)
plt.show()
```

C Appendix C - Carreau fit

```python
import numpy as np
import pandas as pd
import matplotlib.pyplot as plt
from scipy.optimize import curve_fit
from scipy.integrate import quad, cumtrapz

# Define the Carreau model function
def carreau_model(lambda_dot, tau_0, lambda_k, n):
    return tau_0 * (1 + (lambda_dot * lambda_k) ** 2) ** ((n - 1) / 2)

# Load the data
data = pd.read_excel() # Specify the path to an excel
x = np.array(data.x)
y_viscosity = np.array(data.derivation)
y_shear_stress = np.array(data.y)

# Function to calculate shear stress integral
def shear_stress_integral(lambda_dot, tau_0, lambda_k, n):
    def integrand(x):
        return carreau_model(x, tau_0, lambda_k, n)

    result, _ = quad(integrand, 0, lambda_dot)
    return result

# Function to fit both viscosity and shear stress
def combined_fit(lambda_dot, tau_0, lambda_k, n):
    viscosity_fit = carreau_model(lambda_dot, tau_0, lambda_k, n)
    shear_stress_fit = np.array([shear_stress_integral(l, tau_0, lambda_k, n) for l in lambda_dot])
    return np.concatenate((viscosity_fit, shear_stress_fit))

# Perform the combined curve fitting
popt, pcov = curve_fit(combined_fit, x, np.concatenate((y_viscosity, y_shear_stress)), bounds=([0, 0, 0], [100, 100, 5]))

# Extract the optimized parameter values
viscosity_0_fit, lambda_k_fit, n_fit = popt

# Generate a range of shear rates for plotting the fitted curve
lambda_dot_range = np.linspace(0, max(x), 100000)
fitted_data = combined_fit(lambda_dot_range, viscosity_0_fit, lambda_k_fit, n_fit)
viscosity_fit = fitted_data[:len(lambda_dot_range)]
shear_stress_fit = fitted_data[len(lambda_dot_range):]

# Define the function to calculate viscosity in logarithmic scale
```

```
44 def visc_log(lambda_dot):
45     return viscosity_0_fit * (1 + (lambda_dot * lambda_k_fit) ** 2)
       ** ((n_fit - 1) / 2)
46
47 # Calculate the coefficient of determination (R-squared)
48 predicted_data = combined_fit(x, viscosity_0_fit, lambda_k_fit, n_fit
   )
49 residuals_viscosity = y_viscosity - predicted_data[:len(x)]
50 residuals_shear_stress = y_shear_stress - predicted_data[len(x):]
51 SSR = np.sum(residuals_viscosity ** 2) + np.sum(
   residuals_shear_stress ** 2)
52 SST = np.sum((y_viscosity - np.mean(y_viscosity)) ** 2) + np.sum((
   y_shear_stress - np.mean(y_shear_stress)) ** 2)
53 r_squared = 1 - (SSR / SST)
54
55 # Create subplots
56 fig, (ax1, ax2) = plt.subplots(1, 2, figsize=(16, 4))
57
58 # Plot the viscosity - shear rate
59 ax1.scatter(x, y_viscosity, color='green', label='Derived␣viscosity')
60 ax1.plot(lambda_dot_range, viscosity_fit, color='red', label='Fitted␣
   viscosity')
61 ax1.set_xlabel('Shear␣rate␣(s^-1)')
62 ax1.set_ylabel('Viscosity␣(Pa.s)')
63 ax1.legend()
64 ax1.grid(True)
65
66 # Plot the shear stress - shear rate
67 ax2.scatter(x, y_shear_stress, color='blue', label='Measured␣shear␣
   stress')
68 ax2.plot(lambda_dot_range, cumtrapz(carreau_model(lambda_dot_range,
   viscosity_0_fit, lambda_k_fit, n_fit), lambda_dot_range, initial
   =0), color='purple', label='Fitted␣shear␣stress')
69 ax2.set_xlabel('Shear␣rate␣(s^-1)')
70 ax2.set_ylabel('Shear␣stress␣(Pa)')
71 ax2.legend()
72 ax2.grid(True)
73
74 # Plot the graphs
75 plt.tight_layout()
76 plt.show()
77
78 results_text = f"R²:␣{r_squared:.8f}␣(-)\nPower-law␣index:␣{n_fit:.3f
   }␣(-)\nTime␣constant:␣{lambda_k_fit:.3f}␣(s)\nZero␣shear␣rate␣
   viscosity:␣{viscosity_0_fit:.3f}␣(Pa.s)\nInfinite␣shear␣rate␣
   viscosity␣:␣0␣(Pa.s)"
79 print(results_text)
```

D Appendix D - Cross fit

```python
import numpy as np
import pandas as pd
import matplotlib.pyplot as plt
from scipy.optimize import curve_fit
from scipy.integrate import quad

# Load the data
data = pd.read_excel() # Specify the path to an excel
x = np.array(data.x)
y_viscosity = np.array(data.derivation)
y_shear_stress = np.array(data.y)

# Define the Cross_model function
def Cross_model(lambda_dot, tau_0, lambda_k, n):
    return tau_0 / (1 + (lambda_k * lambda_dot) ** (1 - n))

# Define the shear stress integral function
def shear_stress_integral(lambda_dot, tau_0, lambda_k, n):
    integrand = lambda x: Cross_model(x, tau_0, lambda_k, n)
    result, _ = quad(integrand, 0, lambda_dot)
    return result

# Define the combined fitting function
def combined_fit(lambda_dot, tau_0, lambda_k, n):
    viscosity_fit = Cross_model(lambda_dot, tau_0, lambda_k, n)
    shear_stress_fit = np.array([shear_stress_integral(l, tau_0,
       lambda_k, n) for l in lambda_dot])
    return np.concatenate((viscosity_fit, shear_stress_fit))

# Perform the combined curve fitting
popt, pcov = curve_fit(combined_fit, x, np.concatenate((y_viscosity,
   y_shear_stress)), bounds=([0, 0, 0], [100, 100, 5]))

# Extract the optimized parameter values
tau_0_fit, lambda_k_fit, n_fit = popt

# Generate a range of shear rates for plotting the fitted curve
lambda_dot_range = np.linspace(0, max(x), 100000)
fitted_data = combined_fit(lambda_dot_range, tau_0_fit, lambda_k_fit,
    n_fit)
viscosity_fit = fitted_data[:len(lambda_dot_range)]
shear_stress_fit = fitted_data[len(lambda_dot_range):]

# Calculate the coefficient of determination (R-squared)
predicted_data = combined_fit(x, tau_0_fit, lambda_k_fit, n_fit)
residuals_viscosity = y_viscosity - predicted_data[:len(x)]
residuals_shear_stress = y_shear_stress - predicted_data[len(x):]
```

```
SSR = np.sum(residuals_viscosity ** 2) + np.sum(
    residuals_shear_stress ** 2)
SST = np.sum((y_viscosity - np.mean(y_viscosity)) ** 2) + np.sum((
    y_shear_stress - np.mean(y_shear_stress)) ** 2)
r_squared = 1 - (SSR / SST)

# Create subplots
fig, (ax1, ax2) = plt.subplots(1, 2, figsize=(16, 4))

# Plot the viscosity - shear rate
ax1.scatter(x, y_viscosity, color='green', label='Measured viscosity'
    )
ax1.plot(lambda_dot_range, Cross_model(lambda_dot_range, tau_0_fit,
    lambda_k_fit, n_fit), color='red', label='Fitted viscosity')
ax1.set_xlabel('Shear rate (s^-1)')
ax1.set_ylabel('Viscosity (Pa.s)')
ax1.legend()
ax1.grid(True)

# Plot the shear stress - shear rate
ax2.scatter(x, y_shear_stress, color='blue', label='Measured shear
    stress')
ax2.plot(lambda_dot_range, shear_stress_fit, color='purple', label='
    Fitted shear stress')
ax2.set_xlabel('Shear rate (s^-1)')
ax2.set_ylabel('Shear stress (Pa)')
ax2.legend()
ax2.grid(True)

# Plot the graphs
plt.tight_layout()
plt.show()

results_text = f"R²: {r_squared:.8f} (-)\nPower-law index: {n_fit:.3f
    } (-)\nTime constant: {lambda_k_fit:.5f} (s)\nZero shear rate
    viscosity: {tau_0_fit:.4f} (Pa.s)\nInfinite shear rate viscosity:
    0 (Pa.s)"
print(results_text)
```

E Appendix E - Large plate

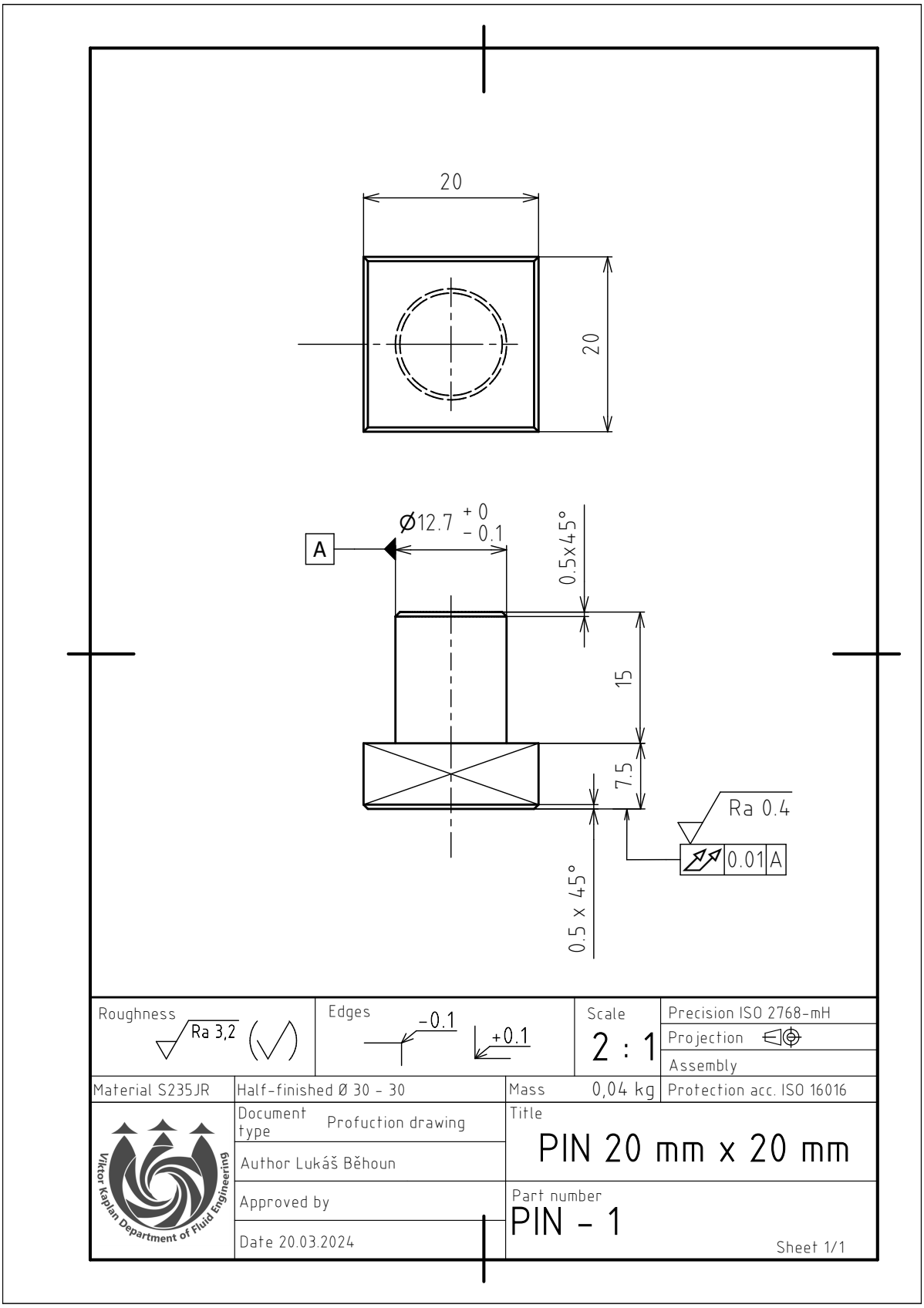

F Appendix F - Medium plate

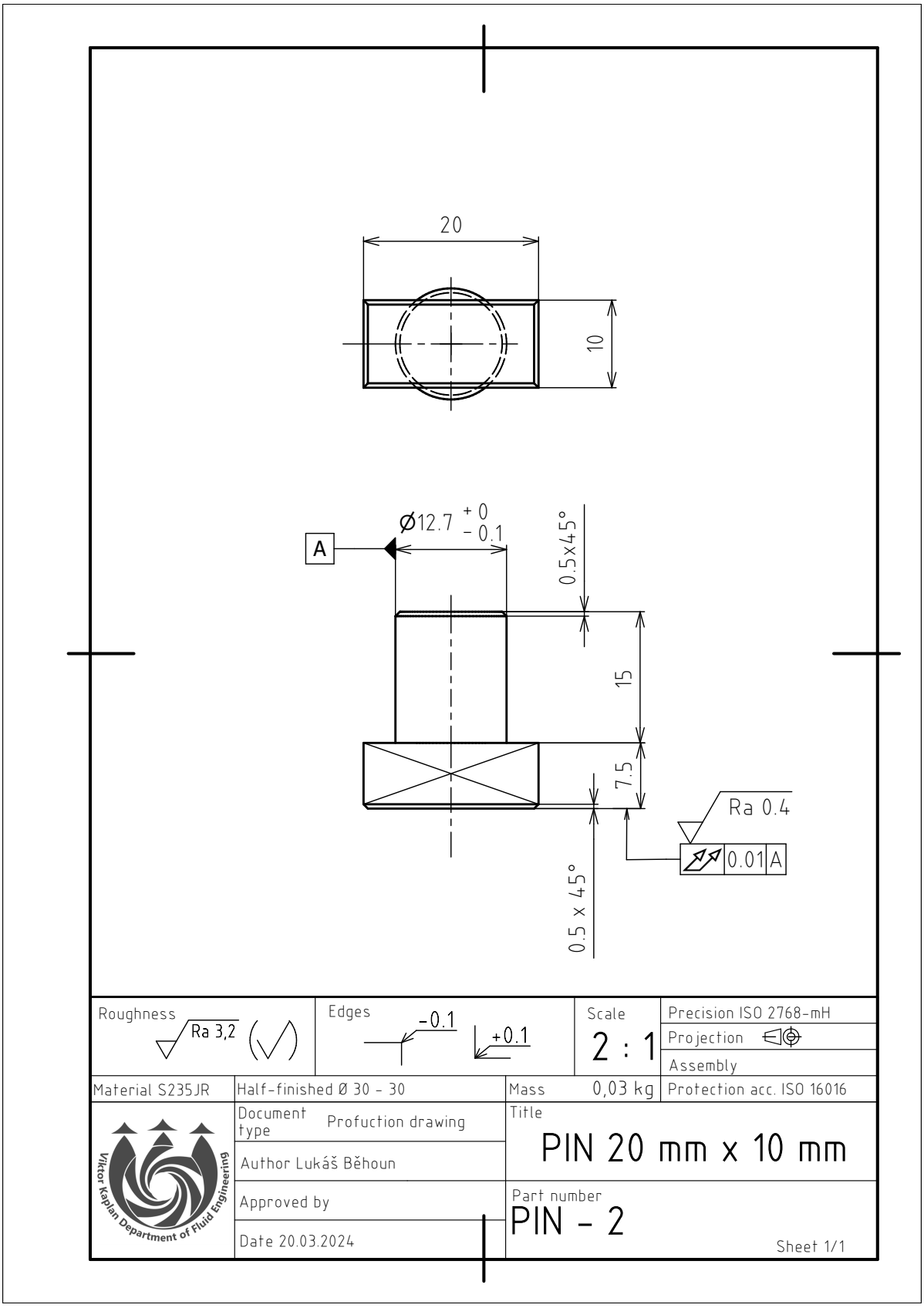

G Appendix G - Small plate

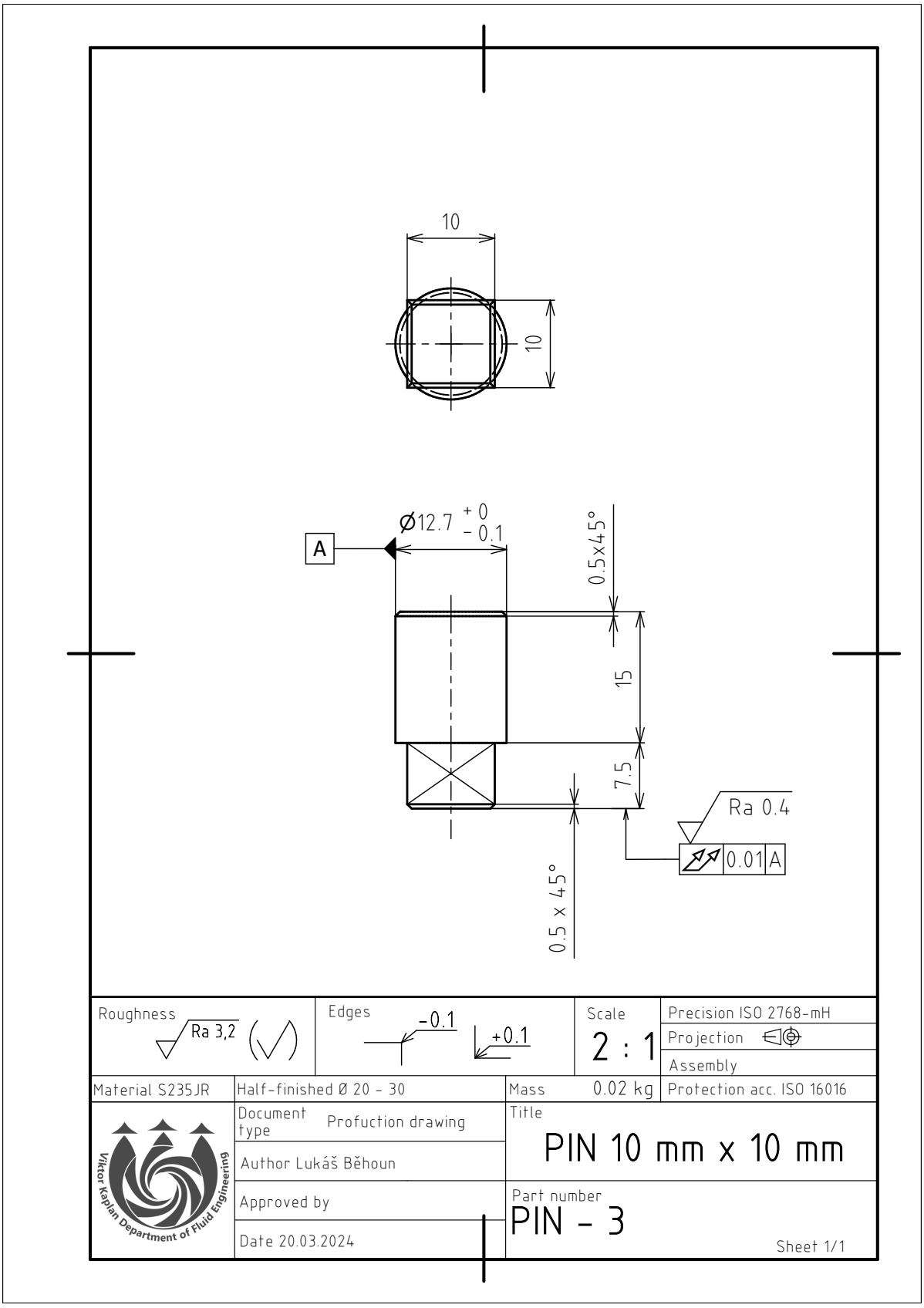

H Appendix H - All experiments

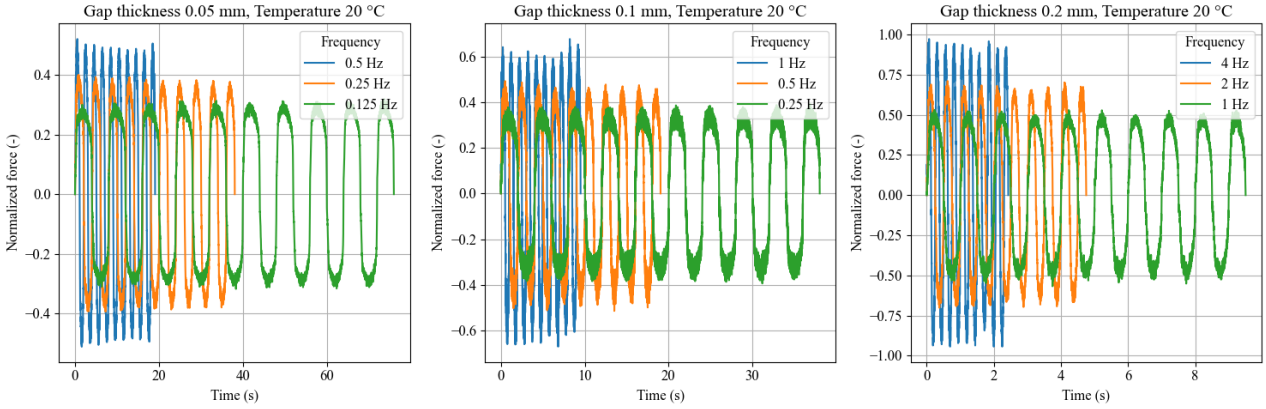

Figure H.1. All test done with plate with dimensions 20 mm x 20 mm at temperature 20 °C. The results are normalized on y-axis.

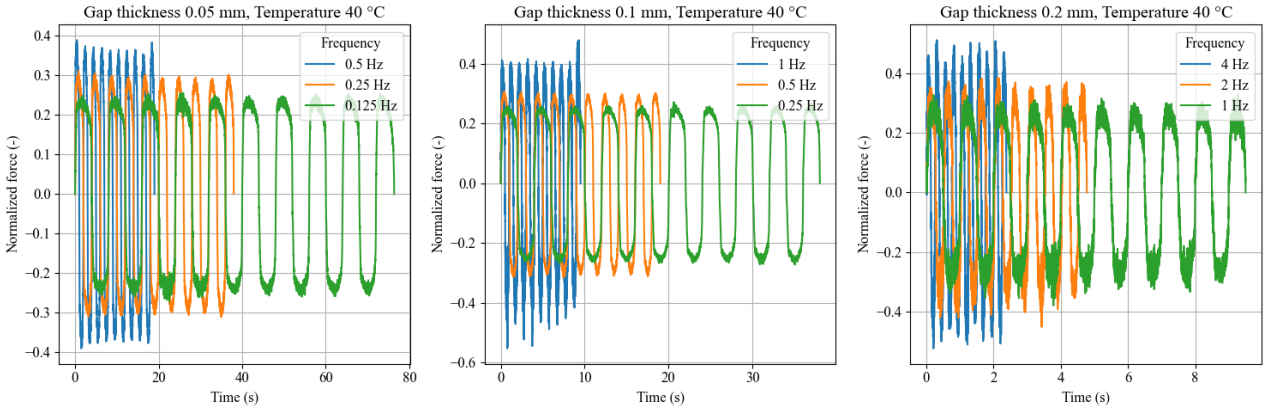

Figure H.2. All test done with plate with dimensions 20 mm x 20 mm at temperature 40 °C. The results are normalized on y-axis.

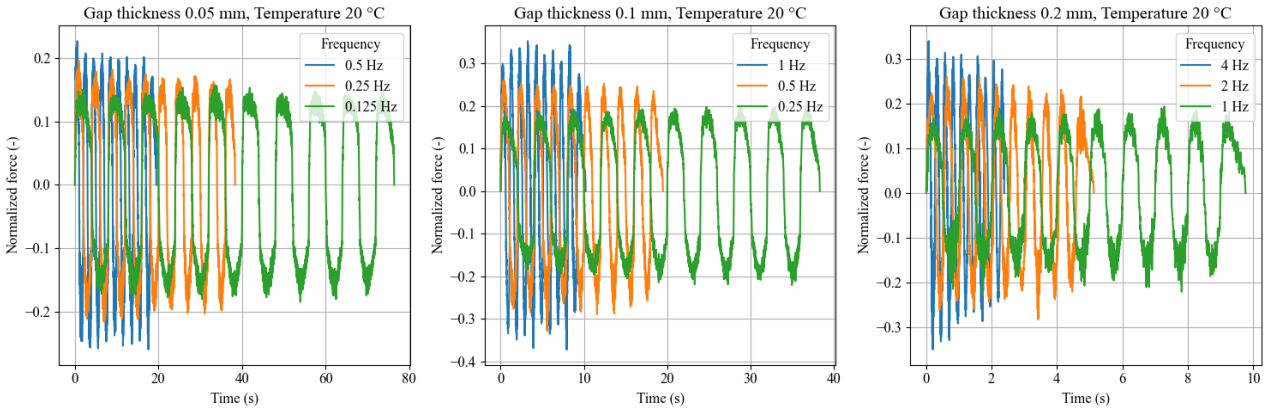

Figure H.3. All test done with plate with dimensions 20 mm x 10 mm (long) at temperature 20 °C. The results are normalized on y-axis.

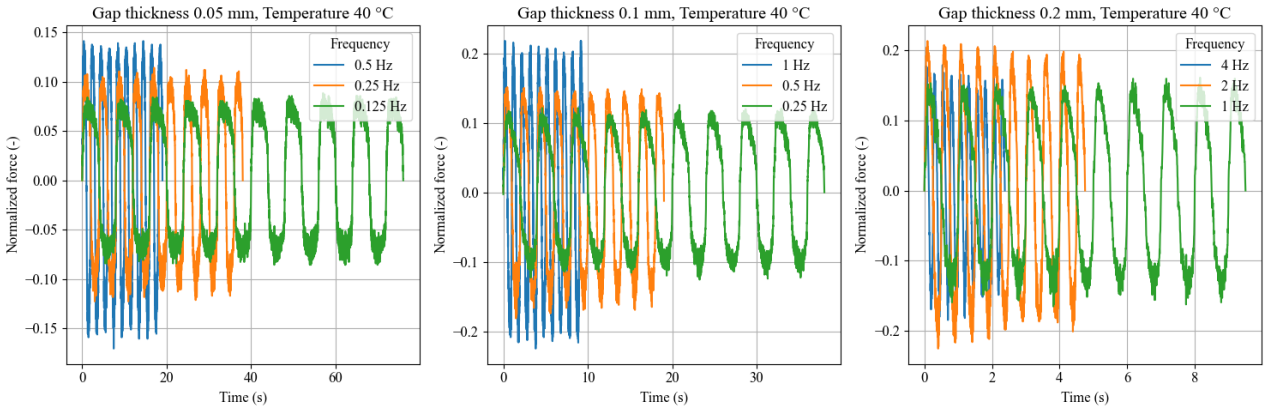

Figure H.4. All test done with plate with dimensions 20 mm x 10 mm (long) at temperature 40 °C. The results are normalized on y-axis.

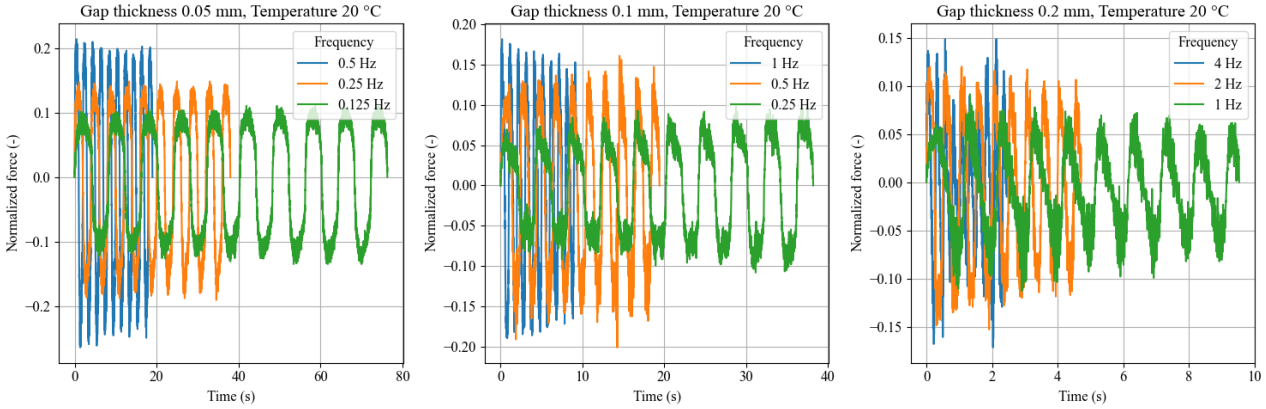

Figure H.5. All test done with plate with dimensions 20 mm x 10 mm (short) at temperature 20 °C. The results are normalized on y-axis.

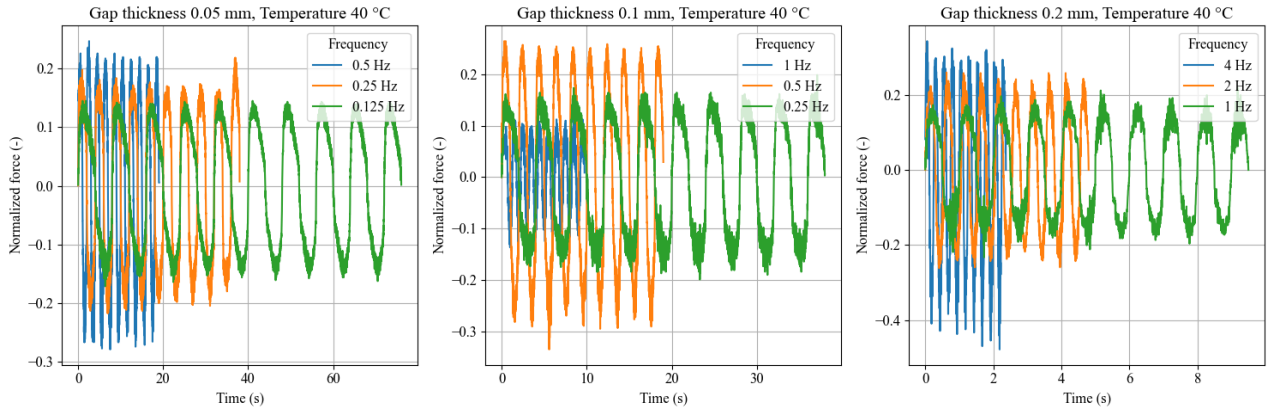

Figure H.6. All test done with plate with dimensions 20 mm x 10 mm (short) at temperature 40 °C. The results are normalized on y-axis.

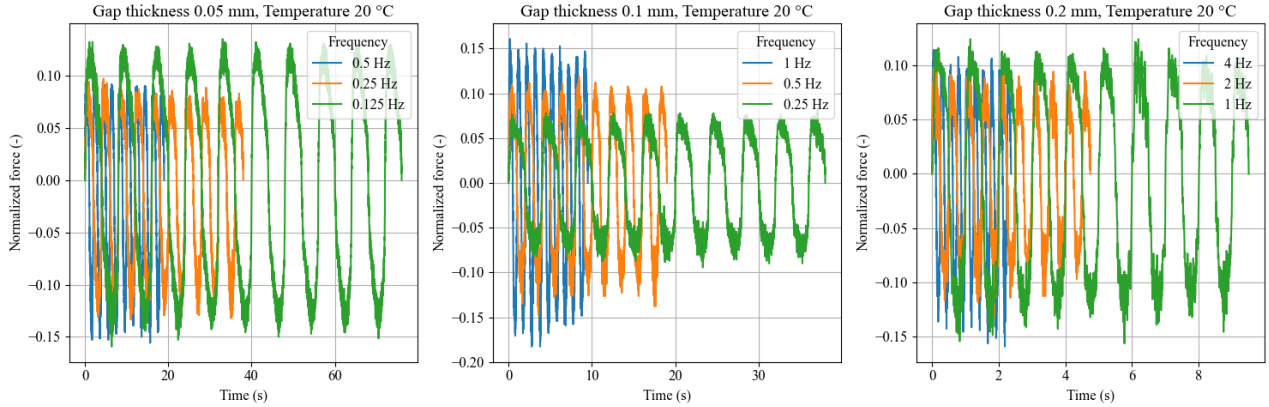

Figure H.7. All test done with plate with dimensions 10 mm x 10 mm at temperature 20 °C. The results are normalized on y-axis.

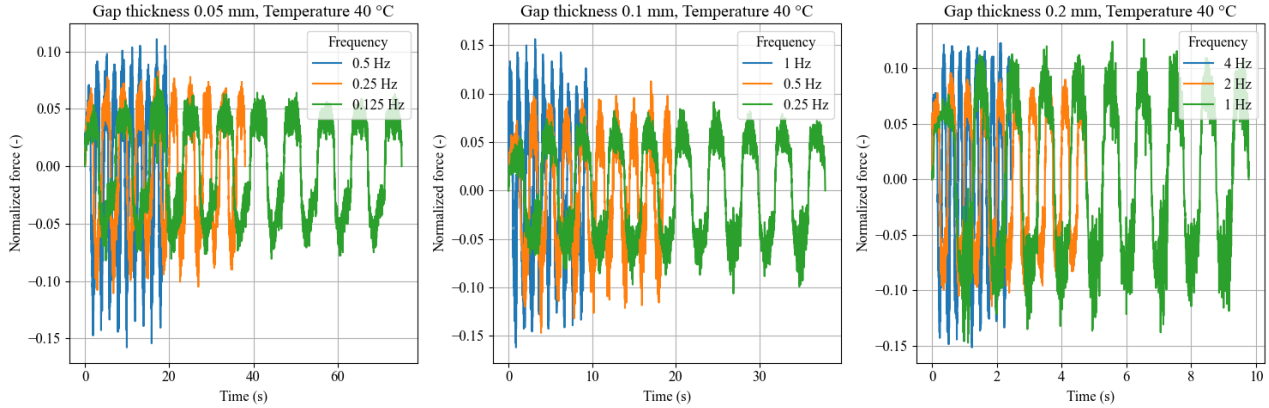

Figure H.8. All test done with plate with dimensions 10 mm x 10 mm at temperature 40 °C. The results are normalized on y-axis.